ASPECTS OF STRONGLY CORRELATED MANY-BODY FERMI SYSTEMS

William J. Porter III

A dissertation submitted to the faculty at the University of North Carolina at Chapel Hill in partial fulfillment of the requirements for the degree of Doctor of Philosophy in the Department of Physics.

Chapel Hill
2017

Approved by:

Joaquín E. Drut

Louise A. Dolan

Charles R. Evans

Dmitri V. Khveshchenko

Yue Wu

ABSTRACT

William J. Porter III: ASPECTS OF STRONGLY CORRELATED MANY-BODY FERMI SYSTEMS
(Under the direction of Joaquín E. Drut)

A, by now, well-known signal-to-noise problem plagues Monte Carlo calculations of quantum-information-theoretic observables in systems of interacting fermions, particularly the Rényi entanglement entropies S_n, even in many cases where the infamous sign problem does not appear. Several methods have been put forward to circumvent this affliction including ensemble-switching techniques using auxiliary partition-function ratios. This dissertation presents an algorithm that modifies the recently proposed free-fermion decomposition in an essential way: we incorporate the entanglement-sensitive correlations directly into the probability measure in a natural way. Implementing this algorithm, we demonstrate that it is compatible with the hybrid Monte Carlo algorithm, the workhorse of the lattice quantum chromodynamics community and an essential tool for studying gauge theories that contain dynamical fermions. By studying a simple one-dimensional Hubbard model, we demonstrate that our method does not exhibit the same debilitating numerical difficulties that naïve attempts to study entanglement often encounter. Following that, we illustrate some key probabilistic insights, using intuition derived from the previous method and its successes to construct a simpler, better behaved, and more elegant algorithm. Using this method, in combination with new identities which allow us to avoid seemingly necessary numerical difficulties, the inversion of the restricted one-body density matrices, we compute high order Rényi entropies and perform a thorough comparison to this new algorithm's predecessor using the Hubbard model mentioned before. Finally, we characterize non-perturbatively the Rényi entropies of degree $n = 2, 3, 4$, and 5 of three-dimensional, strongly coupled many-fermion systems in the scale-invariant regime of short interaction range and large scattering length, i.e. in the unitary limit using the algorithms detailed herein. We also detail an exact, few-body projective method which we use to characterize the entanglement properties of the two-body sector across a broad range of attractive couplings. In the many-body case, we determine universal scaling properties of this system, and for the two-body case, we compute the entanglement spectrum exactly, successfully characterizing a vast range of entanglement behavior across the BCS-BEC crossover.

<div align="center">**TABLE OF CONTENTS**</div>

LIST OF FIGURES

LIST OF ABBREVIATIONS AND SYMBOLS

A Sub-region.

$\bar{A}$ Complement of sub-region.

β Temperature or imaginary time.

d Number of spatial dimensions.

G_A Reduced one-body density matrix.

$\hat{H}$ Hamiltonian operator.

HMC   Hybrid Monte Carlo.

HS   Hubbard-Stratonovich.

MC   Monte Carlo.

n Rényi order.

N_x Linear spatial lattice size.

QCD   Quantum Chromodynamics.

$\hat{\rho}$ Density matrix.

$\hat{\rho}_A$ Reduced density matrix.

S_n Order n Rényi entanglement entropy.

σ Auxiliary field.

CHAPTER 1: Computing the Second Rényi Entropy in a System of Interacting Fermions

Section 1.1: Introduction

Quantum-information and topological aspects of condensed matter physics, broadly defined in order to include all few- and many-body quantum systems, continue to gain attention from a variety of perspectives, with the notion of entanglement playing a key role [7, 8, 9]. Topological quantum phase transitions have been shown to bear a direct connection to the so-called entanglement entropy in both its von Neumann and Rényi forms, through the entanglement spectrum, and by other information-related quantities [10, 11, 12]. Thus, the computation of Rényi entanglement entropies S_n is currently of great importance to many fields (see e.g. [13, 14, 15, 16, 17, 18, 19, 20]), and physicists must meet the challenge of doing so in interacting systems, particularly in strongly coupled and universal regimes.

To meet this challenge, an array of Monte Carlo (MC) methods have recently been developed to compute S_n (see e.g. [21, 22, 23, 24, 25, 26, 27, 1, 28, 29, 30, 31]). As explained below, one of the essential steps shared accross many of the underlying formalisms is the replica trick [14], a paradigm which yields most often an expression for the entropies S_n that naturally appears as a ratio of two partition-function-like objects. Generally, partition functions themselves are challenging objects to compute from a numerical standpoint: they typically involve terms that vary on vastly dissimilar numerical scales, a problem that only gets worse with increasing system size. In the context of stochastic calculations of S_n, it is now understood that this complication manifests itself as a signal-to-noise problem. The naïve estimation of these partition functions, followed necessarily by the calculation of their ratio, leads to unmanageable statistical uncertainties that grow exponentially with the volume of the (sub-)system considered (see e.g. [1, 28, 29] for an explanation).

In this chapter, we present a lattice MC approach for the calculation of the integer-order Rényi entropies S_n. We use a specific case of one-dimensional spin-1/2 fermions governed by a Hubbard-type Hamiltonian as an example, which allows us to compare our results with the exact numerical solution as well as with other extant MC methods, but the technique can be generalized to arbitrary systems, including those with gauge fields and Fermi-Bose mixtures (as long as the so-called sign problem is absent, as in any other MC calculation; see e.g. [32, 33, 34]). To highlight the great generality of this approach, we carry out our calculations using the hybrid Monte Carlo algorithm (HMC) [35, 36] (see [37, 38] for basic introductions to HMC), which is a staple of lattice QCD. It is essential in non-perturbative studies of gauge theories with

dynamical fermions and has been used in a variety of graphene studies [39, 40, 41, 42].

Section 1.2:   Formalism

We place the system on a d-dimensional spatial lattice of extent N_x. Since we are utilizing a finite lattice, the single-particle Hilbert space is of finite extent as well, namely N_x^d. We then follow the formalism of Ref. [1] in order to facilitate comparison.

The n-th order Rényi entanglement entropy S_n of a sub-system A of a given quantum mechanical system is defined as

$$S_n = \frac{1}{1-n} \ln \text{tr}(\hat{\rho}_A^n), \tag{1.1}$$

where $\hat{\rho}_A$ is the reduced density matrix of sub-system A (that is, after the degrees of freedom of the rest of the system are traced out). Specifically, for a system with density matrix $\hat{\rho}$, the reduced density matrix is defined via a partial trace over the Hilbert space corresponding to the complement $\bar{A}$ of our sub-system as

$$\hat{\rho}_A = \text{tr}_{\bar{A}}\,\hat{\rho}. \tag{1.2}$$

Further details regarding the brute-force evaluation of this partial trace will be provided in later chapters when the few-body problem is examined in detail. We table these discussions for now.

In Ref. [1], Grover obtained an auxiliary-field path-integral form for $\hat{\rho}_A$. Using this form, he showed that S_n can be computed using MC methods for a range of systems. We summarize those derivations below. In auxiliary-field Monte Carlo methods one introduces a Hubbard-Stratonovich (auxiliary) field σ that decouples the fermion species so that the usual density matrix $\hat{\rho}$ can be written as a path integral:

$$\hat{\rho} = \frac{e^{-\beta \hat{H}}}{\mathcal{Z}} = \int \mathcal{D}\sigma\, P[\sigma]\, \hat{\rho}[\sigma], \tag{1.3}$$

in terms off a system-dependent normalized probability measure $P[\sigma]$ determined by the specifics of the Hamiltonian in question (for more detail, see [32, 33, 34]). In our derivation, the partition function is given by $\mathcal{Z} = \text{tr}[e^{-\beta \hat{H}}]$, and the operator $\hat{\rho}[\sigma]$ denotes an auxiliary density matrix corresponding to noninteracting particles in an external field σ. Analogously, Grover proved that one may rewrite the reduced density matrix as

$$\hat{\rho}_A = \int \mathcal{D}\sigma\, P[\sigma]\, \hat{\rho}_A[\sigma], \tag{1.4}$$

with

$$\hat{\rho}_A[\sigma] = C_A[\sigma] \, \exp\left(-\sum_{i,j} \hat{c}_i^\dagger [\ln(G_A^{-1}[\sigma] - 1)]_{ij} \hat{c}_j\right), \tag{1.5}$$

and where the functional $C_A[\sigma]$ is defined

$$C_A[\sigma] = \det(1 - G_A[\sigma]). \tag{1.6}$$

Above, we have used the restricted Green's function $[G_A[\sigma]]_{ij}$, which corresponds to a free single-particle Green's function $G(i,j)$ in the background field σ but such that the arguments i,j only take values in the region A (see Ref. [1] and also Ref. [43, 44, 45], where expressions for the reduced density matrix of free systems, based on reduced Green's functions, were obtained first).

Using the above choice of $\hat{\rho}_A[\sigma]$, Grover showed that the expectation of $c_j c_i^\dagger$ in the auxiliary free system correctly reproduces the restricted single-particle Green's functions, as it is required to do. Therefore, by linearity, expectation values of observables supported only in the region A are reproduced as well. This validates the expression on the right-hand side of Eq. (2.4).

Using this expression, taking powers of $\hat{\rho}_A$ necessarily results in the appearance of a number of HS fields, which we collectively denote below as $\{\sigma\}$. A manifestation of the replica trick [14], this approach allows the trace of the n-th power of $\hat{\rho}_A$ in Eq. (2.1) to be recast as a field integral over a product of fermion determinants that depend on the collection of fields $\{\sigma\}$. Indeed, for a system of $2N$-component fermions, using an auxiliary-field transformation that decouples them, we obtain

$$\exp\left((1-n)S_n\right) = \int \mathcal{D}\{\sigma\} P[\{\sigma\}] \, Q[\{\sigma\}], \tag{1.7}$$

where the field integration measure, given by

$$\mathcal{D}\{\sigma\} = \prod_{k=1}^{n} \frac{\mathcal{D}\sigma_k}{\mathcal{Z}}, \tag{1.8}$$

is over the n "replicas" σ_k of the Hubbard-Stratonovich auxiliary field. We have included the normalization

$$\mathcal{Z} = \int \mathcal{D}\sigma \prod_{m=1}^{2N} \det U_m[\sigma] \tag{1.9}$$

in the integration measure to simplify the notation. The seemingly natural probability measure, given by

$$P[\{\sigma\}] = \prod_{k=1}^{n} \prod_{m=1}^{2N} \det U_m[\sigma_k], \tag{1.10}$$

3

factorizes completely across replicas, and it is therefore blind to correlations associated with quantum entanglement. This factorization is the main reason why using $P[\{\sigma\}]$ as a MC probability leads to (seemingly) insurmountable signal-to-noise problems, as shown in Ref. [1]; it is also why we call it naïve (although that is by no means a judgement of Ref. [1]). In Eq. (2.10), $U_m[\sigma]$ is a matrix which encodes the dynamics of the m-th component in the system, namely the kinetic energy and the form of the interaction after an auxiliary-field decomposition; it further encodes the form of the trial ket $|\Psi\rangle$ in ground-state projective formulations (see e.g. Ref. [32, 33, 34]), as we employ in this work. We will take the ket $|\Psi\rangle$ to be a Slater determinant. In finite-temperature approaches, the matrix $U_m[\sigma]$ is obtained by evolving a complete set of single-particle states in imaginary time.

The factor that introduces the critical contributions to entanglement measures is

$$Q[\{\sigma\}] = \prod_{m=1}^{2N} \det M_m[\{\sigma\}], \tag{1.11}$$

where we abbreviate

$$M_m[\{\sigma\}] \equiv \prod_{k=1}^{n} \left(1 - G_{A,m}[\sigma_k]\right) \left[1 + \prod_{k=1}^{n} \frac{G_{A,m}[\sigma_k]}{1 - G_{A,m}[\sigma_k]}\right]. \tag{1.12}$$

In the above equation, we have written $G_{A,m}[\sigma_k]$, which is a restricted Green's function, as previously defined, but where we now indicate the fermion component m and replica field index k.

The product $Q[\{\sigma\}]$ was identified as playing the role of an observable in Ref. [1], which is a natural interpretation in light of Eq. (2.7), but which we will interpret differently below. Note that, for $n = 2$, thankfully, no matrix inversion is required in the calculation of $Q[\{\sigma\}]$; for higher n, however, there is no obvious way to avoid the inversion of $1 - G_{A,m}[\sigma_k]$. We comment on this in subsequent chapters. Otherwise, it seems this calculation would require some kind of numerical regularization technique (see Ref. [30, 31]) to avoid singularities in $G_{A,m}[\sigma_k]$, whose eigenvalues can be close to zero and unity.

In zero-temperature paradigms, the extent of $U_m[\sigma]$ is given by the number of particles of the m-th species present in the system. In finite-temperature approaches, the size is that of the whole single-particle Hilbert space (i.e. the size of the lattice, as mentioned earlier). The size of $G_{A,m}[\sigma_k]$, on the other hand, is always given by the number of lattice sites enclosed by the region A. Note that, separating a factor of $\mathcal{Z}^n$ in the denominator of Eq. (2.7), an explicit form can be identified in the numerator as the result of the so-called replica trick [14] (namely a partition function for n copies of the system, "glued" together in the region A).

Section 1.3: Our proposed method

By analogy to the right side of Eq. (2.7), we define an auxiliary parameter $0 \leq \lambda \leq 1$ and introduce a function $\Gamma(\lambda; g)$ as

$$\Gamma(\lambda; g) \equiv \int \mathcal{D}\{\sigma\} P[\{\sigma\}] \, Q[\{\sigma\}; \lambda], \tag{1.13}$$

where we have augmented the dependence of $Q[\{\sigma\}]$ on the coupling g by replacing

$$g \to \lambda^2 g, \tag{1.14}$$

which defines $Q[\{\sigma\}; \lambda]$. From this definition, it follows immediately that $\Gamma(\lambda; g)$ satisfies two pivotal constraints, each of which with different nontrivial physical significance: For $\lambda = 0$, we see

$$\frac{1}{1-n} \ln \Gamma(0; g) = S_n^{(0)}, \tag{1.15}$$

where $S_n^{(0)}$ is the entropy of a noninteracting system, that is, one where $g \to 0$. To wit, at $\lambda = 0$ the functional $Q[\{\sigma\}; \lambda]$ does not depend on the auxiliary fields $\{\sigma\}$ and factors completely from the integral. Ergo, independent of the numerical value of g, the function $\Gamma(0; g)$ corresponds to the Rényi entropy of a free system, which can be computed trivially within the present formalism, although in the prototype calculations that follow, we make use of Grover's original formalism for simplicity. Indeed, in the free case the lack of fluctuation in the auxiliary field implies that there is no path integral when interactions are turned off, such that the noninteracting result can be computed with a single Monte Carlo sample using the formalism by Grover mentioned above. It is worth mention that the Rényi entropy of a noninteracting system has received substantial attention in the recent few years, with specific techniques developed for their study and specific, and interesting, results arising therefrom. A lot is known about these quantities for a variety of systems, in particular in connection with area laws, modified area laws, and their violation [2, 3, 46, 4, 6].

For $\lambda = 1$, on the other hand, $\Gamma(\lambda; g)$ corresponds to the Rényi entanglement entropy of the fully interacting system:

$$\frac{1}{1-n} \ln \Gamma(1; g) = S_n. \tag{1.16}$$

Therefore, both of these reference points are physically relevant, one of them is relatively straight-forward to compute, and obtaining the other reference point is our objective in this chapter.

Using Eq. (3.84),

$$\frac{\partial \ln \Gamma}{\partial \lambda} = \int \mathcal{D}\{\sigma\} \tilde{P}[\{\sigma\}; \lambda] \, \tilde{Q}[\{\sigma\}; \lambda] \tag{1.17}$$

5

where

$$\tilde{P}[\{\sigma\};\lambda] = \frac{1}{\Gamma(\lambda;g)} P[\{\sigma\}] \, Q[\{\sigma\};\lambda], \tag{1.18}$$

and

$$\tilde{Q}[\{\sigma\};\lambda] = \sum_{m=1}^{2N} \mathrm{tr} \left[M_{m,\lambda}^{-1}[\{\sigma\}] \frac{\partial M_{m,\lambda}[\{\sigma\}]}{\partial \lambda} \right]. \tag{1.19}$$

It is important that any dependence on the auxiliary parameter λ appears only in the matrix M_n. It is in this way that we include the entanglement correlations in the MC sampling algorithm, which is to be done using $\tilde{P}[\{\sigma\};\lambda]$ as the probability measure. When considering an even number of flavors $2N$, and when the interactions are not repulsive, $\det^{2N} U[\sigma]$ and $Q[\{\sigma\},\lambda]$ are real and positive semidefinite for any real σ. This nonnegativity means that there is no sign problem, and $\tilde{P}[\{\sigma\};\lambda]$ above is useful as a normalized, well-defined probability distribution.

More specifically, the method presented in this chapter to compute S_n is to take the free $\lambda = 0$ point as a reference and calculate S_n by integration using

$$S_n = S_n^{(0)} + \frac{1}{1-n} \int_0^1 d\lambda \, \langle \tilde{Q}[\{\sigma\};\lambda] \rangle, \tag{1.20}$$

where

$$\langle X \rangle = \int \mathcal{D}\{\sigma\} \tilde{P}[\{\sigma\};\lambda] \, X[\{\sigma\}]. \tag{1.21}$$

Another way, we obtained an integral form of the interacting Rényi entanglement entropy that can be calculated using any of a great variety of MC methods, in particular the hybrid Monte Carlo algorithm (HMC) [35, 36]. The latter combines molecular dynamics (MD) of the auxiliary fields (defining a fictitious auxiliary conjugate momentum independent of the auxiliary fields) with the Metropolis-type accept-reject step. This combination enables simultaneous global updates of all n of the auxiliary fields $\{\sigma\}$. As is well known in the lattice QCD community, HMC is an exceptionally efficient sampling strategy, particularly when gauge fields are required (see e.g. [35, 36, 32, 33, 34]). The integration of the MD equations of motion requires the calculation of the MD force, which is given by the functional derivative of the augmented measure $\tilde{P}[\{\sigma\};\lambda]$ with respect to the fields $\{\sigma\}$, and can be calculated directly from Eq. (3.88).

The method described above is akin to the so-called coupling-constant integration approach of many-body physics, particularly finite-temperature, grand-canonical formulations, but it is significantly different in that we have strategically introduced the λ dependence only in the entanglement-sensitive determinant $Q[\{\sigma\};\lambda]$ of Eq. (2.11).

Equation (3.89) is our first main result and defines this version of the method. An essential point

is that the expectation that appears above is taken with respect to the augmented probability measure $\tilde{P}[\{\sigma\}; \lambda]$, which includes the correlations that account for quantum entanglement. In contrast to the naïve MC probability $P[\{\sigma\}]$, which corresponds to statistically independent replicas of the auxiliary field, this measure does not display the factorization responsible for the signal-to-noise problem afflicting previous work mentioned above.

In practice, using Eq. (3.89) requires MC calculations to evaluate $\langle \tilde{Q}[\{\sigma\}; \lambda] \rangle$ stochastically as a function of the parameter λ, followed by numerical integration over this parameter. We find that $\langle \tilde{Q}[\{\sigma\}; \lambda] \rangle$ is a surprisingly smooth function of λ that vanishes gradually at $\lambda = 0$ and displays most of its features close to $\lambda = 1$ (further details below). We therefore carry out the numerical integration using the Gauss-Legendre quadrature method [47] in an effort to sample it efficiently. It should also be pointed out that the stochastic evaluation of $\langle \tilde{Q}[\{\sigma\}; \lambda] \rangle$, for fixed subregion A, can be expected to feature roughly symmetric fluctuations about its mean value. Therefore, after integration over the parameter λ, the statistical effects on the entropy are reduced (as we show empirically in the Results section of this chapter).

A few comments are necessary at this point regarding the auxiliary parameter. First, we could have performed the replacement $g \to \lambda^2 g$ everywhere, i.e. not only in Q but also in P (including its normalization $\mathcal{Z}$). This global replacement would have led to three terms in the derivative of PQ with respect to λ, two of which would come from P (recall P is normalized) and feature different signs and a rather indirect connection to S_n (recall P factorizes across replicas). Our approach avoids this superfluous difficulty by focusing solely on the entanglement portion of the integrand (i.e. Q). Additionally, we could have used a power λ^x of the auxiliary parameter rather than its square λ^2, where x does not have to be an integer (although it would be rather inconvenient to make it less than 1). This is indeed a possibility, and it allows for further optimization than pursued here. In what remains of this chapter, we set $x = 2$, as above. Finally, the calculations required for different values of λ are completely independent from one another with likely unrelated probability measures governing their evaluation. These calculations can therefore be performed wholly in parallel with essentially perfect scaling (up to the computationally negligible final data gathering and quadrature).

Section 1.4: Relation to other methods

Our formulation is quite similar to the temperature-integration method of Ref. [21, 22, 23, 24], but it is much closer in its formulation to the ratio trick (and similar schemes) of Refs. [25, 29]. As discussed above,

the calculation begins from the replica trick originally introduced by Calabrese and Cardy [14], i.e.

$$\exp((1-n)S_n) = \frac{\mathcal{Z}_{A,n}}{\mathcal{Z}^n},\tag{1.22}$$

where $\mathcal{Z}_{A,n}$ is the partition function of n replicas of the system "glued" together across the quantum numbers A. Usually, $\mathcal{Z}_{A,n}$ and $\mathcal{Z}^n$ can be grossly different from each other in scale, especially if S_n is large (as is usually the case for large sub-system sizes). As a result, calculating the partition functions given above separately (and stochastically) and attempting afterward to evaluate the ratio of the two is very likely to yield a large statistical uncertainty resulting in a significant signal-to-noise problem. Hope of circumventing this problem is can be derived from the use of the ratio (or increment) trick, whereby one introduces auxiliary ratios of the partition function corresponding to systems whose configuration spaces are only marginally dissimilar. In other words, one uses

$$\exp((1-n)S_n) = \frac{\mathcal{Z}_{A,n}}{\mathcal{Z}^n} = \frac{\mathcal{Z}_{A,n}}{\mathcal{Z}_{A-1,n}}\frac{\mathcal{Z}_{A-1,n}}{\mathcal{Z}_{A-2,n}}\cdots\frac{\mathcal{Z}_{2,n}}{\mathcal{Z}_{1,n}}\frac{\mathcal{Z}_{1,n}}{\mathcal{Z}^n},\tag{1.23}$$

where the intermediate ratios $\mathcal{Z}_{A-i,n}/\mathcal{Z}_{A-i-1,n}$ are chosen to correspond to subsystems of similar size and shape (e.g. such that their linear dimension differs by one lattice spacing). In this way, each of the auxiliary ratios can be expected to not differ significantly from unity, and with enough intermediate ratios, calculations can be carried out in a stable fashion at the price of calculating a potentially large number of ratios.

In the method we detail here, the auxiliary parameter λ is analogous to the varying region size A of the ratio trick. Using Eq. (3.89), we may write

$$\exp\left((1-n)(S_n - S_n^{(0)})\right) = \prod_{\lambda=0}^{1}\exp\left(\Delta\lambda\,\langle\tilde{Q}[\{\sigma\};\lambda]\rangle\right),\tag{1.24}$$

where any discretization $\Delta\lambda$ of the exponent inside the product yields an acceptable (similar) telescoping sequence of ratios as in Eq. (1.23). So long as $\langle\tilde{Q}[\{\sigma\};\lambda]\rangle$ is regular in λ, which we find to be the case in all work performed, our auxiliary factors can be made to be arbitrarily close to unity at the cost of (at most) linear scaling in computation time.

Section 1.5:   Results

We test this first algorithm by calculating the second Rényi entropy S_2 for a family of ten-site, one-dimensional Hubbard models at half filling with periodic boundary conditions in space. The Hamiltonian

operator we simulate is

$$\hat{H} = -t \sum_{s,\langle ij \rangle} \left(\hat{c}^\dagger_{i,s} \hat{c}_{j,s} + \hat{c}^\dagger_{j,s} \hat{c}_{i,s} \right) + U \sum_i \hat{n}_{i\uparrow} \hat{n}_{i\downarrow}, \tag{1.25}$$

where in the above the first sum includes our two distinct fermion species $s = \uparrow, \downarrow$ and all pairs of nearest-neighbor sites. We implemented a symmetric (second order) Trotter-Suzuki factorization of the original canonical Boltzmann weight, with an imaginary-time discretization parameter $\tau = 0.05$ (in lattice units). The full extent of the imaginary-time axis was at its largest $\beta = 5$ (that is, we had 100 imaginary-time lattice sites). The factor in the Trotter-Suzuki decomposition that contains the interaction was addressed, as anticipated in a previous discussion, by introducing a replica HS variable σ for each power of the reduced density matrix $\hat{\rho}_A$. This insertion was accomplished by an auxiliary-field transformation. We selected a version of this transformation based around a continuous field with a convenient, compact range (see Ref. [32, 33, 34]).

Figure 1.1 shows the MC average $\langle \tilde{Q}[\{\sigma\}; \lambda] \rangle$ as a function of not only the auxiliary parameter λ but also of the subregion size L_A for four values of the Hubbard coupling U/t. We emphasize that surfaces corresponding to weak couplings demonstrate significantly less fluctuation along both axes than do their strongly interacting analogues. This uniformity suggests that for weakly coupled systems, even at large L_A, a coarse λ discretization may yield accurate estimates of S_n. Conversely, strongly coupled systems are, not unexpectedly, more computationally demanding.

For smaller subsystems, the majority of the deviation from the noninteracting entropy is accumulated at large λ, on top of an already relatively small amount of variation, and this accumulation appears with almost entirely uniform signature. Much to the contrary, for the larger subsystems, intermediate values of λ correspond to a region of parameter space that contributes opposite-sign corrections to the entropy. This difference yields increasing uncertainty as a function of the subsystem size due to the required cancellations which must, for this system, guarantee that the entropy vanishes when the subregion is taken to the be the entire system. This interesting effect is most clearly visible for the curve corresponding to the case where, again, the subregion constitutes the entire system. In this case, S_2 is zero, for several reasons, regardless of the value of the coupling, which implies that the integral over λ must be identically zero. This vanishing happens by a precise cancelation that must be faithfully captured by the numerical integration procedure. Given that the features of $\langle \tilde{Q}[\{\sigma\}; \lambda] \rangle$ are most greatly represented in $0.5 < \lambda < 1$, we chose a Gauss-Legendre quadrature method to carry out the numerical integral in a precise and efficient way. With $N_\lambda = 20$ points in the integration domain $[0, 1]$ (i.e. 40 points in the extended defining interval $[-1, 1]$ using an even extension of the integrand), we see that, for the parameter values used here, the systematic effects associated with λ are contained within the statistical uncertainty, as required.
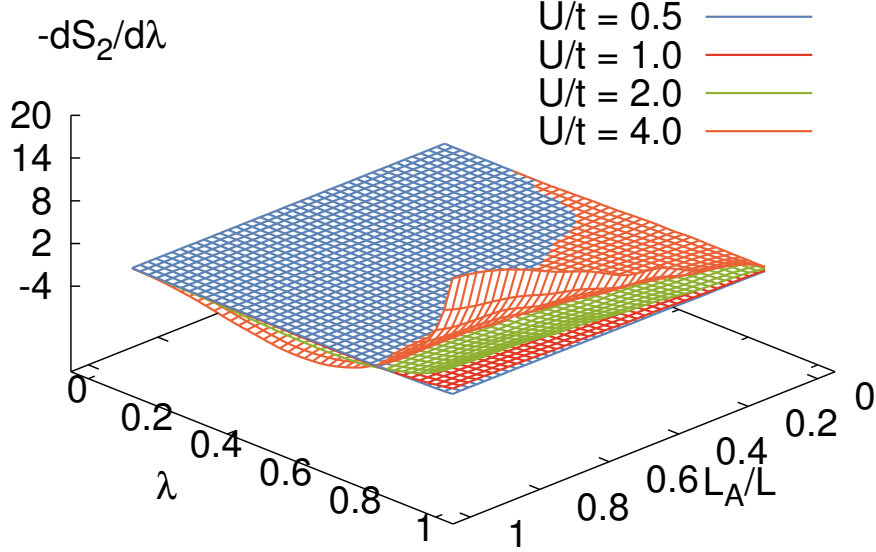
Figure 1.1: HMC results for the source (integrand) with $U/t = 0.5, 1.0, 2.0$, and 4.0 (from bottom to top at $\lambda = 1$) as functions of the auxiliary parameter λ and of the region size L_A, for a system of size $N_x = 10$ sites.

Our experience with this method, and this system in particular, indicates that the features we have observed in studying the source $\langle \tilde{Q}[\{\sigma\}; \lambda] \rangle$ are quite generic: they fluctuate in amplitude with the coupling, but their qualitative features are largely insensitive to the overall system size, and they generally behave in a surprisingly benign way as a function of λ and the sub-system size, so long as the sampling routine is sufficiently robust. Hence, the auxiliary parameter integration does not contribute to the scaling of the computation time versus system size beyond a manageable prefactor. We present our results upon integrating over λ as detailed above in the section that follows.

1.5.1: Comparison with exact diagonalization results and a look at statistical effects

In Fig. 1.2, we depict results for a system of size $L = N_x \ell$, with $N_x = 10$ sites and a lattice spacing of $\ell = 1$ as in conventional Hubbard-model studies. These calculations include couplings $U/t = 0.5, 1, 2$, and 4, and subsystems of sizes $L_A = 1 - 10$. We compare our results to the results given in Ref. [1], and the agreement we find is quite good.

In order to understand the magnitude of the statistical effects, below, we demonstrate how the averages of interest vary with the number of MC samples in Fig. 1.3. In Fig. 1.3 we see that the total number of samples collected was well beyond what was needed in order to resolve the average: half as many would have already
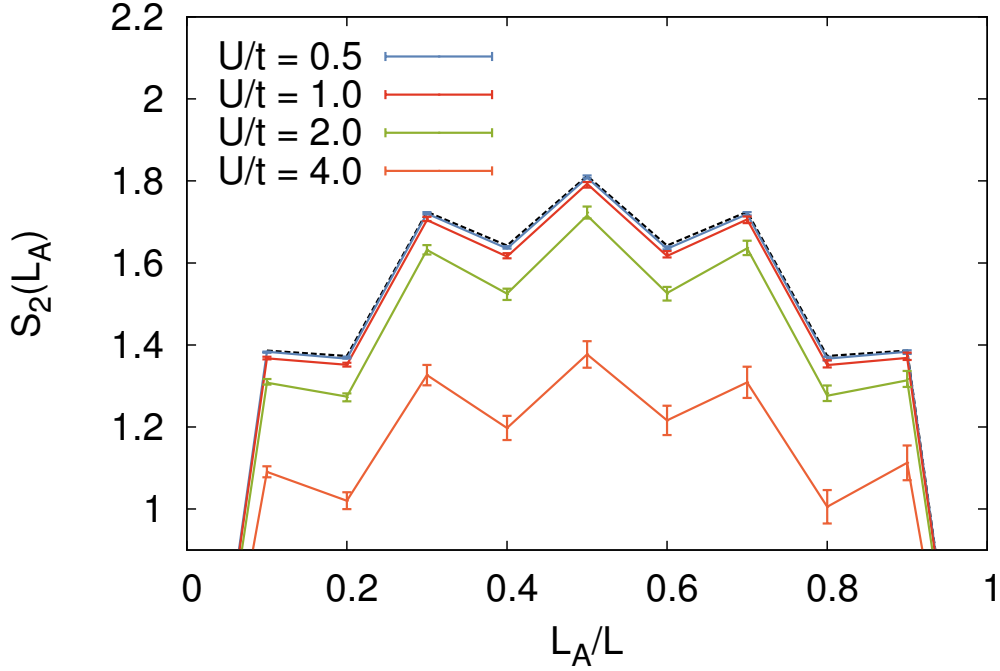
Figure 1.2: Our results for the ten-site Hubbard model with couplings of $U/t = 0.5$, 1.0, 2.0, and 4.0 (unbroken lines from top to bottom). Results for the noninteracting $U/t = 0$ case are shown using a dashed line. Hybrid Monte Carlo results, with numerical uncertainties for 7,500 decorrelated samples, are indicated by the center of their associated statistical error bars. Exact-diagonalization results from Ref. [1] are shown with lines, with the exception of the $U/t = 4.0$ case, where the lines join the central values of our results and are provided to guide the eye.

given exceptional results. These figures show that, by including the entanglement-sensitive factor into the probability measure itself, our approach circumvents the devastating signal-to-noise problem mentioned in the introduction, making the sampling procedure enormously more efficient and the calculation manageable. Below we elaborate more explicitly on statistical effects and on this noise problem, and we include concrete numerical examples of how it arises in calculations.

In Fig. 1.4, we illustrate the overall statistical uncertainty ΔS_2 in our estimates of the entropy S_2 as a function of the number of decorrelated HMC samples N_s, for the coupling strengths and subsystem sizes we studied above. ΔS_2 was computed by using the envelope determined by the MC statistical uncertainties in $\langle \tilde{Q}[\{\sigma\}; \lambda] \rangle$ as a function of λ. While the statistical uncertainty ΔS_2 grows as expected with the sub-system size, its familiar $N_s^{1/2}$ scaling remains constant as the number of samples is increased.

11

1.5.2: Comparison with naïve free-fermion decomposition method

Figure 1.5 depicts again the results for our half-filled, ten-site Hubbard model using 7,500 decorrelated samples for each value of the parameter λ, and this time, it offers a comparison with the naïve free-fermion decomposition method using a comparable 75,000 samples. Such an increased number of samples for the naïve method was selected to offer a more balanced comparison with our method, as the latter technique requires a MC calculation for each value of λ, but those calculations are independent. We used 20 λ points but, as explained in more detail below, roughly half of the λ points require only a small number of samples to achieve reasonable accuracy and precision.

Often, the statistical uncertainties associated with the naïve calculation do not contain the expected values for the entropy. This disagreement is symptomatic of an "overlap" problem, a situation where the probability measure used bears little to no correlation with the observable of interest, as already mentioned once above (see also Ref. [48]). This situation is the same as the signal-to-noise problem referred to in preceding discussions.

To illustrate this issue more precisely, we show in Fig. 2.1 a histogram of $Q[\{\sigma\}]$ [see Eq. (2.7)] for coupling $U/t = 2.0$ and system size $L_A/L = 0.8$. Even after using a logarithmic vertical scale, the distribution of $Q[\{\sigma\}]$ displays an extended tail that survives across numerous orders of magnitude. We find that the distribution is approximately of the log-normal type (that is, its logarithm is approximately distributed as a gaussian, as shown in the inset of Fig. 2.1); this situation presents a great challenge when the average of $Q[\{\sigma\}]$ must be determined with good precision by means of implementing the free-fermion decomposition of Ref. [1] in its purest form. Additionally, we further expect these features to worsen quickly in larger systems, especially in higher dimensions and at stronger couplings, as the matrices involved become more and more ill-conditioned and the scaling of the entropy, as seen in free systems, shifts toward more and more potent divergences of the power-law variety.

We emphasize that it is the logarithm of the average of $Q[\{\sigma\}]$ that determines the quantities of interest, a quantity which could then be obtained by means of the cumulant expansion; however, it is a priori entirely unknown whether such an expansion would converge if it can even be carried out, as there is no knowledge of to what extent the qualities of this distribution deviate from gaussianity.

The log-normality referred to above has often been associated with the HS-field representation of the interaction. In such background fields σ, the orbitals of the trial wavefunction diffuse much like electrons in a disordered medium, and the stronger the interaction (or the lower the temperature) the heavier the tail becomes in the distribution of $Q[\{\sigma\}]$. This interesting effect was observed relatively recently in Ref. [48], and it appears to be quite ubiquitous. It was then shown, phenomenologically, that many signal-to-noise

problems are characterized by the heavy tail of a lognormal distribution (see also, Ref. [49]), and in some cases this behavior has been exploited to provide physical insights.

1.5.3:   Statistical behavior as a function of coupling, region size, and auxiliary parameter

In Fig. 1.7 we give the statistical distribution of our results for the λ derivative for several values of the coupling. These distributions are in most cases approximately gaussian (that is, their tails decay faster than linearly in a log scale), except for the strongest coupling we studied $U/t = 4.0$ where, not entirely unexpectedly, the distribution becomes more asymmetric and develops extended tails relative to its weaker-coupling analogues.

In Fig. 1.8 we show the distribution of our results for the λ derivative at fixed sub-system size and coupling strength, but we vary λ. As stated previously, the parameterization we chose requires considerably fewer decorrelated MC samples at lower λ than at higher λ, as the width of the distributions is much smaller for the former than it is for the latter.

Lastly, in Fig. 1.9 we illustrate the same distribution as above, but as a function of sub-system size. As anticipated, larger subregions are more challenging, but the overall shape of the distributions is very well controlled: it remains close to gaussian in that its tails decay faster than linearly in a log scale, a significant improvement over the distributions shown earlier.

Section 1.6:   Summary and Conclusions

In this chapter, we have described an alternative MC approach to the calculation of the Rényi entanglement entropy of many-fermion systems. A central component of this method is to compute the derivative of the entanglement entropy with respect to an auxiliary parameter and integrate afterwards to compute the difference between the interacting and non-interacting entropies. We have demonstrated that such a derivative can be calculated through a MC method without the previously observed signal-to-noise issues, as the resulting expression yields a probability measure that does not factor across replicas and accounts for entanglement-sensitive correlations in the MC sampling procedure in an efficient, natural way. The required numerical integration can be carried out by any of numerous well-known methods, and in the present case, we computed the required quadratures by means of the Gauss-Legendre rule.

As a test case, we have detailed calculations for the second Rényi entanglement entropy S_2 for a one-dimensional, half-filled Hubbard Hamiltonian for several coupling strengths and compared with values obtained via exact methods. Our calculations show that the statistical uncertainties are very well controlled, as we have shown in numerous plots and histograms. Even though we have not run into numerical stability is-

sues in our tests, we anticipate that those may indeed appear in the manifestation mentioned in Ref. [30, 31]. Our formulation is just as general as the technique proposed in Ref. [1]. Specifically, this chapter's contents can be generalized straightforwardly to finite-temperature algorithms as well as to relativistic systems, in particular those with gauge fields such as QED and QCD, or any other non-Abelian $SU(N)$ gauge theory, systems which have seen enormous success as a result techniques utilized in this chapter.
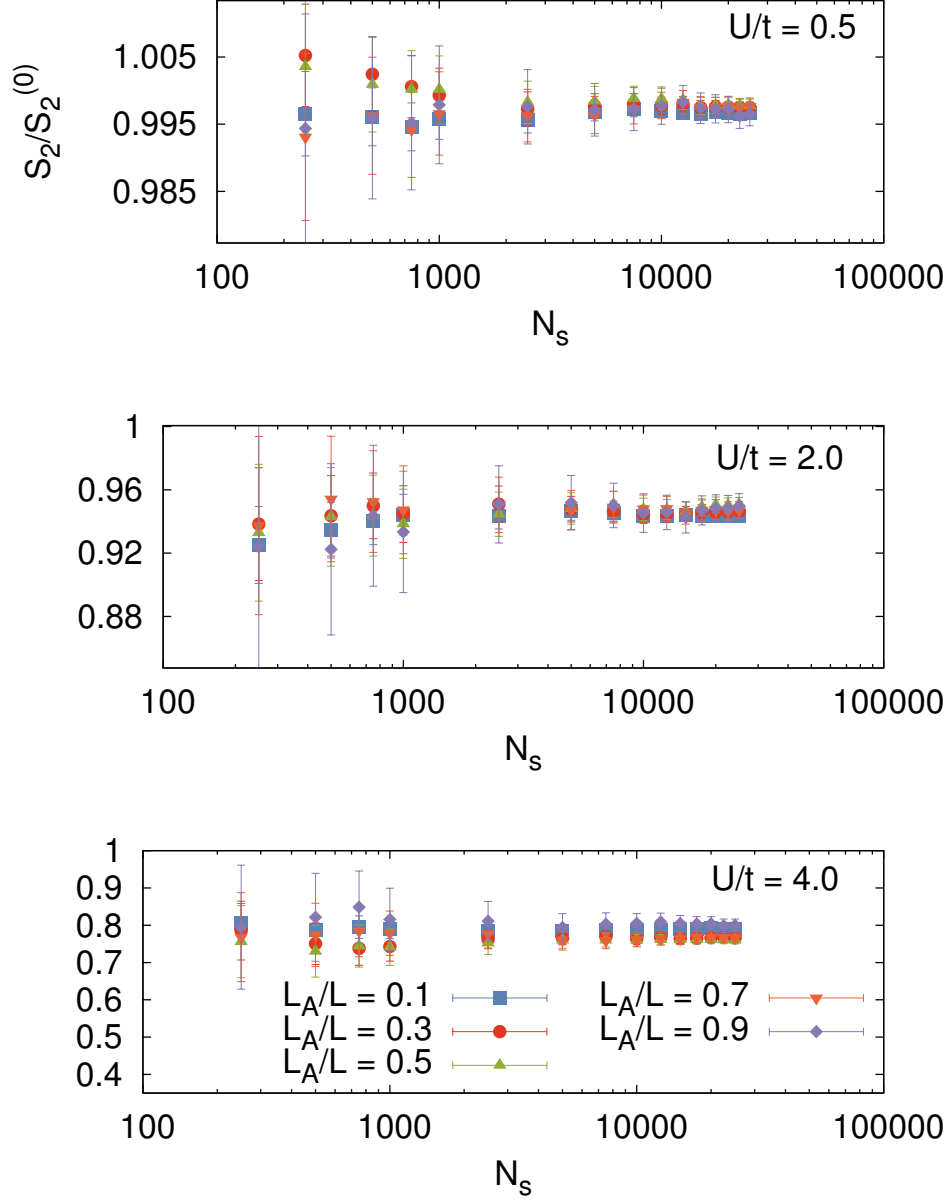
Figure 1.3: Second Rényi entropy (in units of the noninteracting value) as a function of the number of samples N_s for coupling strengths $U/t = 0.5$, 2.0, and 4.0 shown from top to bottom. Within the first few thousand samples, we observe that the results have stabilized comfortably to within 1-2%.
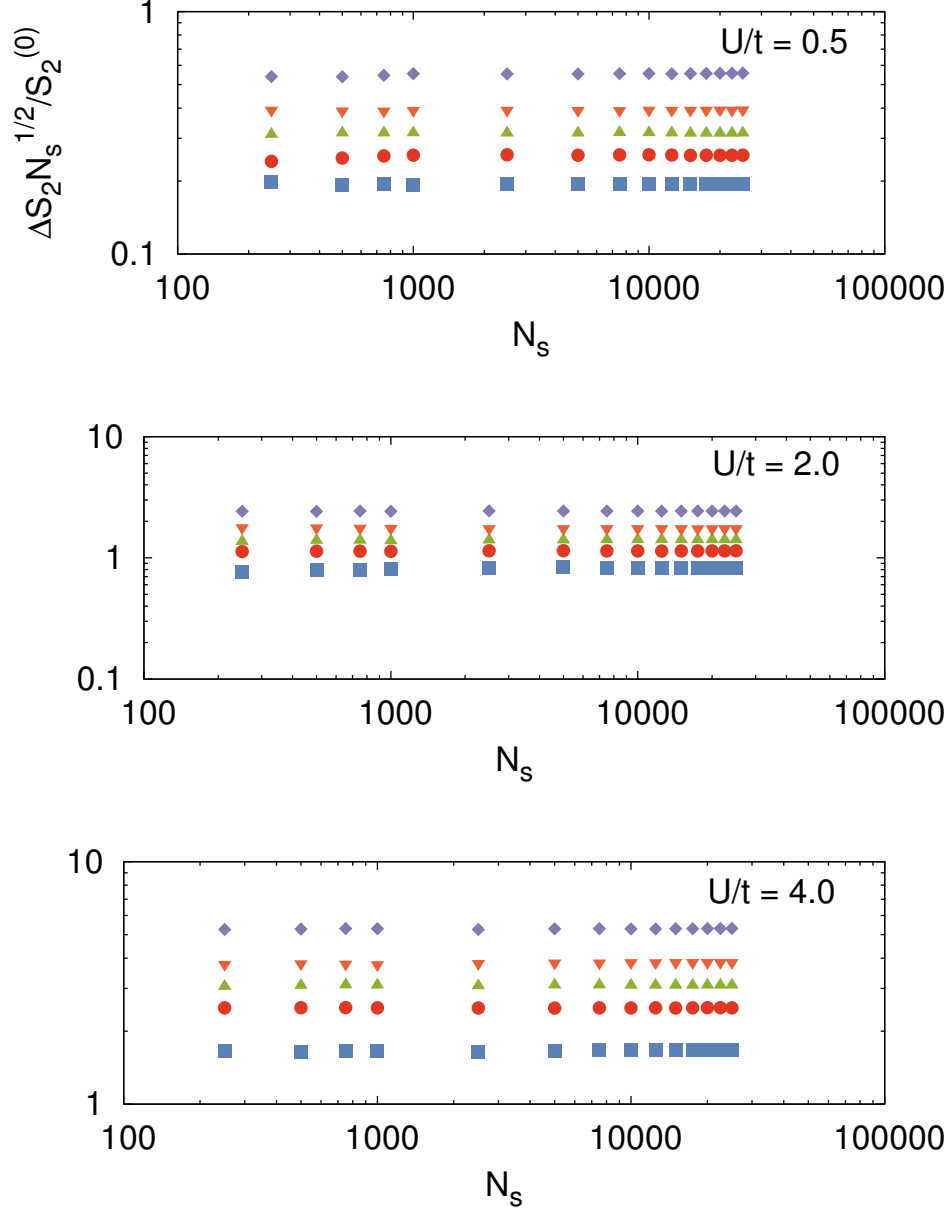
Figure 1.4: Relative statistical uncertainty of the second Rényi entropy (propagated from the standard deviation in the uncertainties on its λ derivative) as a function of the number of decorrelated HMC samples N_s for coupling strengths $U/t = 0.5$, 2.0, and 4.0 shown from top to bottom. The symbols and colors correspond to those utilized above in Fig. 1.3.
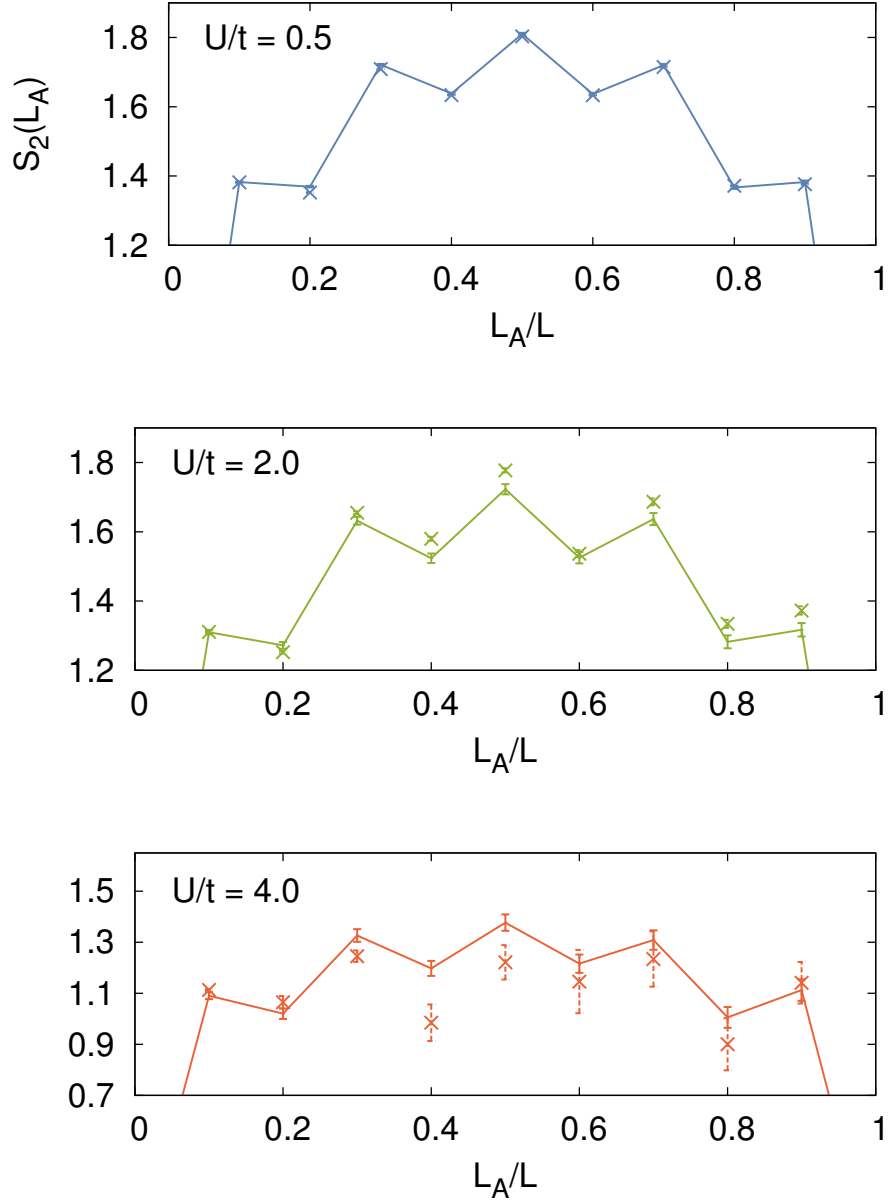
Figure 1.5: Hybrid Monte Carlo results (shown with solid lines) for a ten-site, half-filled Hubbard model with $U/t = 0.5$, 2.0, and 4.0 and with numerical uncertainties for 7,500 decorrelated samples (for each value of λ) compared with results from the naïve free-fermion decomposition method (crosses paired with dashed error bars) with 75,000 decorrelated samples.
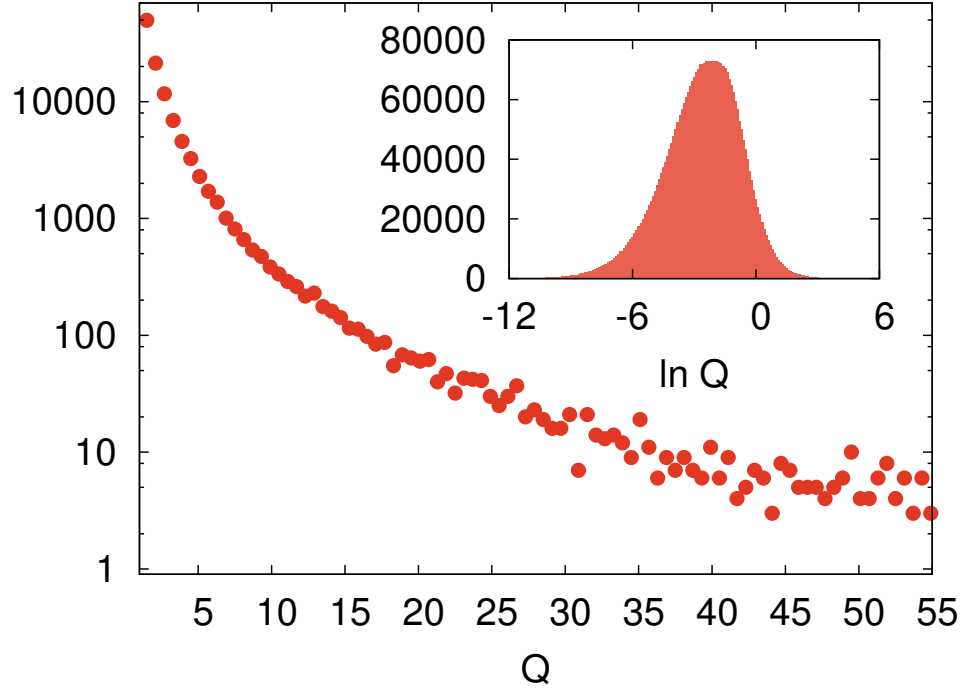
Figure 1.6: The distribution of the natural observable $Q[\{\sigma\}]$ of the naïve free-fermion decomposition method [implemented via Eq. (2.7)] for coupling $U/t = 2.0$ and sub-system size $L_A/L = 0.8$. We emphasize that the quantity $Q[\{\sigma\}]$ is a non-negative one. The extended tail (main plot; note logarithmic scale in vertical axis) extends well beyond the range we have shown, and we find that it is approximately a log-normal distribution, i.e. the quantity $\ln Q[\{\sigma\}]$ is distributed roughly as a gaussian (inset).
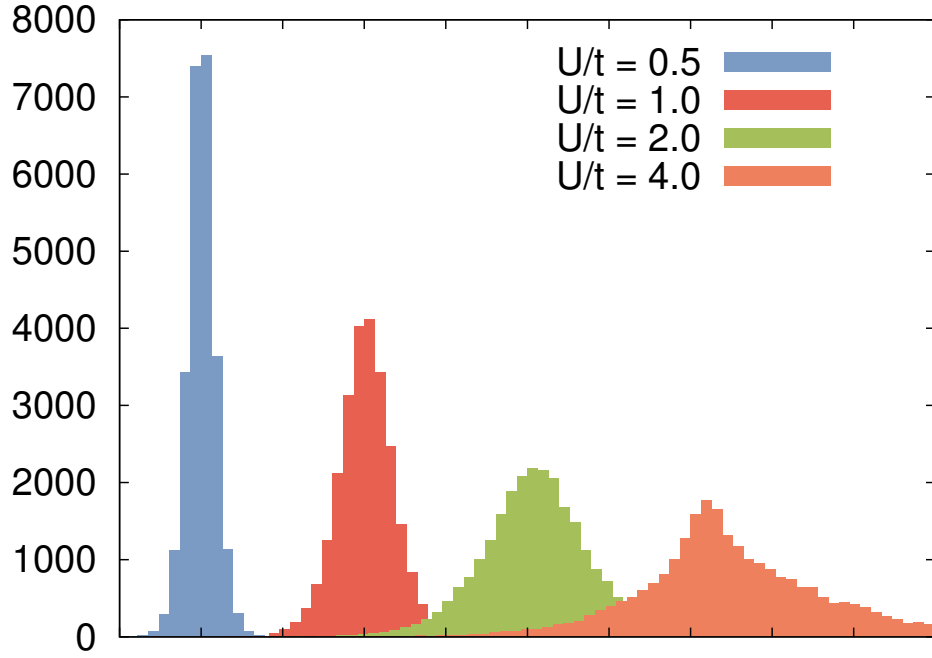
Figure 1.7: A histogram showing the distribution of our results for the derivative $dS_2/d\lambda$ for system size $L_A/L = 0.8$, auxiliary parameter $\lambda \simeq 0.83$, and Hubbard couplings $U/t = 0.5, 1.0, 2.0, 4.0$. The results for different couplings have been offset relative to their true center for display purposes, but the scale is the same for each of them. This figure illustrates that, even though our method addresses the original signal-to-noise issue, strong couplings remain more challenging that weak couplings for reasons common to calculations of this type.
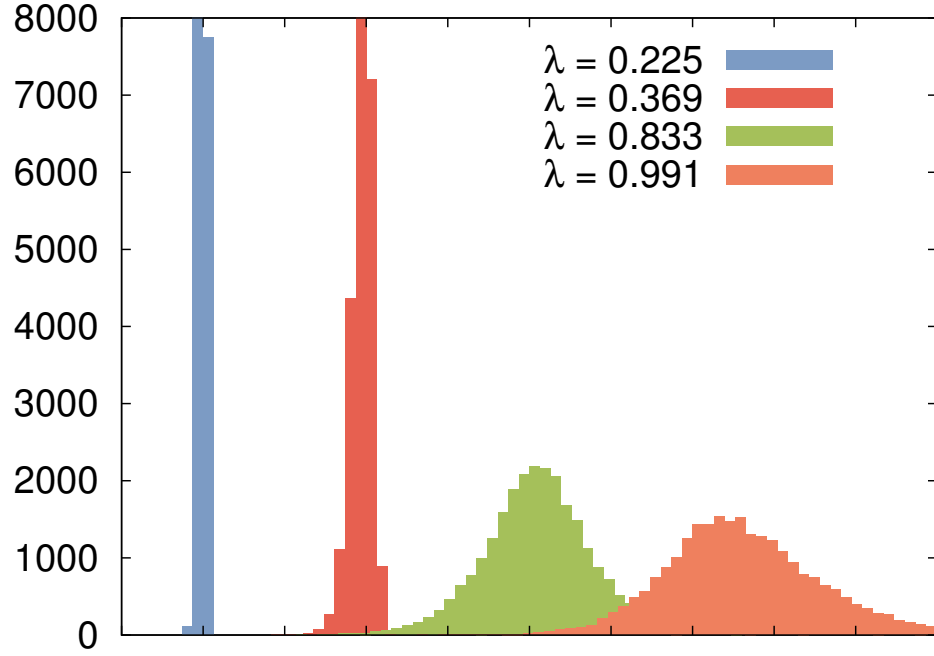
Figure 1.8: Histogram showing the statistical distribution of our results for the derivative $dS_2/d\lambda$ for system size $L_A/L = 0.8$, auxiliary parameter $\lambda \simeq 0.225, 0.369, 0.833, 0.991$, and coupling strength $U/t = 2.0$. Our results for different coupling strengths have been offset for display purposes, but the scale remains the same for each of them. This figure illustrates that lower values of λ require fewer decorrelated MC samples than larger ones in order to determine $\langle \tilde{Q}[\{\sigma\}; \lambda] \rangle$ with acceptable precision.
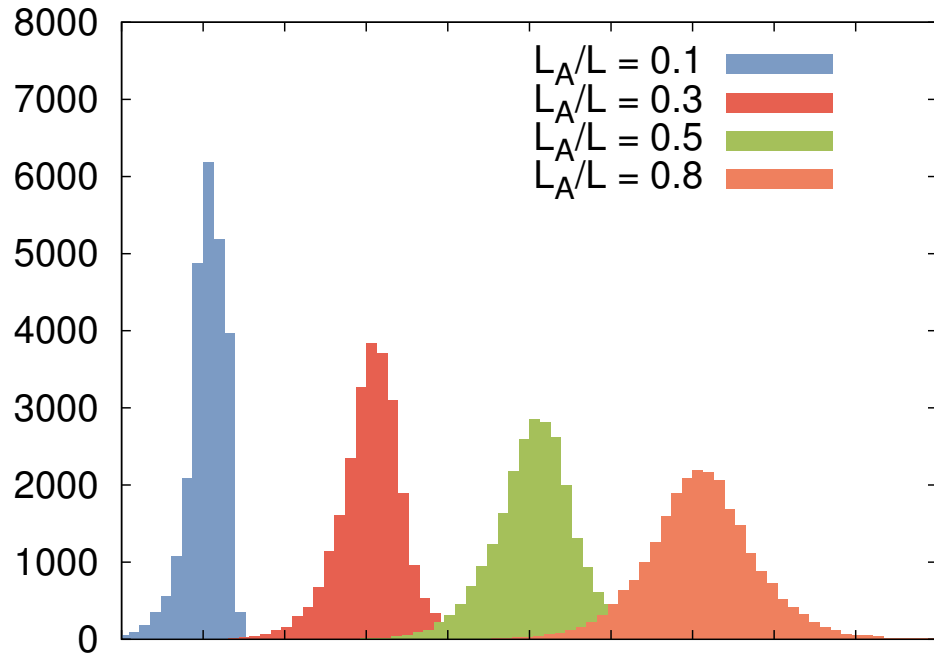
Figure 1.9: A histogram showing the distribution of our results for the derivative $dS_2/d\lambda$ for regions of size $L_A/L =$0.1, 0.3, 0.5, 0.8, auxiliary parameters of $\lambda \simeq 0.83$, and a coupling strength of $U/t = 2.0$. The results for different interaction strengths have been offset for display purposes, but the scale is the same for each of them.

CHAPTER 2:   Higher Order Entropies and a More Stable Algorithm

Section 2.1:   Introduction

In the previous chapter, we detailed an algorithm to calculate the Rényi entanglement entropies S_n of interacting fermion models. Numerous other algorithms have been proposed during the last few years to this effect [16, 21, 22, 24, 25, 26, 28, 29, 27]. This chapter's method, based on Grover's free-fermion decomposition formalism given originally in our Ref. [1], alleviates the signal-to-noise problem present in that algorithm, and our second method is also compatible with the hybrid Monte Carlo (HMC) workhorse [37, 38, 35, 36] extensively utilized in the context of lattice quantum chromodynamics (QCD) and other gauge-field-based simulations. The central point of the last chapter's method is that, by differentiating with respect to an auxiliary parameter λ, one may carry out a Monte Carlo (MC) calculation of $dS_n/d\lambda$ with a probability measure that includes entanglement-sensitive correlations explicitly. [This circumvention was certainly not the case in the approach of Ref. [1], where the probability measure factored completely across the multiple auxiliary field replicas; we identified this factorization as the primary cause of this particular, and particularly devastating, signal-to-noise problem (see discussion that follows)]. After the MC calculation is complete, (numerical) integration with respect to the auxiliary parameter λ returns the desired Rényi entanglement entropy relative to that of a noninteracting system (which is easily computed separately); that is, it returns the contribution to the Rényi entropies coming from the presence of the interactions.

In the present chapter, we detail and benchmark an important improvement upon that Monte Carlo algorithm which, while sharing the properties and central philosophy summarized above, differs from it in two critical regards. Firstly, this chapter's MC method takes advantage of the approximately lognormal characteristics of the underlying statistical distributions of the canonical fermion determinants, which we studied in some detail in the previous chapter, and which we explain in greater detail in the discussion that follows. Additionally, and more importantly, this chapter's algorithm is enormously simpler than its predecessor. While in the latter method the auxiliary parameter λ scaled the coupling constant g (thereby generating a rather involved set of terms upon functional differentiation of the fermion determinant), here the parameter λ is coupled to the number of distinct fermion flavors N_f in a much more accessible way. As we demonstrate in this chapter, our choice not only simplifies the formalism and implementation, but it also highlights the central role of the logarithm of the fermion determinant in our calculation of the Rényi

entropies S_n, and thus brings to the forefront the approximate lognormality property which was mentioned above.

In what follows, we present our basic formalism, review our evidence for approximately lognormal distributions, and explain our method. In addition to the points mentioned above, in our computations we have found the present method to be much more numerically stable than its predecessor in the sense that it functions more smoothly with more lenient MC input parameters. We explain this in detail in this chapter's Results section.

In addition to the new, more elegant method, we demonstrate that it is possible to rewrite part of the formalism in order to bypass the calculation of inverses of the restricted density matrix (see e.g. [28, 29]) in the determination of Rényi entropies of order $n > 2$, a problem highlighted in the literature and one which causes great difficulty in the computation of higher order entropies. To test our method, we computed the $n = 2$ Rényi entropy of the attractive one-dimensional Hubbard model using the previous formalism as well as the new formalism and we checked that we obtained identical results. In going further than the $n = 2$ case, we present results for the $n = 2, 3, 4, \ldots, 10$ Rényi entropies, and we see that higher Rényi entropies display reduced statistical uncertainty in MC calculations. Finally, we attempt an extrapolation to large and small Rényi orders.

Section 2.2:   Basic formalism

As in the previous chapter, we quickly set the stage by presenting the formalism of Grover's method originally put forward in Ref. [1]. The n-th Rényi entropy S_n of a sub-system A of a given model is given by

$$S_n = \frac{1}{1-n} \ln \operatorname{tr}(\hat{\rho}_A^n), \tag{2.1}$$

where $\hat{\rho}_A$ is the reduced density matrix of the sub-system A. For a system with canonical density matrix $\hat{\rho}$, the reduced density matrix is defined via a partial trace over the Hilbert space corresponding to the complement $\bar{A}$ of our sub-system in the full set of quantum numbers:

$$\hat{\rho}_A = \operatorname{tr}_{\bar{A}} \hat{\rho}. \tag{2.2}$$

A convenient auxiliary-field path-integral form for $\hat{\rho}_A$, from which S_n can be computed using a number of MC methods for a wide variety of systems, was presented originally in Ref. [1], which we briefly summarize next for clarity and in an effort to ensure that this chapter is as self-contained as possible.

As is well known from conventional many-body formalism, the full density operator $\hat{\rho}$ can be cast as a

field integral by means of a Hubbard-Stratonovich (HS) auxiliary-field transformation:

$$\hat{\rho} = \frac{e^{-\beta\hat{H}}}{\mathcal{Z}} = \int \mathcal{D}\sigma\, P[\sigma]\, \hat{\rho}[\sigma], \tag{2.3}$$

for a normalized probability measure $P[\sigma]$ determined by the details of the underlying model's Hamiltonian (for more detail, see below and also Ref. [32, 33, 34]). In the above expression, $\mathcal{Z}$ is the partition function, and $\hat{\rho}[\sigma]$ is the density matrix of a system of noninteracting fermions in the fixed external auxiliary field σ. One of the central advances of Ref. [1] was to demonstrate that this decomposition determines not only the full density matrix but also the restricted one and, crucially, all associated one-body correlations. Indeed, Ref. [1] shows that

$$\hat{\rho}_A = \int \mathcal{D}\sigma\, P[\sigma]\, \hat{\rho}_A[\sigma], \tag{2.4}$$

where $P[\sigma]$ is the same probability used in Eq. (2.3),

$$\hat{\rho}_A[\sigma] = C_A[\sigma]\ \exp\left(-\sum_{i,j}\hat{c}_i^\dagger[\ln(G_A^{-1}[\sigma]-1)]_{ij}\hat{c}_j\right), \tag{2.5}$$

and

$$C_A[\sigma] = \det(1 - G_A[\sigma]). \tag{2.6}$$

In the above, we denote by $G_A[\sigma]$ the restricted Green's function of the free system in the external background field σ (see below), and $\hat{c}^\dagger$, $\hat{c}$ are the fermion creation and annihilation operators. The sums in the exponent of Eq. (2.5) range over those points in the system which belong to the subsystem A.

By using the above formalism for the case of $2N$-component fermions, the Rényi entropy (c.f. Eq. 2.1) becomes

$$\exp\left((1-n)S_n\right) = \int \mathcal{D}\{\sigma\}P[\{\sigma\}]\, Q[\{\sigma\}], \tag{2.7}$$

where the field integration measure, given by

$$\mathcal{D}\{\sigma\} = \prod_{k=1}^{n}\frac{\mathcal{D}\sigma_k}{\mathcal{Z}}, \tag{2.8}$$

is over the n "replicas" σ_k of the auxiliary field which result from taking the n-th power of the path integral

representation of $\hat{\rho}_A$ shown above, and the normalization

$$\mathcal{Z} = \int \mathcal{D}\sigma \prod_{m=1}^{2N} \det U_m[\sigma] \qquad (2.9)$$

was included in the measure. It is worth explicitly mentioning that, by separating out a factor of $\mathcal{Z}^n$ in the denominator of Eq. (2.7), an explicit form can be identified in the numerator as in the replica trick [14], which corresponds to a "replica" partition function for n copies of the system, "glued" together in the region A as a result of the particular structure of the matrix product and partial trace.

The naïve probability measure, namely

$$P[\{\sigma\}] = \prod_{k=1}^{n} \prod_{m=1}^{2N} \det U_m[\sigma_k], \qquad (2.10)$$

factorizes completely across replicas, which makes it largely insensitive to entanglement-oriented correlations. This factorization is the central reason why using $P[\{\sigma\}]$ as the MC probability leads to signal-to-noise problem (see Ref. [1]). In Eq. (2.10), $U_m[\sigma]$ encodes the dynamics of the m-th fermion species, including the kinetic energy and the form of the interaction after a Hubbard-Stratonovich transformation. This matrix also encodes the form of the trial state $|\Psi\rangle$ in imaginary-time-projective, ground-state approaches (see e.g. Ref. [32, 33, 34]), a version of which we use here; in what follows, we have taken $|\Psi\rangle$ to be a Slater determinant of single-particle orbitals. In finite-temperature approaches, $U_m[\sigma]$ is obtained by evolving a complete set of single-particle states in imaginary time.

The quantity that contains the critical input to the entanglement entropy is the determinant

$$Q[\{\sigma\}] = \prod_{m=1}^{2N} \det M_m[\{\sigma\}], \qquad (2.11)$$

which we refer to below as the "entanglement determinant," and where the matrix $M_m[\{\sigma\}]$ is given by

$$M_m[\{\sigma\}] \equiv \prod_{k=1}^{n} \left(1 - G_{A,m}[\sigma_k]\right) \times \left[1 + \prod_{l=1}^{n} \frac{G_{A,m}[\sigma_l]}{1 - G_{A,m}[\sigma_l]}\right]. \qquad (2.12)$$

The quantity $Q[\{\sigma\}]$ assumed the role of an observable in Ref. [1], which is a natural interpretation considering Eq. (2.7). Nevertheless, we will interpret this product differently in the discussion below. Besides the replica fields, the new component in the determination of S_n is again the *restricted Green's function* $G_{A,m}[\sigma_k]$. This quantity is the same as the free one-body density matrix $G(x, x')$ of the m-th fermion species in the external potential σ_k, but the spatial arguments x, x' are restricted to the region A and the operator's size is reduced

to match (see Ref. [1] and also Ref. [43, 44, 45], where expressions were originally derived for the reduced density matrix of noninteracting systems, based on reduced Green's functions).

Section 2.3:   Avoiding inversion of the reduced Green's function for $n > 2$

Addressed explicitly in Ref. [30, 31], for $n = 2$, no inversion of the difference $1 - G_{A,m}[\sigma_k]$ is actually required in the calculation of the entanglement determinant $Q[\{\sigma\}]$, as straightforward calculation immediately confirms that the equations simplify in that case. However, for higher n it is not at all obvious how to avoid such an inversion or if it can be avoided at all. Below, we demonstrate that this calculation can indeed be accomplished without performing this troublesome inversion. We begin by factoring the entanglement determinant such that

$$\det M_m[\{\sigma\}] = \det L_m[\{\sigma\}]\det K_m[\{\sigma\}], \tag{2.13}$$

where $L_m[\{\sigma\}]$ is a block diagonal matrix (one block per replica k):

$$L_m[\{\sigma\}] \equiv \text{diag}\left[1 - G_{A,m}[\sigma_k]\right], \tag{2.14}$$

and

$$K_m[\{\sigma\}] \equiv \begin{pmatrix} 1 & 0 & 0 & \dots & 0 & -R[\sigma_n] \\ R[\sigma_1] & 1 & 0 & \dots & \vdots & 0 \\ 0 & R[\sigma_2] & 1 & 0 & 0 & 0 \\ \vdots & \ddots & \ddots & \ddots & 1 & \vdots \\ 0 & \dots & \dots & 0 & R[\sigma_{n-1}] & 1 \end{pmatrix}, \tag{2.15}$$

where the ones in the above are identity matrices and where we have defined

$$R[\sigma_k] = \frac{G_{A,m}[\sigma_k]}{G_{A,m}[\sigma_k] - 1}. \tag{2.16}$$

The equivalence of the determinants in Eq. (2.13) can be shown in a straightforward fashion: the $L_m[\{\sigma\}]$ factor is easily understood, as that matrix is block diagonal and therefore its determinant reproduces the

first r.h.s. factor in the first line of Eq. (2.12); the remaining factor relies on the identity

$$\det \begin{pmatrix} 1 & 0 & 0 & \dots & 0 & H_k \\ -H_1 & 1 & 0 & \dots & \vdots & 0 \\ 0 & -H_2 & 1 & 0 & 0 & 0 \\ \vdots & \ddots & \ddots & \ddots & 1 & \vdots \\ 0 & \dots & \dots & 0 & -H_{k-1} & 1 \end{pmatrix} = \det\left(1 + H_1 H_2 \dots H_k\right), \tag{2.17}$$

which is valid for arbitrary block matrices H_j, is a standard result often used in many-body physics (especially when implementing a Hubbard-Stratonovich transformation), and can be shown using so-called elementary operations on rows and columns.

Within the determinant of Eq. (2.13), we multiply $K_m[\sigma]$ and $L_m[\sigma]$:

$$T_m[\{\sigma\}] \equiv K_m[\{\sigma\}]L_m[\{\sigma\}] = 1 - \mathcal{G}_m[\{\sigma\}]B, \tag{2.18}$$

where $\mathcal{G}_m[\{\sigma\}]$ is a block diagonal matrix defined by

$$\mathcal{G}_m[\{\sigma\}] = \text{diag}\left[G_{A,m}[\sigma_n]\right], \tag{2.19}$$

and

$$B \equiv \begin{pmatrix} 1 & 0 & 0 & \dots & -1 \\ 1 & 1 & 0 & \dots & 0 \\ 0 & 1 & 1 & \dots & 0 \\ \vdots & \ddots & \ddots & \ddots & \vdots \\ 0 & \dots & 0 & 1 & 1 \end{pmatrix} \tag{2.20}$$

where again the ones given in the above are identity matrices. Equation (2.18) proves our claim, as we may use $T_m[\{\sigma\}]$ in our calculations instead of $M_m[\{\sigma\}]$, and the former contains no inverses of $1 - G_{A,m}$ greatly simplifying the calculation of higher order entropies.

Summarizing, a class of approaches to calculating S_n for $n > 2$, based on the Hubbard-Stratonovich representation of $\hat{\rho}_A$ (also known as free-fermion decomposition), requires computing $M_m[\{\sigma\}]$, which in turn requires inverting $1 - G_{A,m}$ per Eq. (2.12). By arriving at Eq. (2.18), and given that

$$\det T_m[\{\sigma\}] = \det M_m[\{\sigma\}], \tag{2.21}$$

27

[Eq. (2.13) and beyond] we have demonstrated that no inversions are actually required, as $T_m[\{\sigma\}]$ contains no inverses and because its determinant is equivalent to the original, more computationally unstable, form. While this is a desirable feature from a numerical point of view, it should be mentioned that, from a computational-cost point of view, the price of not inverting $1 - G_{A,m}$ reappears in the fact that T_m, though sparse, scales linearly with n in size.

For the remainder of this chapter, all calculations carried out at $n = 2$ use the M-approach, which is based on Eq. (2.12) and the 'proposed method' described below. We reproduced those results by switching to the T-approach, which uses Eq. (2.18) (as well as the method described below), and we then proceeded to higher n with the latter formulation.

Section 2.4: A statistical observation: lognormal distribution of the entanglement determinant

In the previous chapter, we offered examples of the approximate log-normal distributions obeyed by $Q[\{\sigma\}]$ when sampled according to the naïve measure $P[\{\sigma\}]$. One specific example is reproduced here for reference in Fig. 2.1. The fact that such statistical distributions are approximately log-normal, at least visually, strongly suggests that one may use the cumulant expansion to determine S_n. Generally,

$$
\begin{aligned}
(1-n)S_n &= \ln \int \mathcal{D}\{\sigma\} P[\{\sigma\}] \, Q[\{\sigma\}] \\
&= \sum_{m=1}^{\infty} \frac{\kappa_m[\ln Q]}{m!},
\end{aligned}
\tag{2.22}
$$

where $\kappa_m[\ln Q]$ is the m-th cumulant of $\ln Q$, and the first two nontrivial cumulants are given by

$$
\kappa_1[X] = \langle X \rangle
\tag{2.23}
$$

and

$$
\kappa_2[X] = \langle X^2 \rangle - \langle X \rangle^2
\tag{2.24}
$$

for a given functional $X[\{\sigma\}]$, and where the expectation value denoted here as $\langle \cdot \rangle$ is taken with respect to the natural produce measure $P[\{\sigma\}]$. If the distribution of $\ln Q$ were truly normal, the above series would end after only the initial two terms, and this simplicity would provide us with an efficient means of bypassing signal-to-noise issues in the determination of S_n via stochastic methods [48]. Unfortunately but unsurprisingly, the statistical distribution is not exactly normal. Moreover, the cumulants beyond $m = 2$ more often than not show extreme sensitivity to the details of the underlying distribution (i.e. they can
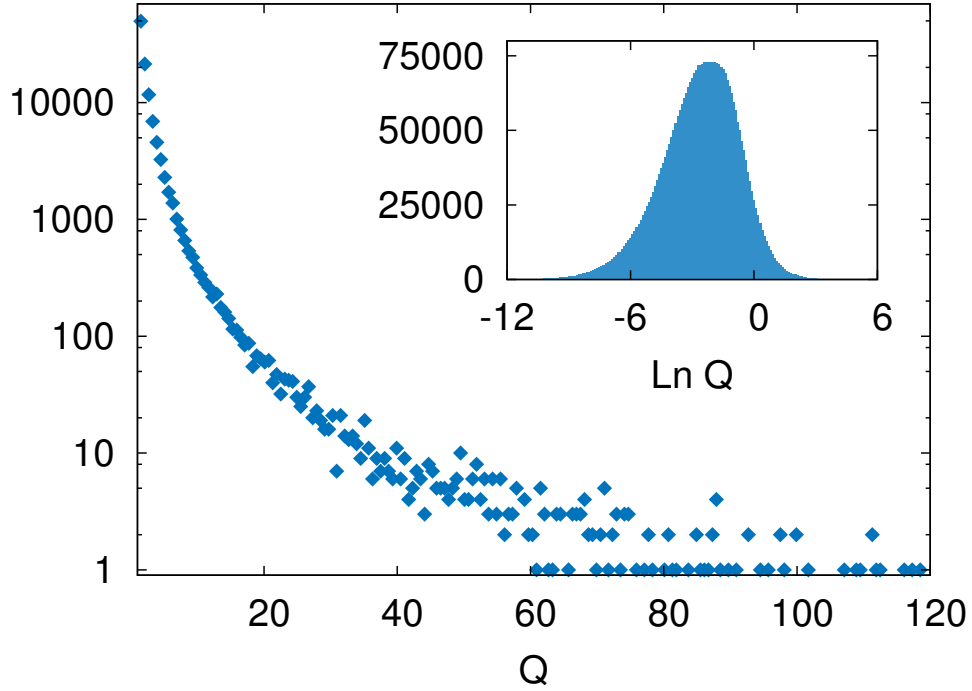
Figure 2.1: Statistical distribution of the observable $Q[\{\sigma\}]$ of the naïve free-fermion decomposition method, i.e. using Eq. (2.7), for a ten-site, one-dimensional Hubbard model described by Eq. (2.33), at an attractive coupling of $U/t = 2.0$ and for a subsystem of size $L_A/L = 0.8$. In our case, $Q[\{\sigma\}]$ is a strictly non-negative quantity. The extended tail in the main plot (note logarithmic scale in vertical axis) is approximately a log-normal distribution [i.e. $\ln Q[\{\sigma\}]$ is roughly a normal distribution (see inset)].

fluctuate wildly across a huge range of scales), they are very difficult to determine stochastically (the signal-to-noise problem re-emerges in a different form), and there is currently no easy way to obtain clean analytic insight into the large-m behavior of κ_m. Nevertheless, this approximate log-normality does provide a path forward, as it indicates that we may still evaluate $\langle \ln Q \rangle$ to good precision with MC methods. As we will demonstrate in the next sections, this evaluation is enough to determine S_n if we are willing to pay the price of a one-dimensional integration on a compact domain.

Although (approximate) lognormality in the entanglement determinant seems very difficult to prove analytically in the present case, evidence of its appearance has been found in systems as different as ultracold atoms and relativistic gauge theories [48, 49]. Again, the underlying reason for this distribution appears to be connected to a similarity between the motion of electrons in disordered media and lattice fermions in the external auxiliary (gauge) field present in MC calculations.

Section 2.5:   Proposed method

Beginning from the right side of Eq. (2.7), we introduce an auxiliary variable $0 \leq \lambda \leq 1$ and define a new function $\Gamma(\lambda; g)$, analogous to the one defined in the previous chapter, via

$$\Gamma(\lambda; g) \equiv \int \mathcal{D}\{\sigma\} P[\{\sigma\}] \, Q^\lambda[\{\sigma\}]. \tag{2.25}$$

At $\lambda = 0$,

$$\ln \Gamma(0; g) = 0, \tag{2.26}$$

while at $\lambda = 1$, $\Gamma(\lambda; g)$ provides the full Rényi entanglement entropy:

$$\frac{1}{1-n} \ln \Gamma(1; g) = S_n. \tag{2.27}$$

From Eq. (3.84),

$$\frac{\partial \ln \Gamma}{\partial \lambda} = \int \mathcal{D}\{\sigma\} \tilde{P}[\{\sigma\}; \lambda] \, \ln Q[\{\sigma\}] \tag{2.28}$$

where

$$\tilde{P}[\{\sigma\}; \lambda] = \frac{1}{\Gamma(\lambda; g)} P[\{\sigma\}] \, Q^\lambda[\{\sigma\}]. \tag{2.29}$$

With an even number of species $2N$ and with attractive interactions, the quantities $P[\{\sigma\}]$ and $Q[\{\sigma\}]$ are wholly real and strictly non-negative for all fields σ, such that there is no sign problem and such that $\tilde{P}[\{\sigma\}; \lambda]$ above is a well-defined and normalized probability measure.

As in the previous chapter, using this, we can compute S_n by taking the initial $\lambda = 0$ point as a reference and computing the entropy from

$$S_n = \frac{1}{1-n} \int_0^1 d\lambda \, \langle \ln Q[\{\sigma\}] \rangle_\lambda, \tag{2.30}$$

where we have defined

$$\langle X \rangle_\lambda = \int \mathcal{D}\{\sigma\} \tilde{P}[\{\sigma\}; \lambda] \, X[\{\sigma\}]. \tag{2.31}$$

Thus, we arrive at an integral form for the fully interacting Rényi entanglement entropy that can be computed using any MC method (see e.g. [32, 33, 34]), in particular HMC [35, 36, 37, 38].

As in the last chapter, we emphasize that the expectation values above are computed with respect to the augmented probability measure $\tilde{P}[\{\sigma\}; \lambda]$, which communicates correlations responsible for entanglement and differs for each value of the parameter λ. In stark contrast to the usual MC probability $P[\{\sigma\}]$ consisting of the usual fermion determinant, which corresponds to statistically independent copies of the Hubbard-
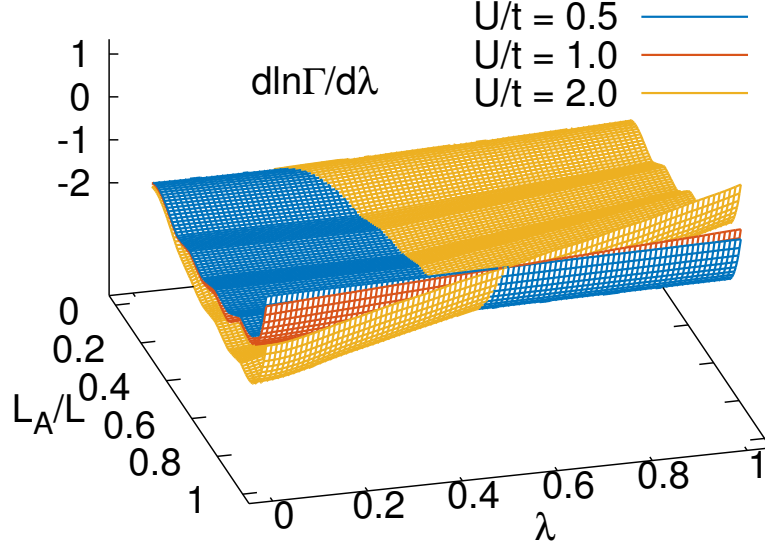
Figure 2.2: Stochastic results for $\langle \ln Q[\{\sigma\}] \rangle_\lambda$ with $n = 2$ for coupling strengths of $U/t = 0.5, 1.0$, and 2.0 as functions of the auxiliary parameter λ and the region size L_A/L for a ten-site, one-dimensional Hubbard model.

Stratonovich field, this admittedly more complicated statistical distribution does not exhibit the factorization responsible for the signal-to-noise problems present in the approach as it was originally written down.

Making use of Eq. (3.89) requires a Monte Carlo method to evaluate the expectation value $\langle \ln Q[\{\sigma\}] \rangle_\lambda$ as a function of λ, followed by numerical integration over this superfluous parameter. As in the last chapter, we see here that $\langle \ln Q[\{\sigma\}] \rangle_\lambda$ is a surprisingly smooth function of λ, which is essentially linear in the present case. It is therefore sufficient to perform the numerical integration using a uniform grid rather than a specialized quadrature as was done above. In the chapter that follows, we will again find surprisingly linear behavior as a function of λ and will use a uniform grid in that case as well. The stochastic evaluation of the source $\langle \ln Q[\{\sigma\}] \rangle_\lambda$, for fixed subregion A, can be expected to feature roughly symmetric fluctuations about the mean, and as a consequence, the statistical effects on the entropy are reduced after integrating over λ as is typical with such calculations.

Finally, we note an interesting and straightforward application of Jensen's inequality at $\lambda = 0$. At that

point

$$\left.\frac{\partial \ln \Gamma}{\partial \lambda}\right|_{\lambda=0} = \int \mathcal{D}\{\sigma\} P[\{\sigma\}] \ln Q[\{\sigma\}] \tag{2.32}$$

$$\leq \ln \int \mathcal{D}\{\sigma\} P[\{\sigma\}] Q[\{\sigma\}] = (1-n)S_n,$$

which must be satisfied by our calculations. Our Monte Carlo results at $\lambda = 0$ do indeed satisfy this bound.

Section 2.6: Results

2.6.1: Second Rényi entropy

As a first test of our algorithm and in efforts to make contact with previous work [1], we begin by showing results for the second Rényi entropy S_2 for the one-dimensional, half-filled Hubbard model with periodic boundary conditions, whose Hamiltonian operator is

$$\hat{H} = -t \sum_{s,\langle ij \rangle} \left(\hat{c}_{i,s}^\dagger \hat{c}_{j,s} + \hat{c}_{j,s}^\dagger \hat{c}_{i,s} \right) + U \sum_i \hat{n}_{i\uparrow} \hat{n}_{i\downarrow}, \tag{2.33}$$

where the first sum includes species $s = \uparrow, \downarrow$ and all pairs of adjacent lattice sites. As before, we make use of a symmetric Trotter-Suzuki decomposition of the canonical Boltzmann weight, with an imaginary-time discretization parameter of $\tau = 0.05$ (given in lattice units). As described earlier, the many-body interacting factor in the Trotter-Suzuki approximation was implemented by introducing a "replica" auxiliary field σ for each required power of the reduced density matrix. As in the chapter before, we implemented a Hubbard-Stratonovich transformation of a compact continuous form [32, 33, 34], one of many known options.

We offer plots for the source $\langle \ln Q[\{\sigma\}] \rangle_\lambda$ with $n = 2$ in Fig. 2.2. In contrast to the results depicted in the previous chapter and as described above, the resulting expectation boasts stunningly little curvature as the subsystem size L_A is increased and is shockingly linear as a function of the auxiliary parameter λ. Even after twice doubling the strength of the interaction, the curvature of constant-subsystem-size slices is increased only marginally. We note that if one assumes such benign curvature is a somewhat universal feature, at least for weakly-coupled systems, our method provides a means by which to rapidly estimate the entanglement entropy for a large portion of parameter space at the very least yielding a qualitative picture of its behavior as a function of the physically relevant input parameters.

We observe that this surface displays almost no torsion, its dominant features being those present even in the noninteracting case i.e. an alternating shell-like structure as a function of the subsystem size. Moving toward larger region sizes, we observe a combination of twisting and translation culminating in the required,

and somewhat delicate, cancellation upon reaching the full system size. Presented with this relatively forgiving geometry, we performed the required integration via cubic-spline interpolation. Using a uniformly spaced lattice of size $N_\lambda = 20$ points, we determine the desired entropy to a precision limited by statistical rather than systematic considerations demonstrating below that the statistical uncertainties themselves are also well-controlled.

2.6.2: Comparison to exact diagonalization

Depicted in Fig. 2.3 are results for a system of size $L = N_x \ell$ with a number of sites $N_x = 10$. For coupling strengths $U/t = 0.5, 1.0, 2.0$ and 4.0 and for region sizes $L_A = 1, 2, \ldots, 10$, we find good agreement with previous calculations in Ref. [1] and the previous chapter, and as in the former, we observe convergence rather quickly with only $O(10^3)$ decorrelated samples as can be seen in Fig. 2.4. Further, for large sample sizes N_s, we observe that the standard error in the entropy ΔS_2, computed from the envelope defined by the MC uncertainty in the source $\langle \ln Q[\{\sigma\}] \rangle_\lambda$ for at each value in (L_A, λ)-space, scales asymptotically as $\Delta S_2 \sim 1/\sqrt{N_s}$ up to noninfluential corrections.

2.6.3: Results for $n \neq 2$

In this section, we extend the results presented in the above discussion to Rényi orders $n = 3, 4, 5, \ldots, 10$. To highlight the contrasting points between $n = 2$ and $n > 2$, we show in Fig. 2.5 the Rényi entropies S_n for $n = 2, 3, 4$ (top to bottom) of the same 1D attractive Hubbard model, as obtained with our method and the reformulation of the fermion determinant shown in Eq. (2.18).

As clear from the figure, increasing n leads always to lower values of S_n at fixed subsystem size L_A/L consistent with knowledge that the Rényi entropy is a nonincreasing function of its order. However, increasing n also amplifies the fluctuations as a function of L_A/L. Interestingly, the approach of our system to the large-n regime is quite rapid, and after only the first few orders, the difference between consecutive entropies is only marginal at best, most obviously so at weak coupling. We also observe that, as n is increased, the statistical fluctuations that define the error bars appear to be progressively more suppressed, which is particularly evident for the strongest coupling we studied, namely $U/t = 4.0$.

At the level of the auxiliary function $\langle \ln Q[\{\sigma\}] \rangle_\lambda$, we again see very predictable changes in the geometry of this surface as a function both its arguments as shown in Fig. 2.6. At particle content and coupling strength, increasing the Rényi order results in a tilting effect reminiscent of that seen previously with increasing coupling, but rather than being localized away from vanishing subsystem size, the change is much more global, affecting all subsystems in a qualitatively similar fashion and leaving each surface's

characteristic quasi-linearity in λ intact. Although the shell-like structure present in this function's L_A dependence is amplified, this increased fluctuation affects the quality of the results negligibly at most, as again, the geometry remains accessible to fairly naive quadratures.

Given the data shown above, we would be borderline negligent if we did not attempt an extrapolation not only to the limit of infinite Rényi order S_∞, but also to the von Neumann entropy, despite knowledge of the formidable challenges presented by these extrapolations, particularly in the case of the von Neumann entropy. The former limit provides a lower bound on all finite-order entropies, whereas the latter is of interest to a variety of disciplines and has proven quite difficult to study. At fixed coupling and with the knowledge that the Rényi entropy is nonincreasing in the order, we found that our results at each fixed region size and at every studied coupling were well-characterized by simple exponential decays.

Interestingly, the relative speed of this decay alternates as a function of the region size as can be seen in Fig. 2.7. Regions corresponding to an even number of lattice sites demonstrate a much more sudden initial decay than do those regions comprised of an odd number of sites. This peculiar oscillation results in an inverted shell structure for the extrapolation to $n = 1$, in contrast to the case where $n \to \infty$ in which this feature is preserved. A representative example of this procedure is shown in Fig. 2.8.

Section 2.7:   Summary and Conclusions

We have presented a technique designed to compute the entanglement entropy of strongly interacting fermions which takes advantage of an approximate log-normality property of the statistical distribution of the canonical fermion determinants. The above approach overcomes the signal-to-noise problem of naïve formulations, and it is very close in its central idea to the method proposed in the previous chapter: both methods involve defining an auxiliary parameter λ, differentiating with respect to this parameter, and then integrating it out to recover the full entropy S_n after a MC calculation. The order of the steps is important, as the differentiation with respect to λ induces the appearance of entanglement-sensitive contributions in what can be used as MC probability measure. Beyond those similarities, the present method has the distinct advantages of being simultaneously simpler to formulate (algebraically as well as computationally) and of explicitly using the approximate log-normality property. Moreover, we have found that the λ integration step displays clearly more stable numerical behavior in the present approach than in its predecessor: it is approximately linear in the present case and markedly not so in the original incarnation. We therefore strongly advocate using the present algorithm over the former.

In this chapter, in addition to presenting an improved method, we have put forward a straightforward algebraic reformulation of the equations which, while exactly equivalent to the original formalism, avoids the

numerical burden and complication of computing inverses of nearly singular restricted Green's functions in the calculation of n-th order Rényi entropies for $n > 2$. This problem had been pointed out by us and others (see e.g. Ref. [30, 31]) as a stumbling block, as it is perfectly possible for those matrices to be singular.

As a test case for our algorithm, we have presented results for the Rényi entanglement entropies S_n of the half-filled, one-dimensional Hubbard model with periodic boundary conditions. The present and previous formalisms were used for calculations at $n = 2$, which matched exactly. The rewritten form based on the simpler Eq. (2.18) was then used to extend our computations to higher-order cases with $n = 3, 4, \ldots, 10$, allowing us to attempt extrapolations in the Rényi order in both directions.

Our results demonstrate that, with increasing Rényi order n, the value of S_n decreases as expected for all L_A/L, but the fluctuations as a function of L_A/L become much more pronounced. Surprisingly, the statistical MC fluctuations decrease as n is increased. Since the problem we set out to solve was in fact statistical in nature, our observations indicate that calculations for large systems and in higher dimensions will benefit from pursuing Rényi orders $n > 2$.
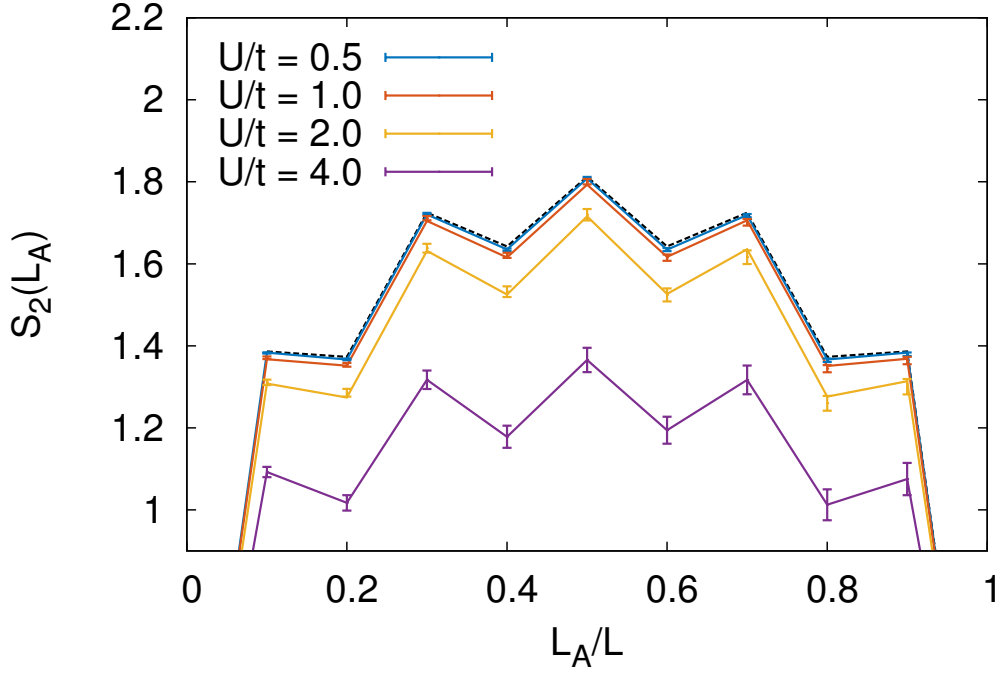
Figure 2.3: Results for the ten-site, one-dimensional Hubbard model for coupling strengths of $U/t = 0.5, 1.0, 2.0,$ and 4.0 for 7,500 MC samples with associated numerical uncertainties shown. Results for $U/t = 0$ are depicted as a dashed line (black). For each but the largest coupling, results obtained via exact diagonalization from Ref. [1] are indicated by solid lines, whereas for the largest coupling, we provide a line joining the central values of our result to emphasize that its shape is consistent with results for the former and to guide the eye.
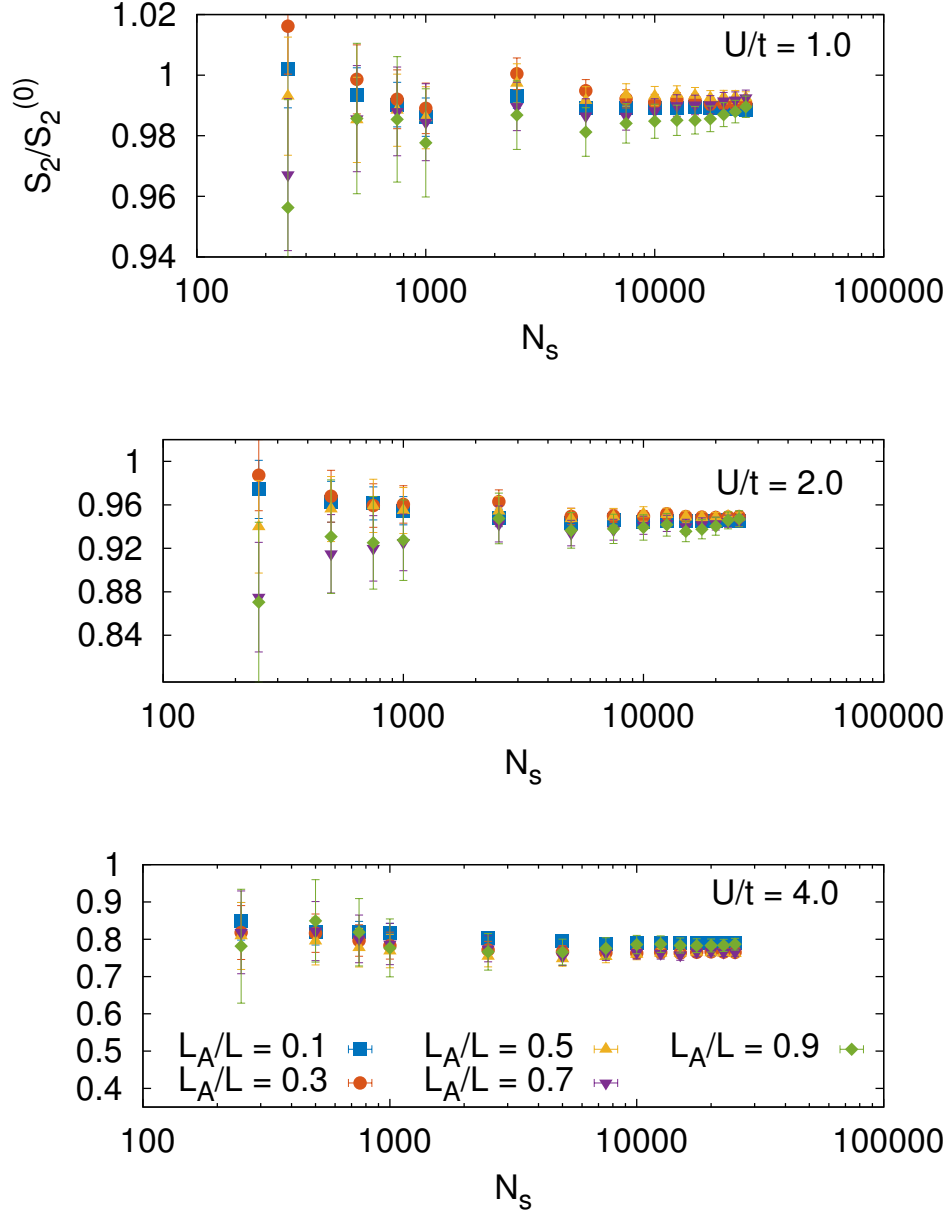
Figure 2.4: The second Rényi entanglement entropy S_2 in units of the result for a free system plotted as a function of the number of samples N_s for coupling strengths $U/t = 0.5, 1.0, 2.0,$ and 4.0 demonstrating convergence to within a few percent within the first ten thousand samples.
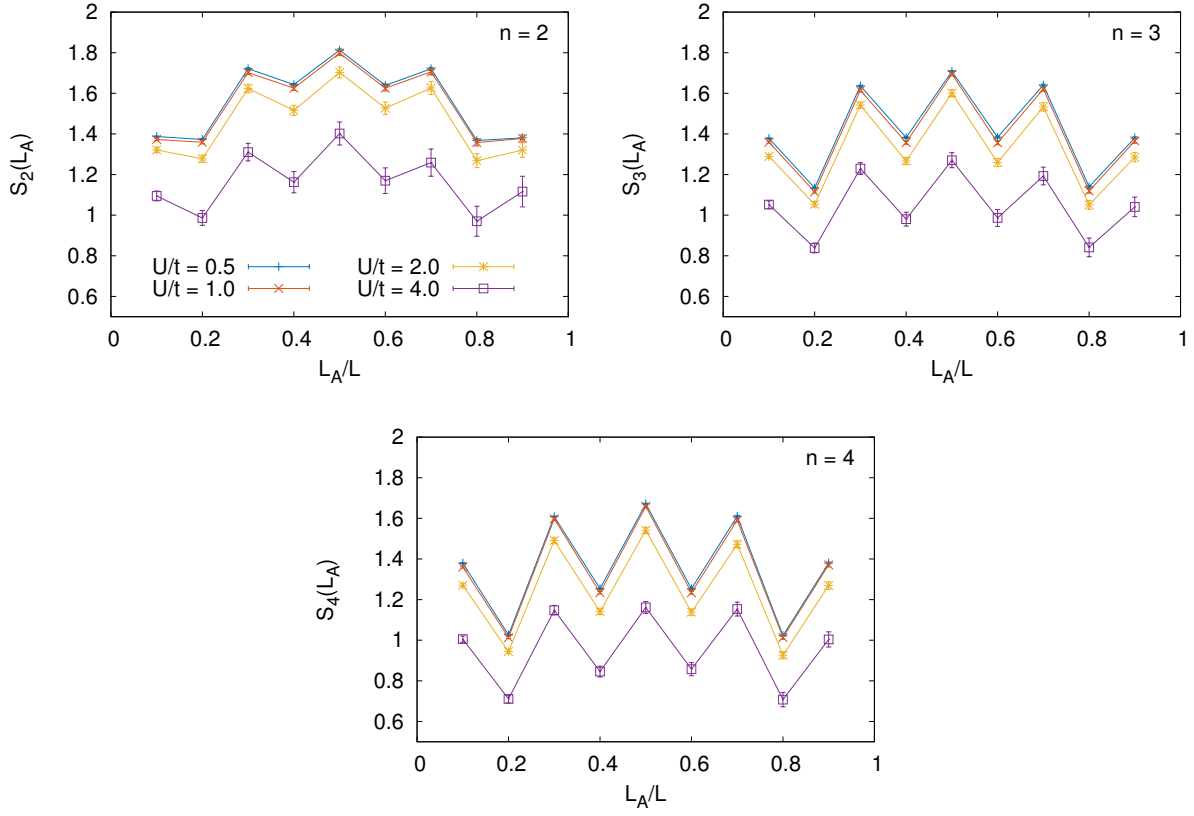
Figure 2.5: Rényi entropies S_n for $n = 2, 3, 4$ (top to bottom) of the 1D attractive Hubbard model at half filling, as a function of the subsystem size L_A/L. In each plot, results are shown for several values of the attractive coupling U/t.
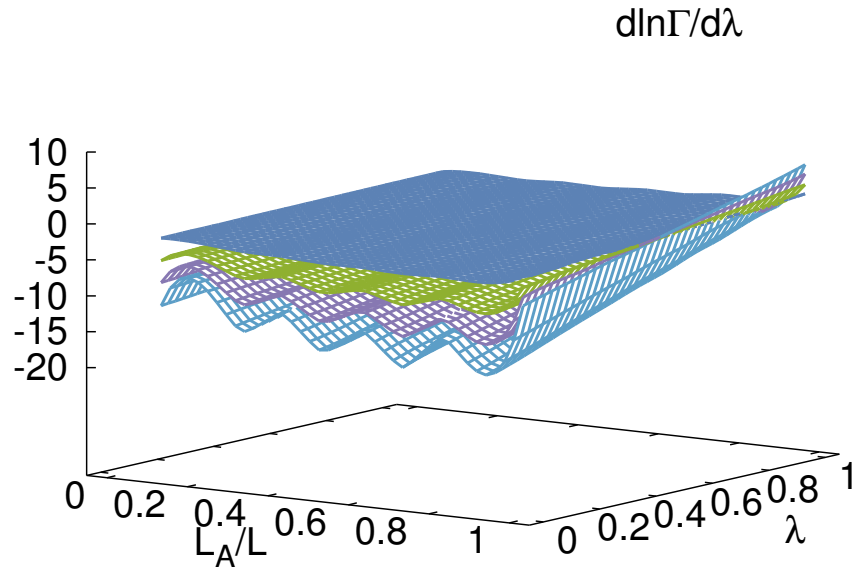
Figure 2.6: Stochastic results for $\langle \ln Q[\{\sigma\}] \rangle_\lambda$ with $n = 2, 4, 6$, and 8 (top to bottom) for a coupling of $U/t = 2.0$ as functions of the auxiliary parameter λ and the region size L_A/L.
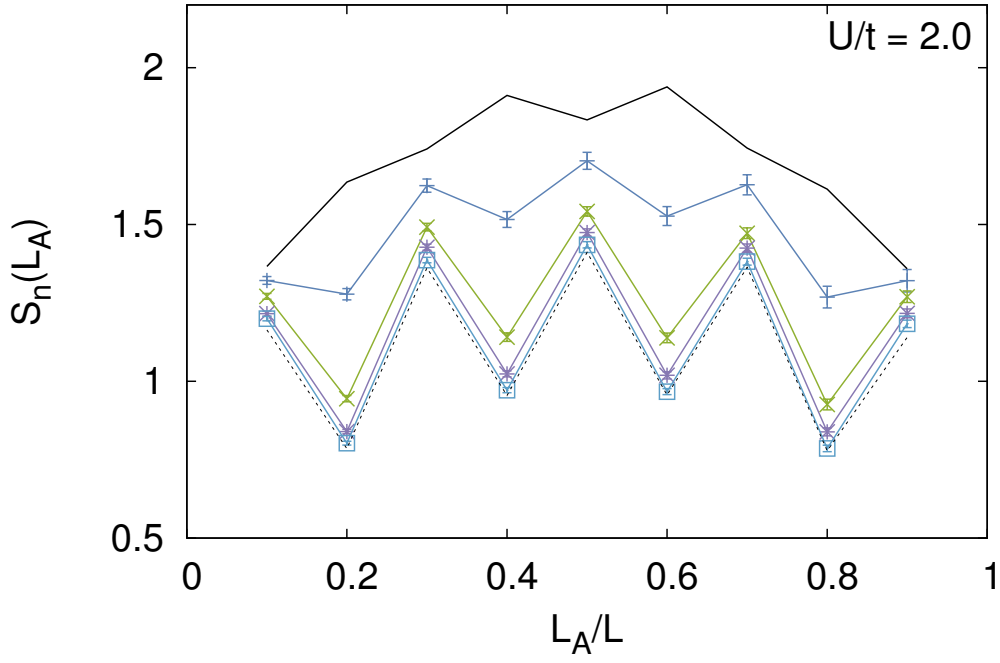
Figure 2.7: Rényi entanglement entropies S_n for orders $n = 2, 4, 6$, and 8 (top to bottom with error bars and colors matching those in Fig. 2.6) of the 1D attractive Hubbard model at half filling, as a function of the subsystem size L_A/L. The solid black line shows extrapolation to $n = 1$. The dashed black line shows extrapolation to $n \to \infty$. Again, results are shown for a coupling strength of $U/t = 2.0$.
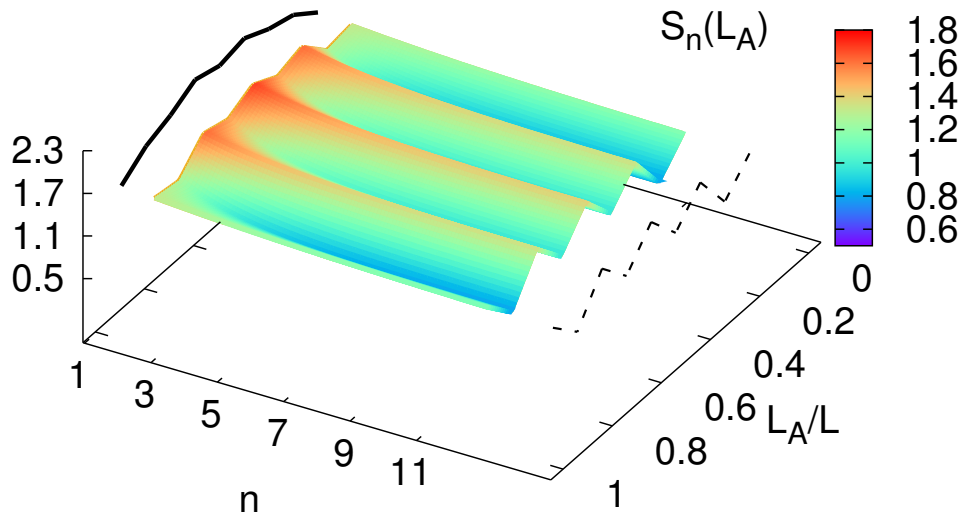
Figure 2.8: Interpolation of the Rényi entropies S_n for $n = 2, 3, 4, \ldots, 10$ for a coupling of $U/t = 2.0$ given as functions of the Rényi order n as well as the region size L_A/L. An extrapolation to $n = 1$ (the von Neumann entropy) as well as to $n \to \infty$ are shown in solid and dashed lines respectively.

CHAPTER 3:   The Entanglement Properties of the Resonant Fermi Gas

Section 3.1:   Introduction

This is an exciting time for research in the study of ultracold atoms. The degree of control that experimentalists have engineered continues to grow consistently from year to year in combination with their ability to measure and exploit collective properties in progressively more stunning ways (see e.g. [50, 51, 52]). Indeed, after the realization of Bose-Einstein condensates over twenty years ago [53, 54, 55], followed by Fermi condensates in the last decade [56], the field entered an accelerated phase and rapidly achieved control of multiple parameters such as the system's temperature, its polarization, and and even its interaction strength (e.g. in alkali gases via Feshbach resonances, see e.g. [57], and more recently in alkaline-earth gases via orbital resonances, see e.g. [58, 59]), as well as exquisite tuning of designer external trapping potentials. Additionally, numerous properties can be directly measured, ranging from the equation of state (see e.g. [60, 61]) to hydrodynamic response (see e.g. [62, 63]) and, more recently, various entanglement measures [64, 65].

This sustained progress has strengthened the intersections of ultracold atoms reseach with other areas of physics, in particular with the modern condensed matter physics and quantum information communities [66], as well as with nuclear and particle physics fields [67, 68, 69]. Quantum simulation by fine manipulation of nuclear spins, electronic states, and optical lattices, are now more realistic than ever before [70, 71, 72]. At the boundary between many of those areas lies a deceptively simple non-relativistic scale-invariant quantum system: the unitary Fermi gas, which corresponds to the limit of vanishing interaction range r_0 and infinite s-wave scattering length a, that is,

$$0 \leftarrow r_0 \ll n^{-1} \ll a \to \infty \tag{3.1}$$

where n is the system's density; this regime of parameter space corresponds to the threshold of two-body bound-state formation.

As both an actually realized resonant atomic gas and a model for dilute neutron matter, this universal spin-1/2 system has brought together the nuclear [73, 74, 75], atomic [76], and condensed matter physics areas [77, 78, 79], as well as the AdS/CFT community [80, 81], due to the underlying non-relativistic conformal invariance it displays [82]. While many properties of this quintessential many-body problem are known and in recent years have been the focus of intense study, other fundamental properties like entanglement and quantum-information aspects have thus far remained still unexplored.

Quantum information concepts are increasingly being adopted as part of the modern language of quantum many-body physics and field theory(see e.g. Refs. [7, 8, 9, 66]), in particular with regards to the characterization of quantum computation and topological phases of matter, but in connection also with black holes (see e.g. [13]) and string theory (see e.g. [18]). In the couple of decades, a large effort has been made in order to characterize the entanglement properties of low dimensional systems (especially those with spin degrees of freedom [21, 22, 83]) at quantum phase transitions (in particular those with topological order parameters that defy a local description) as well as systems of noninteracting fermions and bosons [2, 3, 4, 5, 6], which present interesting challenges of their own.

In this chapter we characterize the entanglement properties of the unitary Fermi gas using non-perturbative lattice methods. We analyze the reduced density matrix, entanglement spectrum, and associated Rényi entanglement entropies of the two-body problem by implementing an exact projection technique on the lattice and exact methods to extract spectral information from a reduced density matrix computed directly from the two-body wavefunction of the interacting system. For the many-body problem, we make use of Monte Carlo techniques developed in the previous chapters, based on the work of Ref. [1], to calculate the n-th Rényi entanglement entropy for $n = 2, 3, 4$ and 5. We showed in those chapters that our method overcomes the signal-to-noise problem of naïve Monte Carlo approaches. We did that using the one-dimensional Fermi-Hubbard model as a test case, but to our knowledge no previous calculations have been attempted for the challenging case of a three-dimensional Fermi gas, particularly a strongly interacting one.

The remainder of this chapter is organized in the following fashion: In Sec. 3.2 we offer the central definitions in preparation for Sec. 3.3, where we detail how we implement our computations of the entanglement spectrum, entanglement entropies, and other quantum-information-theoretic measures in two- and many-fermion systems. For completeness, we include in that section a discussion on how to avoid the signal-to-noise issue that plagues entanglement-entropy calculations in the many-body case with notation in accord with that used throughout this chapter, in some ways simplified and in some ways amended to match newly incorporated techniques and improvements. We extend that discussion to the case of bosons in the same section. In Sec. 3.4 we show our results for the entanglement spectrum and entropies of the two-body system along the BCS-BEC crossover, and in Sec. 3.5 we show the Rényi entanglement entropies of many fermions at unitarity. We present a summary and our main conclusions in Sec. 3.6. Finally, the appendices contain more detailed explanations of our few- and many-body methods and some brief comments on systematic effects.
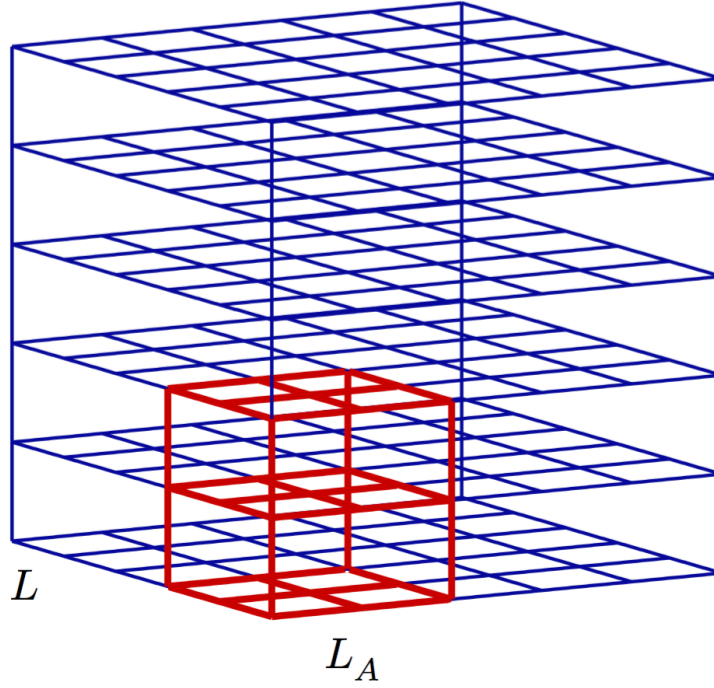
Figure 3.1: The (bipartite) entanglement entropies computed in this work correspond to partitioning the system into a subsystem A (in coordinate space, but it can also be defined in momentum space) and its complement in the total space $\bar{A}$. In practice, the calculations are carried out on systems that live in a periodic cubic lattice of side L, and the subsystems are defined by cubic subregions of side $L_A \leq L$. The reduced density matrix $\hat{\rho}_A$ of the open system A contains the information about entanglement between A and $\bar{A}$, and is obtained by tracing the full density matrix over the states supported by $\bar{A}$, which form the Hilbert space $\mathcal{H}_{\bar{A}}$.

Section 3.2:   Definitions: Hamiltonian, density matrices, and the entanglement entropy

The Hamiltonian operator governing the dynamics of resonant Fermi gases can be written as a sum

$$\hat{H} = \hat{T} + \hat{V}, \tag{3.2}$$

where the non-relativistic kinetic energy operator is

$$\hat{T} = \sum_{s=\uparrow,\downarrow} \int d^3r \; \hat{\psi}_s^\dagger(\mathbf{r}) \left(-\frac{\nabla^2}{2m}\right) \hat{\psi}_s(\mathbf{r}), \tag{3.3}$$

having defined $\hat{\psi}_s^\dagger(\mathbf{r})$ and $\hat{\psi}_s(\mathbf{r})$ are the creation and annihilation operators of particles of spin species $s =\uparrow,\downarrow$ at location $\mathbf{r}$.

The two-body, zero-range (contact) interaction operator is given by

$$\hat{V} = -g \int d^3r \; \hat{\psi}_\uparrow^\dagger(\mathbf{r})\hat{\psi}_\uparrow(\mathbf{r})\hat{\psi}_\downarrow^\dagger(\mathbf{r})\hat{\psi}_\downarrow(\mathbf{r}), \tag{3.4}$$

where the bare coupling g is tuned to the desired physical situation. By definition, the limit of unitarity is achieved by requiring that the ground state of the two-body problem lies at the threshold of bound-state formation (note that in one and two dimensions bound states form at arbitrarily small attractive coupling, but a finite value is required in three dimensions). Because our work was carried out in a finite volume with periodic boundary conditions, we used Lüscher's formalism [84, 85] to renormalize, that is, to relate the bare coupling to the scattering length in the analysis of the BCS-BEC crossover. We describe that procedure below, when showing the results for the two-body problem.

The full, normalized density matrix of the system is

$$\hat{\rho} = \frac{e^{-\beta\hat{H}}}{\mathcal{Q}}, \tag{3.5}$$

where

$$\mathcal{Q} = \text{Tr}_{\mathcal{H}}\left[e^{-\beta\hat{H}}\right], \tag{3.6}$$

is the canonical partition function, as is typical, and $\mathcal{H}$ is the full Hilbert space. In this chapter, we are concerned with systems in a pure state, namely the ground state $|\Xi\rangle$, such that the full density matrix can be written as

$$\hat{\rho} = |\Xi\rangle\langle\Xi|. \tag{3.7}$$

In both the few- and many-body systems we consider here, the zero-temperature density matrix will be approached by a projection method we describe below.

A subsystem A and its complement $\bar{A}$ (in coordinate or momentum space, see Fig. 3.1) support states that belong to Hilbert spaces $\mathcal{H}_A$ and $\mathcal{H}_{\bar{A}}$, respectively, so that the Hilbert space $\mathcal{H}$ of the full system (in the absence of link degrees of freedom) can be written as a direct product space

$$\mathcal{H} = \mathcal{H}_A \otimes \mathcal{H}_{\bar{A}}. \tag{3.8}$$

The density matrix $\hat{\rho}_A$ of subsystem A, usually referred to as the reduced density matrix, is defined by tracing over the degrees of freedom supported by $\bar{A}$, i.e. tracing out the states in $\mathcal{H}_{\bar{A}}$ in order to yield an

operator on only the remaining Hilbert space:

$$\hat{\rho}_A = \mathrm{Tr}_{\mathcal{H}_{\bar{A}}}\hat{\rho}. \tag{3.9}$$

From this definition, the characteristics of A as an open subsystem can be computed and formally investigated using operators with support in A. Specifically, quantitative measures of entanglement between A and $\bar{A}$ are given by the well-known von Neumann entanglement entropy,

$$S_{\mathrm{vN},A} = -\mathrm{Tr}_{\mathcal{H}_A}\left[\hat{\rho}_A \ln \hat{\rho}_A\right], \tag{3.10}$$

and by the n-th order Rényi entanglement entropy,

$$S_{n,A} = \frac{1}{1-n}\ln \mathrm{Tr}_{\mathcal{H}_A}\left[\hat{\rho}_A^n\right]. \tag{3.11}$$

Naturally, these entropies vanish when A is the whole system, as then there is full knowledge of the state of the system. In any other case, the entanglement entropy will be non-zero, unless the ground state factorizes into a state supported in A and a state supported in the complement $\bar{A}$. As the entanglement between A and $\bar{A}$ happens across the boundary that separates those regions, it is quite intuitive to expect $S_{n,A}$ to scale extensively with the size of that intermediate boundary, i.e. proportional to the area delimiting A. This point was the topic of many papers in the last decade or so, especially in connection with quantum phase transitions and the scaling of entanglement measure near those quantum critical points (see e.g. [86]).

However, in recent years, it was shown rigorously that the Rényi entanglement entropy of non-interacting fermions with a well-defined Fermi surface presents a multiplicative logarithmic violation of this assumed area law [2, 3, 4, 5, 6]. This peculiarity was verified numerically with the aid of overlap-matrix techniques [87], which we reproduce in Fig. 3.2, where we explicitly depict said logarithmic dependence (dashed line) as a function of $x = k_F L_A$, where k_F is the Fermi momentum (roughly the inverse inter-particle separation up to a pure number) and L_A is the linear size of the subregion A, such that

$$
\begin{aligned}
x = k_F L_A &= \frac{\pi N}{2}\frac{L_A}{L} && \text{in 1D,} & (3.12)\\
&= (2\pi N)^{1/2}\frac{L_A}{L} && \text{in 2D,} & (3.13)\\
&= (3\pi^2 N)^{1/3}\frac{L_A}{L} && \text{in 3D,} & (3.14)
\end{aligned}
$$

where N is the total particle number. We note that, at large enough x, finite size effects eventually emerge

and force the entropy quickly to zero. The sub-leading oscillations were studied in detail in Ref. [88].

Resonant fermions are strongly coupled, as the regime is non-perturbative and away from any regime with small dimensionless parameters; nevertheless, we can expect $S_{n,A}$ to follow a similar trend as the non-interacting analogue, for the following reasons. First, resonant fermions have a distinguishable Fermi surface (note, however, that that is quickly lost as one proceeds towards the BEC side of the resonance), whose role in the entanglement entropy has been emphasized many times (see e.g. [46]). Second, our experience with $S_{n,A}$ for the Hubbard model in other cases indicates that very strong couplings U/t are needed even in a single spatial dimension (where quantum fluctuations are qualitatively much more discernible than in three or more dimensions) in order for $S_{n,A}$ to differ noticeably from the free result. We anticipate, therefore, similar behavior for resonant fermions as that of the bottom panel of Fig. 3.2; the latter provides some qualitative knowledge of where the leading logarithmic and sub-leading dependence sets in for $S_{n,A}$ as a function of $x = k_F L_A$. In fact, as we will see below, the onset of this asymptotic behavior (meaning dominated by leading and sub-leading dependence on x) at $x \simeq 2 - 4$ is the same for unitarity as for the non-interacting case. This similarity is stunning, as there is no obvious reason for that to be the case: had this onset appeared at $x \simeq 10$ or greater as could very well have been the case, the calculations in this chapter would not have been possible, as they would have required enormous lattices. Below, we return to this discussion when presenting our many-body results.

Section 3.3:   Method

In this section we detail the two approaches utilized in this chapter. We first address the unpolarized two-particle problem, which we solved with a direct (that is, non-stochastic) projection technique on the lattice. This problem can be solved exactly by changing to center-of-mass and relative coordinates; nevertheless, doing so implies using a method that works only in that particular case, and we are greatly interested in algorithms that may be used in a variety of situations (e.g. in the presence of external fields, more than two particles, time-dependent cases, and so forth). We address thereafter the many-body problem using a method detailed in the previous chapter, which we first presented and tested for one-dimensional systems.

Even though both methods we detail in this chapter utilize an auxiliary field transformation, the ultimate utility of this technique is markedly different in each case. Below, we describe the part of the formalism common to both approaches before treating in later sections the details of their deviation from common notation and assumptions.

At a fixed chemical potential μ and specified inverse temperature β, the usual grand canonical partition

function $\mathcal{Z}$ is defined as a trace over the usual Boltzmann weight via

$$\mathcal{Z} = \text{Tr}\left[e^{-\beta(\hat{H}-\mu\hat{N})}\right] \tag{3.15}$$

for Hamiltonian operator $\hat{H}$ and total particle-number operator $\hat{N}$. Rewriting the inverse temperature as an integer number N_τ of steps, we make use of a symmetric Suzuki-Trotter decomposition with the ultimate aim of factoring each operator into distinct one-body and two-body pieces. For the grand canonical Boltzmann factor, we obtain

$$e^{-\beta(\hat{H}-\mu\hat{N})} = \prod_{j=1}^{N_\tau} e^{-\tau\hat{K}/2}e^{-\tau\hat{V}}e^{-\tau\hat{K}/2} + \mathcal{O}(\tau^2) \tag{3.16}$$

were we have defined the modified kinetic energy operator as

$$\hat{K} = \hat{T} - \mu\hat{N}. \tag{3.17}$$

At each spatial position $\mathbf{r}$ and for each of the equivalent N_τ factors, we decompose the interaction via the introduction of a Hubbard-Stratonovich auxiliary field σ which we choose to be of a continuous and compact form [32]. More concretely for each spacetime position $(\mathbf{r}, \tau_j)$, where $\mathbf{r} \in [0, L)^3$ and $\tau_j = j\tau$ for some $1 \leq j \leq N_\tau$, we introduce

$$e^{\tau g \hat{n}_\uparrow \hat{n}_\downarrow} = \int_{-\pi}^{\pi} \frac{d\sigma}{2\pi}\left(1 + B\,\hat{n}_\uparrow \sin\sigma\right)\left(1 + B\,\hat{n}_\downarrow \sin\sigma\right) \tag{3.18}$$

having suppressed the spacetime dependence of the field σ and the spatial dependence of the fermionic density operators $\hat{n}_s(\mathbf{r}) = \hat{\psi}_s^\dagger(\mathbf{r})\hat{\psi}_s(\mathbf{r})$ where $s = \uparrow, \downarrow$ indicates the fermion species. Because $\hat{n}_s(\mathbf{r})$ is an idempotent operator, it follows that

$$e^{\tau g \hat{n}_\uparrow \hat{n}_\downarrow} = 1 + (e^{\tau g} - 1)\hat{n}_\uparrow \hat{n}_\downarrow, \tag{3.19}$$

which implies that the constant B satisfies the following equation:

$$e^{\tau g} - 1 = \frac{B^2}{2}. \tag{3.20}$$

Gathering together the individual integration measures, we arrive at a path-integral form of the partition

function which is accurate to quadratic order in the temporal lattice spacing, writing

$$\mathcal{Z} = \int \mathcal{D}\sigma \, \mathrm{Tr} \, \hat{\mathcal{U}}[\sigma] + \mathcal{O}(\tau^2) \tag{3.21}$$

where

$$\hat{\mathcal{U}}[\sigma] = \prod_{j=1}^{N_\tau} \hat{\mathcal{U}}_j[\sigma], \tag{3.22}$$

and the individual factors are given by

$$\hat{\mathcal{U}}_j[\sigma] = e^{-\tau \hat{K}/2} \prod_{\mathbf{r}} \Big[\big(1 + B \, \hat{n}_\uparrow(\mathbf{r}) \sin \sigma(\mathbf{r}, \tau_j)\big) \big(1 + B \, \hat{n}_\downarrow(\mathbf{r}) \sin \sigma(\mathbf{r}, \tau_j)\big) \Big] e^{-\tau \hat{K}/2}. \tag{3.23}$$

Ultimately, the temporal discretization τ will be chosen so that any artifacts of this approximation will be of less importance than the residual statistical uncertainties, and for this reason, for all intents and purposes, we may neglect the terms of quadratic order in τ.

As the kinetic energy operator $\hat{T}$ and the number operator $\hat{N}$ are already written as products of species-specific operators, we may partition the operator $\hat{\mathcal{U}}$ into individual factors each of which assumes responsibility for the evolution of a particular fermion species $s = \uparrow, \downarrow$. We make this separation by defining the operators $\hat{T}_s$, $\hat{N}_s$, and $\hat{K}_s$ for $s = \uparrow, \downarrow$ by

$$\hat{T}_s = \int d^3r \, \hat{\psi}_s^\dagger(\mathbf{r}) \left(-\frac{\nabla^2}{2m} \right) \hat{\psi}_s(\mathbf{r}), \tag{3.24}$$

$$\hat{N}_s = \int d^3r \, \hat{\psi}_s^\dagger(\mathbf{r}) \hat{\psi}_s(\mathbf{r}), \tag{3.25}$$

and $\hat{K}_s = \hat{T}_s - \mu \hat{N}_s$. We then write

$$\hat{\mathcal{U}}_{j,s}[\sigma] = e^{-\tau \hat{K}_s/2} \prod_{\mathbf{r}} \big(1 + B \, \hat{n}_s(\mathbf{r}) \sin \sigma(\mathbf{r}, \tau_j)\big) e^{-\tau \hat{K}_s/2},$$

such that

$$\hat{\mathcal{U}}[\sigma] = \hat{\mathcal{U}}_\uparrow[\sigma] \, \hat{\mathcal{U}}_\downarrow[\sigma], \tag{3.26}$$

where

$$\hat{\mathcal{U}}_s[\sigma] = \prod_{j=1}^{N_\tau} \hat{\mathcal{U}}_{j,s}[\sigma]. \tag{3.27}$$

49

The exponential form of each factor in the above provides (see e.g. [34])

$$\mathcal{Z} = \int \mathcal{D}\sigma \, \det\left(1 + \boldsymbol{U}_\uparrow[\sigma]\right) \det\left(1 + \boldsymbol{U}_\downarrow[\sigma]\right) \tag{3.28}$$

after performing the required Fock-space trace, where we have suppressed higher-order contributions in τ (which are of order τ^2), and written the matrix $\boldsymbol{U}_s[\sigma]$ for the restriction of each of the operators $\hat{\mathcal{U}}_s[\sigma]$ to the single-particle Hilbert space. Knowing that we are confined to that space, it follows that each of those matrices contains an overall factor of the fugacity

$$z \equiv e^{\beta\mu}. \tag{3.29}$$

We exhibit this factor explicitly in what follows and redefine the matrices $\boldsymbol{U}_s[\sigma]$ to reflect this minor revision. In this chapter, we exclusively treat balanced (that is, unpolarized) systems, and so we may treat the determinants as equivalent in derivations that follow by writing

$$\mathcal{Z} = \int \mathcal{D}\sigma \, \det^2(1 + z\,\boldsymbol{U}[\sigma]), \tag{3.30}$$

and by neglecting to denote any spin degree of freedom wherever context precludes confusion.

3.3.1: Direct lattice approach to the entanglement spectrum of the two-body problem

Identifying the transfer matrix

In order to give full account of the details as well as showcase the generality of our technique, we show the main steps here in broad strokes and leave the finer details to be covered in Appendix .1.

We first isolate the two-body sector using the above path-integral form of the partition function $\mathcal{Z}$. From the finite-temperature partition function Eq. (3.28), we may derive the conventional virial expansion in powers of the fugacity for each spin, which is given by

$$\mathcal{Z} = \sum_{N_\uparrow, N_\downarrow = 0}^{\infty} z_\uparrow^{N_\uparrow} z_\downarrow^{N_\downarrow} \mathcal{Q}_{N_\uparrow, N_\downarrow}, \tag{3.31}$$

where we have identified the coefficient of the N_s-th power of the fugacity as the N_s-particle canonical partition function $\mathcal{Q}_{N_\uparrow, N_\downarrow}$. This realization offers a convenient way of identifying the fixed particle-number subspaces and singling them out in the full partition function.

Expanding the path-integral expression for the grand canonical partition function, we find that in terms

of the matrix $U[\sigma]$, the $(1+1)$-particle partition function is

$$\mathcal{Q}_{1,1} = \int \mathcal{D}\sigma \operatorname{tr}^2 U[\sigma]. \tag{3.32}$$

The path integral in $\mathcal{Q}_{1,1}$ above can be evaluated directly in a way that elucidates the form of the two-body transfer matrix. To that end, and in order to provide a more general derivation, we define a four-index object from which the above squared trace may be obtained by suitable index contraction:

$$R_{ab,cd} = \int \mathcal{D}\sigma \, U[\sigma]_{ac} \, U[\sigma]_{bd}. \tag{3.33}$$

The same four-index object, with indices properly contracted to account for antisymmetry, can be used to analyze the $(2+0)$-particle case.

We next explicitly write out each of the matrices $U[\sigma]$ in its product form; that is, we reintroduce Eq. (3.22) in matrix form:

$$U[\sigma] = \prod_{j=1}^{N_\tau} U_j[\sigma]. \tag{3.34}$$

Exactly N factors of the matrix $U[\sigma]$ appear for each contribution to the N-body transfer matrix, and as a result each temporal lattice point appears in the integrand exactly N times. Turning now to the individual factors, we write each of the matrices $U_j[\sigma]$ in such a way as to exhibit the factor responsible for the interaction. More specifically, we write

$$U_j[\sigma] = T V_j[\sigma] T, \tag{3.35}$$

where the matrix elements

$$[T]_{\mathbf{kk'}} = e^{-\tau k^2/2} \delta_{\mathbf{k},\mathbf{k'}}, \tag{3.36}$$

comprise the single-particle form of the kinetic energy operator defined above (in momentum space), and the (position-space representation of the) auxiliary external potential operator has matrix elements

$$\left[V_j[\sigma]\right]_{\mathbf{rr'}} = \left(1 + B \sin \sigma(\mathbf{r}, \tau_j)\right) \delta_{\mathbf{rr'}}. \tag{3.37}$$

At this point, all matrix elements have been written out and can be commuted as needed to carry out the path integral. The only nontrivial results are obtained when an even number (in this $N = 2$ case no more than 2) of fields $\sigma(\mathbf{r}, \tau_j)$ appear in the integrand for the same values of $(\mathbf{r}, \tau_j)$.

This unraveling of the auxiliary-field transformation may seem a convoluted or cumbersome way to proceed, but it is useful in that it mechanically generates the correct expression for the N-body partition

51

function for arbitrary particle content simply by rote differentiation of the fermion determinants. Moreover, this calculation is accomplished without the need to deal with tedious operator algebra, and it is easily generalized to bosons. In the two-body case, in particular, the above procedure results in

$$R_{ac,bd} = \left[M_2^{N_\tau} \right]_{ac,bd},\tag{3.38}$$

where we have naturally identified a transfer matrix in the two-particle subspace

$$[M_2]_{ac,bd} = \mathcal{K}_{ab}\mathcal{K}_{cd} + (e^{\tau g} - 1)\mathcal{I}_{abcd},\tag{3.39}$$

and where

$$\mathcal{K}_{ij} = \sum_p \boldsymbol{T}_{ip}\boldsymbol{T}_{pj},\tag{3.40}$$

$$\mathcal{I}_{ijkl} = \sum_p \boldsymbol{T}_{ip}\boldsymbol{T}_{pj}\boldsymbol{T}_{kp}\boldsymbol{T}_{pl}.\tag{3.41}$$

The form of the transfer matrix lends itself immediately to an intuitive and useful diagrammatic representation, which we show for the two- and three-particle cases (the latter is derived in Appendix .1) in Eqs. (3.42), (3.43) and (3.44).

$$[M_2]_{ac,bd} = \quad \text{(diagram)} \quad + \quad (e^{\tau g} - 1) \quad \text{(diagram)}\tag{3.42}$$

$$[M_3]_{abc,def} = \quad \text{(diagram)} \quad + \quad (e^{\tau g} - 1) \quad \text{(diagram)}\tag{3.43}$$

$$\text{(diagram)} = \text{(diagram)} + \text{(diagram)} + \text{(diagram)}\tag{3.44}$$

Obtaining the ground state and the reduced density matrix

Having extracted the transfer matrix allows us to now design a projection method to extract the ground state by repeated application of M_2. Proposing a guess state $|\Xi_0\rangle$, we project out the true two-particle ground state $|\Xi\rangle$ via

$$M_2^{N_\tau} |\Xi_0\rangle \xrightarrow{N_\tau \to \infty} |\Xi\rangle. \tag{3.45}$$

In practice, we compute the position-space wavefunction $\xi(x_\uparrow, x_\downarrow) = \langle x_\uparrow, x_\downarrow | \Xi \rangle$. Wavefunction in hand, we calculate the matrix elements of the full density matrix $\hat{\rho}$ as

$$\langle x_\uparrow, x_\downarrow | \hat{\rho} | x'_\uparrow, x'_\downarrow \rangle = \langle x_\uparrow, x_\downarrow | \Xi \rangle \langle \Xi | x'_\uparrow, x'_\downarrow \rangle \tag{3.46}$$

$$= \xi^*(x'_\uparrow, x'_\downarrow) \, \xi(x_\uparrow, x_\downarrow). \tag{3.47}$$

From these matrix elements, the matrix elements of the reduced density matrix $\hat{\rho}_A$ can be obtained as well by performing a partial trace. Given two states $|s\rangle, |s'\rangle \in \mathcal{H}_A$ for the subregion A, each state being completely specified by selecting for each degree of freedom either a position in A or in the complement $\bar{A}$, we compute the matrix element via

$$\langle s | \hat{\rho}_A | s' \rangle = \sum_{a \in \mathcal{A}_{ss'}} (|s\rangle \otimes |a\rangle)^\dagger \, \hat{\rho} \, (|s'\rangle \otimes |a\rangle), \tag{3.48}$$

where, at each fixed pair of two-particle states s, s', the sum is taken over all states $|a\rangle \in \mathcal{H}_{\bar{A}}$ such that the state $|s\rangle \otimes |a\rangle \in \mathcal{H}_A \otimes \mathcal{H}_{\bar{A}}$ (resp. $|s'\rangle \otimes |a\rangle \in \mathcal{H}_A \otimes \mathcal{H}_{\bar{A}}$) is consistent with the first (resp. second) index of the matrix element being evaluated. We have denoted this set as $\mathcal{A}_{ss'}$. From this matrix, we compute the entanglement spectrum $\sigma(\hat{H}_A)$, that is the spectrum of the entanglement Hamiltonian defined

$$\hat{\rho}_A = e^{-\hat{H}_A}, \tag{3.49}$$

as well as the von Neumann and Rényi entanglement entropies.

3.3.2: Lattice Monte Carlo approach to the many-body problem

We implement the Monte Carlo version of the algorithm outlined above in order to address the many-body system. The output of this computation is not the ground-state wavefunction, however, but rather

the expectation value of the desired observable in a projected state. In this case, the observable is of course the entanglement entropy. To obtain it, crucial intermediate steps are required that go beyond conventional Monte Carlo approaches and that were detailed above in previous chapters. We outline the basic formalism again in order to develop a notation consistent with the narrative of the present chapter, and we then proceed to explain the additional steps required to calculate $S_{n,A}$.

Basic formalism

Starting off with a largely arbitrary many-body state $|\Omega_0\rangle$, we evolve the state forward in imaginary time by an amount β by constructing

$$|\Omega(\beta)\rangle = e^{-\beta \hat{H}}|\Omega_0\rangle, \tag{3.50}$$

In the limit of large imaginary time, we may write

$$|\Omega(\beta)\rangle \xrightarrow{\beta \to \infty} |\Omega\rangle, \tag{3.51}$$

where $|\Omega\rangle$ is the true interacting ground state provided that $\langle \Omega_0 | \Omega \rangle \neq 0$.

We may compute the ground-state expectation value for an operator $\hat{O}$ by studying the large-imaginary-time behavior of the function

$$O(\beta) = \frac{1}{Z(\beta)} \langle \Omega(\beta/2)| \hat{O} |\Omega(\beta/2)\rangle, \tag{3.52}$$

with the zero-temperature normalization (generating functional) defined as

$$Z(\beta) = \langle \Omega(\beta/2)|\Omega(\beta/2)\rangle = \langle \Omega_0| e^{-\beta \hat{H}} |\Omega_0\rangle. \tag{3.53}$$

As derived earlier in detail, we implement a symmetric factorization of the Boltzmann weight [c.f. Eq. (3.16)] in order to separate factors depending only on the one-body kinetic-energy operator from the significantly more involved two-body interaction-energy operator responsible for the contact interaction between the particles. After this decomposition, we again make use of an auxiliary field transformation [c.f. Eq. (3.18)] to recast the interaction factor as an expectation value. This identity allows us to write the ground- state estimator of Eq. (3.52) defined above in path integral form as

$$O(\beta) = \frac{1}{Z(\beta)} \int \mathcal{D}\sigma \, P_\beta[\sigma] \, O_\beta[\sigma], \tag{3.54}$$

while simultaneously proving that

$$Z(\beta) = \int \mathcal{D}\sigma \, P_\beta[\sigma], \tag{3.55}$$

again to quadratic order in the imaginary time discretization parameter τ.

We have identified a naturally emerging probability measure $P_\beta[\sigma]$ calculated as

$$P_\beta[\sigma] = \langle \Omega_0 | \hat{\mathcal{U}}_\beta[\sigma] | \Omega_0 \rangle, \tag{3.56}$$

with the operator $\hat{\mathcal{U}}_\beta[\sigma]$ defined as before in Eq. (3.22) (setting $\mu = 0$ in the kinetic energy factor since particle number is fixed in the zero-temperature formalism). The integrand then is of the form

$$O_\beta[\sigma] = \frac{\langle \Omega_0 | \hat{\mathcal{U}}_{\beta/2}[\sigma] \, \hat{O} \, \hat{\mathcal{U}}_{\beta/2}[\sigma] | \Omega_0 \rangle}{\langle \Omega_0 | \hat{\mathcal{U}}_\beta[\sigma] | \Omega_0 \rangle}. \tag{3.57}$$

Taking advantage of the arbitrariness of the initial state, we choose for $|\Omega_0\rangle$ to be a Slater determinant for each fermion species constructed from single-particle non-interacting plane-wave states ϕ_j for $1 \leq j \leq N/2$ with $N/2 = N_\downarrow = N_\uparrow$. With this simple assumption, we see that the probability takes the form

$$P_\beta[\sigma] = \det^2 \boldsymbol{U}_\beta[\sigma], \tag{3.58}$$

with

$$[\boldsymbol{U}_\beta[\sigma]]_{kk'} = \langle \phi_k | \hat{\mathcal{U}}_\beta[\sigma] | \phi_{k'} \rangle, \tag{3.59}$$

where the indices k, k' satisfy $1 \leq k, k' \leq N/2$.

Path integral form of the reduced density matrix, replica fields, and the Rényi entropy

Originally, it was demonstrated by Tarun Grover in Ref. [1] that the interacting reduced density matrix can be rewritten in terms of the fermionic creation and annihilation operators $\hat{c}^\dagger, \hat{c}$ as a weighted average with respect to the probability measure $P_\beta[\sigma]$ derived above and a collection of non-interacting density matrices corresponding to fermions in a background field. More specifically,

$$\hat{\rho}_{A,\beta} = \int \mathcal{D}\sigma \, P_\beta[\sigma] \, \hat{\rho}_{A,\beta}[\sigma], \tag{3.60}$$

where

$$\hat{\rho}_{A,\beta}[\sigma] = \det\left(1 - G_{A,\beta}[\sigma]\right) \exp\left(-\sum_{i,j \in A} \hat{c}_i^\dagger \left[\log\left(G_{A,\beta}^{-1}[\sigma] - 1\right)\right]_{ij} \hat{c}_j\right). \tag{3.61}$$

Note that $\hat{\rho}_{A,\beta}[\sigma]$ is the aforementioned reduced density matrix of a system of non-interacting fermions in the external field σ. Analytic expressions for free reduced density matrices were first put forward in Refs. [43, 44, 45], but it was not until more recent work in Ref. [1] that those were folded into the non-perturbative formalism based around Eq. (3.60) and made amenable to Monte Carlo calculations.

In the above equation, $G_{A,\beta}[\sigma]$ is the spatial restriction of the (equal-time) one-body density matrix for either of the two flavors to the region A computed as

$$G_{A,\beta}[\sigma]_{rr'} = \sum_{a,b=1}^{N/2} [\boldsymbol{U}_\beta^{-1}[\sigma]]_{ab} \, \phi_b^*(r, \beta/2) \, \phi_a(r', \beta/2), \tag{3.62}$$

where

$$\phi_a(r', \beta/2) = \langle r' | \hat{\mathcal{U}}_\beta[\sigma] | \phi_a \rangle \tag{3.63}$$

$$\phi_b^*(r, \beta/2) = \langle \phi_b | \hat{\mathcal{U}}_\beta[\sigma] | r \rangle. \tag{3.64}$$

We neglect to explicitly show the imaginary-time β dependence in much of what follows with the understanding that calculations are to be performed in the limit of $\beta \to \infty$. Practically, this prescription implies performing multiple simulations for various values of the imaginary time and extrapolating thereafter.

An estimator for the n-th order Rényi entropy can be derived from this decomposed form of the reduced density matrix. Because n factors of $\hat{\rho}_A$ are required, an equal number of auxiliary fields will appear, the so-called "replica" fields, which we will abbreviate collectively as $\boldsymbol{\sigma}$.

The final form (see Refs. [1, 30, 31]) is

$$\exp\left((1-n)S_{n,A}\right) = \mathrm{Tr}_{\mathcal{H}_A}\left[\rho_A^n\right] = \frac{1}{Z^n} \int \mathcal{D}\Sigma \, P[\boldsymbol{\sigma}] \, Q[\boldsymbol{\sigma}], \tag{3.65}$$

where (again, note the suppressed β dependence)

$$P[\boldsymbol{\sigma}] = P[\sigma_1]P[\sigma_2]\dots P[\sigma_n], \tag{3.66}$$

with the naturally appearing observable being

$$Q[\boldsymbol{\sigma}] = \det^2 W[\boldsymbol{\sigma}], \tag{3.67}$$

with

$$W[\boldsymbol{\sigma}] = \prod_{j=1}^{n}(1 - G_A[\sigma_j])\left[1 + \prod_{k=1}^{n}\frac{G_A[\sigma_k]}{1 - G_A[\sigma_k]}\right].\tag{3.68}$$

We have adopted a notation such that, for functionals or integrals of functionals of multiple auxiliary fields, we write

$$F[\boldsymbol{\sigma}] = F[\sigma_1, \sigma_2, \ldots, \sigma_n],\tag{3.69}$$

and

$$\int \mathcal{D}\Sigma\, F[\boldsymbol{\sigma}] = \int \mathcal{D}\sigma_1 \mathcal{D}\sigma_2 \ldots \mathcal{D}\sigma_n\, F[\boldsymbol{\sigma}],\tag{3.70}$$

respectively.

Equation (3.68) emphasizes that it seems necessary to confront the challenging task of inverting $1 - G_A$, which can be very nearly singular, as pointed out in Ref. [1] and in previous chapters. For $n=2$, no inversion is required, because the equations simplify such that

$$Q[\boldsymbol{\sigma}] = \det^2\left[(1 - G_A[\sigma_1])(1 - G_A[\sigma_2]) + G_A[\sigma_1]G_A[\sigma_2]\right].\tag{3.71}$$

Nevertheless, for higher n there is no such simplification, and therefore it is less clear how one may avoid the problem if it may be avoided at all. We solved this problem in the previous chapter (see also [25, 28, 29, 27]); the main point is realizing that

$$\det W[\boldsymbol{\sigma}] = \det L[\boldsymbol{\sigma}]\ \det K[\boldsymbol{\sigma}],\tag{3.72}$$

where $L[\boldsymbol{\sigma}]$ is a block diagonal matrix (one block per replica k):

$$L[\boldsymbol{\sigma}] \equiv \mathrm{diag}\left[1 - G_A[\sigma_k]\right],\tag{3.73}$$

and

$$K[\boldsymbol{\sigma}] \equiv \begin{pmatrix} 1 & 0 & 0 & \ldots & 0 & -R[\sigma_n] \\ R[\sigma_1] & 1 & 0 & \ldots & \vdots & 0 \\ 0 & R[\sigma_2] & 1 & 0 & 0 & 0 \\ \vdots & \ddots & \ddots & \ddots & 1 & \vdots \\ 0 & \ldots & \ldots & 0 & R[\sigma_{n-1}] & 1 \end{pmatrix},\tag{3.74}$$

where

$$R[\sigma_k] = \frac{G_A[\sigma_k]}{G_A[\sigma_k] - 1}.\tag{3.75}$$

Within the determinant of Eq. (3.72), we multiply $K[\boldsymbol{\sigma}]$ and $L[\boldsymbol{\sigma}]$ and define

$$T[\boldsymbol{\sigma}] \equiv K[\boldsymbol{\sigma}]L[\boldsymbol{\sigma}] = 1 - D\,\mathcal{G}[\boldsymbol{\sigma}], \tag{3.76}$$

where $\mathcal{G}[\boldsymbol{\sigma}]$ is a block diagonal matrix defined by

$$\mathcal{G}[\boldsymbol{\sigma}] = \mathrm{diag}\left[G_A[\sigma_k]\right], \tag{3.77}$$

and

$$D \equiv \begin{pmatrix} 1 & 0 & 0 & \ldots & -1 \\ 1 & 1 & 0 & \ldots & 0 \\ 0 & 1 & 1 & \ldots & 0 \\ \vdots & \ddots & \ddots & \ddots & \vdots \\ 0 & \ldots & 0 & 1 & 1 \end{pmatrix}. \tag{3.78}$$

Equation (3.81) is the result that allows us to bypass the inversion of $1 - G_A$. The form of $T[\boldsymbol{\sigma}]$ is clearly much simpler than that of the original estimator $W[\boldsymbol{\sigma}]$. For these reasons we use $T[\boldsymbol{\sigma}]$ in all of the many-body MC calculations presented here. Our improved formulation allowed us to study Rényi entropies as high as $n = 5$; higher are also possible, but as we will see later and as seen in previous chapters, progressively higher Rényi orders converge surprisingly quickly toward the large-n bound.

For completeness, we present here the simplification for the bosonic case as well (and add a subindex B accordingly), for which

$$Q_B[\boldsymbol{\sigma}] = \mathrm{det}^{-2}W_B[\boldsymbol{\sigma}], \tag{3.79}$$

and

$$W_B[\boldsymbol{\sigma}] = \prod_{j=1}^{n}(1 + G_A[\sigma_j]) \left[1 - \prod_{k=1}^{n}\frac{G_A[\sigma_k]}{1 + G_A[\sigma_k]}\right]. \tag{3.80}$$

The analogous strategy to avoid inversion leads here to

$$T_B[\boldsymbol{\sigma}] \equiv 1 - D_B\mathcal{G}[\boldsymbol{\sigma}], \tag{3.81}$$

where $\mathcal{G}[\boldsymbol{\sigma}]$ is a block diagonal matrix defined by

$$\mathcal{G}[\boldsymbol{\sigma}] = \mathrm{diag}\left[G_A[\sigma_n]\right], \tag{3.82}$$

and

$$D_B \equiv \begin{pmatrix} -1 & 0 & 0 & \dots & 1 \\ 1 & -1 & 0 & \dots & 0 \\ 0 & 1 & -1 & \dots & 0 \\ \vdots & \ddots & \ddots & \ddots & \vdots \\ 0 & \dots & 0 & 1 & -1 \end{pmatrix}. \tag{3.83}$$

Signal-to-noise issues and how to overcome them

The path integral form of the Rényi entropy Eq. (3.65) has a deceptively simple form, as discussed in previous chapters: It seems quite obvious that one should naturally interpret $P[\boldsymbol{\sigma}]$ as the probability measure and consider $Q[\boldsymbol{\sigma}]$ as an observable being averaged. This understanding, in some sense, is a trap: while $Q[\boldsymbol{\sigma}]$ is critically sensitive to correlations between the replica auxiliary fields σ_k, the naïve measure $P[\boldsymbol{\sigma}]$ completely factorizes across replicas (i.e. it is insensitive to these essential correlations). As a consequence, a Monte Carlo implementation built on sampling sampling $\boldsymbol{\sigma}$ according to $P[\boldsymbol{\sigma}]$ will give outlandish values of $Q[\boldsymbol{\sigma}]$ that fluctuate wildly and may not converge to the expected value or may require a ludicrous number of samples. This feature is what in the lattice QCD area is often called an overlap problem (see e.g. Refs [48, 49]). The case at hand is especially challenging in two and three dimensions, as the magnitude of the determinant $Q[\boldsymbol{\sigma}]$ is expected to grow exponentially with the size of the boundary of the subregion A (see e.g. [25, 28]).

Motivated by the similarity between the numerator of Eq. (3.65) and the conventional path-integral form of partition functions, we address the overlap problem by first differentiating with respect to a parameter, then using Monte Carlo methods to compute that derivative, a much better behaved quantity, and finally integrating out the auxiliary parameter at the end. We outlined this algorithm in detail in the preceding chapter, and reproduce part of it here for completeness and notational cohesion.

We introduce a parameter $0 \le \lambda \le 1$ by defining an auxiliary function $\Gamma(\lambda; g)$ such that

$$\Gamma(\lambda; g) \equiv \int \mathcal{D}\Sigma \, P[\boldsymbol{\sigma}] \, Q^\lambda[\boldsymbol{\sigma}]. \tag{3.84}$$

Normalization of $P[\boldsymbol{\sigma}]$ implies that

$$\ln \Gamma(0; g) = 0, \tag{3.85}$$

while Eq. (3.65) implies

$$\ln \Gamma(1; g) = (1 - n)S_{n,A}. \tag{3.86}$$

59

Using Eq. (3.84),

$$\frac{\partial \ln \Gamma}{\partial \lambda} = \int \mathcal{D}\Sigma \ \tilde{P}[\boldsymbol{\sigma}; \lambda] \ \ln Q[\boldsymbol{\sigma}], \tag{3.87}$$

where

$$\tilde{P}[\boldsymbol{\sigma}; \lambda] \equiv \frac{1}{\Gamma(\lambda; g)} P[\boldsymbol{\sigma}] \ Q^\lambda[\boldsymbol{\sigma}] \tag{3.88}$$

is a well-defined, normalized probability measure which features the usual weight $P[\boldsymbol{\sigma}]$ as well as incorporating entanglement contribution $Q^\lambda[\boldsymbol{\sigma}]$. It is the latter factor that induces entanglement-specific correlations in the sampling of $\boldsymbol{\sigma}$ when doing so according to the probability measure $\tilde{P}[\boldsymbol{\sigma}; \lambda]$.

Thus, $S_{n,A}$ is calculated by using vanishing λ as a reference point and computing the full entropy $S_{n,A}$ via

$$S_{n,A} = \frac{1}{1-n} \int_0^1 d\lambda \ \langle \ln Q[\boldsymbol{\sigma}] \rangle_\lambda, \tag{3.89}$$

where

$$\langle X \rangle_\lambda = \int \mathcal{D}\Sigma \ \tilde{P}[\boldsymbol{\sigma}; \lambda] \ X[\boldsymbol{\sigma}]. \tag{3.90}$$

We thus obtain an integral form of the interacting Rényi entropy that can be computed using any MC method (see e.g. [32, 33, 34]), in particular hybrid Monte Carlo [35, 36] to tackle the evaluation of $\langle \ln Q[\boldsymbol{\sigma}] \rangle_\lambda$ as a function of λ. In application, we observe that $\langle \ln Q[\boldsymbol{\sigma}] \rangle_\lambda$ is a remarkably smooth function of λ, as exemplified in Fig. 3.4. It is therefore sufficient to perform the numerical integration using a uniform grid.

Section 3.4: Results: Two-body system

We solve the two-body problem by means of the ground-state-projection method outlined in a previous section which furnishes the full two-body wavefunction on the lattice. We ensure that the continuum limit is approached by solving the problem for several lattice sizes and by computing the renormalized coupling using the energy spectrum and Lüscher's formalism [84, 85]. The latter equation indicates that the relationship between the energy eigenvalues and the scattering phase shift $\delta(p)$ is given by

$$p \cot \delta(p) = \frac{1}{\pi L} \mathcal{S}(\eta) \tag{3.91}$$

where the parameter $\eta = \frac{pL}{2\pi}$ and L is the box size, such that the energy of the two-body problem is $E = p^2/m$; and

$$\mathcal{S}(\eta) \equiv \lim_{\Lambda \to \infty} \left(\sum_{\mathbf{n}} \frac{\Theta(\Lambda^2 - \mathbf{n}^2)}{\mathbf{n}^2 - \eta^2} - 4\pi\Lambda \right), \tag{3.92}$$

where the sum is over all three-dimensional integer vectors, and $\Theta(x)$ is the Heaviside function. The scattering phase shift determines the scattering parameters via

$$p \cot \delta(p) = -\frac{1}{a} + \frac{1}{2} r_{\text{eff}} p^2 + O(p^4),$$ (3.93)

where δ is the scattering phase shift, a is the scattering length, and r_{eff} is the effective range.

3.4.1: Low-lying entanglement spectrum

Once the matrix elements of the reduced density matrix $\hat{\rho}_A$ are calculated from the projected ground state wavefunction, as shown above, we obtain the eigenvalues using standard diagonalization routines to obtain the entanglement spectrum $\sigma(\hat{H}_A)$, which is defined as the spectrum of the entanglement Hamiltonian $\hat{H}_A$, where

$$\hat{\rho}_A = e^{-\hat{H}_A}.$$ (3.94)

In Fig. 3.5, we present our results for $\sigma(\hat{H}_A)$ for a cubic subregion A of linear size $L_A/L = 0.5$, for two particles in the BCS-BEC crossover, parametrized by the dimensionless coupling $(k_F a)^{-1}$, where k_F is the Fermi momentum (roughly the inter-particle separation in the periodic box, as for two particles there is of course no Fermi surface) and a is the s-wave scattering length. The latter was determined using the Lüscher formalism outlined in the previous section.

The main features of the spectrum can be described as follows. We first note that beyond the lowest four or five eigenvalues, indicated as as λ_1 through λ_5 in the bottom panel of Fig. 3.5, the multiplicity of eigenvalues grows suddenly and dramatically, forming a quasi-continuum. Here, we focus mostly on the lowest five eigenvalues for this reason and characterize the rest statistically in the next section. The dependence of all λ_k on $(k_F a)^{-1}$ is rather mild and smooth as is clear from the figure, although it has a few crisp features: there is a rather large gap between λ_1 and the next eigenvalue, which implies that the Rényi entanglement entropies are dominated by that lowest eigenvalue; there is a crossing of λ_2, λ_3 and λ_4 on the BEC side of the resonance; after that crossing λ_2 and λ_3 heal to λ_5 and effectively merge into the lower edge of the quasi-continuum part of the spectrum at large positive dimensionless coupling. The evolution of these properties along the crossover is shown in more detail in panels $a - e$ of Fig. 3.5.

In Fig. 3.6 we show the Schmidt gap Δ (see Refs [89]), defined as the separation between the two largest eigenvalues of the reduced density matrix $\hat{\rho}_A$, for $L_A/L = 0.1, 0.2, ..., 0.5$, as a function of $(k_F a)^{-1}$. Since we do not expect a quantum phase transition as a function of $(k_F a)^{-1}$, we similarly do not expect the Schmidt gap to vanish. As a result of the eigenvalue crossing explained above, however, there exists a sharp change

(in the sense of a discontinuous derivative) in Δ in the BCS-BEC crossover, which takes place in the strongly coupled region $0 < (k_F a)^{-1} < 1$. It is also evident that, because λ_1 and λ_4 track each other at a very nearly constant separation, the Schmidt gap becomes constant to the right of the sharp edge in Fig. 3.6. As with other features of this spectrum, it remains to be determined how Δ evolves as a function of particle number, in particular as a Fermi surface forms and Cooper pairing correlations emerge.

As mentioned above, our calculations were carried out in a periodic box. We show the corresponding finite-size effects in Fig. 3.7, where we show the lower entanglement spectrum of the two-body system as a function of the bare (unrenormalized) lattice coupling g. In that figure, it is clear that finite-size effects are smallest on the BCS side of the resonance, but become considerably more important on the BEC side as condensation sets in. This behavior is consistent with the expectation that, once a two-body bound state forms (as the coupling is increased away from the non-interacting point), the sensitivity to lattice-spacing effects is significantly enhanced. It is worth noting, in particular, that one may easily identify the unitary regime just by looking at this figure: for any given eigenvalue, the data for different lattice sizes crosses at about the same value of g; this coincidence is reminiscent of the finite-size scaling behavior of order parameters in critical phenomena, as it is the hallmark of scale invariance at phase transitions.

The process of reducing finite-size effects, at fixed particle number, implies approaching the dilute limit, i.e. using larger lattices. When that limit is approached, the renormalization prescription that replaces g with the physical coupling $(k_F a)^{-1}$ (described above) should force the finite-size calculations to collapse to a single, universal (in the sense of size-independent) curve. This is indeed what we find and what yields the results of Fig. 3.5.

3.4.2:   High entanglement spectrum

The entanglement spectrum $\sigma(\hat{H}_A)$ above λ_5, which we will refer to here as the high entanglement spectrum, displays a rapidly growing multiplicity of eigenvalues, as mentioned in the previous section, which we deem best to analyze using elementary statistical methods. In Fig. 3.8, we show the eigenvalue distribution of the high entanglement spectrum (the first quasi-continuous band that we observe) for different system sizes, in histogram form. More importantly, we find that the mean and standard deviation of that distribution, shown here in Fig. 3.8 (middle and bottom), are smooth functions of $(k_F a)^{-1}$; the mean, somewhat surprisingly, diverges as the coupling is turned off. We interpret this effect as strong evidence that the high sector of $\sigma(\hat{H}_A)$ is a non-perturbative component of the entanglement Hamiltonian that is entirely due to quantum fluctuations induced by the interaction. Although the two-body system has no Fermi surface, it seems intuitive to conjecture a link between Cooper pairing and the high entanglement spectrum. Determining

whether this is true, however, is a highly nontrivial problem that requires studying the high entanglement spectrum in the progression from few to many particles, a problem that is likely at the edge of what is currently possible if it is possible at all.

Our numerical calculations show a large number of eigenvalues that lie far (at least 9 to 10 orders of magnitude) above the high entanglement spectrum. While we cannot discard that those eigenvalues are consistent with numerical noise (they come from the lowest eigenvalues of the reduced density matrix), there are enough of them to warrant this brief comment. Although there is a large number of such eigenvalues, their contribution to the entanglement entropy is considerably suppressed by their incredibly small magnitude. We continue this discussion in the sections that follow.

3.4.3: Entanglement entropy

Having computed the eigenvalues of the entanglement Hamiltonian $\lambda_k \in \sigma(\hat{H}_A)$, the entanglement entropy of the two-body problem is now easily determined. The von Neumann entropy is defined as

$$S_{\text{vN},A} = -\text{Tr}_{\mathcal{H}_A}\left[\hat{\rho}_A \ln \hat{\rho}_A\right] = \sum_k \lambda_k \, e^{-\lambda_k}, \tag{3.95}$$

and the n-th order Rényi entanglement entropy is given by

$$S_{n,A} = \frac{1}{1-n} \ln \text{Tr}_{\mathcal{H}_A}\left[\hat{\rho}_A^n\right] = \frac{1}{1-n} \ln \sum_k e^{-n\lambda_k}. \tag{3.96}$$

In Fig. 3.9 (top panel), we show S_2 as a function of $x = k_F L_A$ and the coupling $(k_F a)^{-1}$. Remarkably, the trend towards the leading asymptotic behavior proportional to $x^2 \ln x$ appears to set in at $x \simeq 2$ for all couplings. This behavior is quite surprising, as there is nothing obvious that necessitates this convenient behavior. As we will find below, we observe the same sort of behavior for the many-body Fermi gas at resonance.

To explicitly demonstrate the effect of the high entanglement spectrum on S_2, which we referred to at the end of the previous section, we plot in Fig. 3.9 (bottom panel) the contribution ΔS_2 of the first entanglement eigenvalue to the full S_2. It is clear in that plot that the contribution is at most on the order of 8% for the parameter ranges we studied.

Section 3.5:   Results: Many-body system

By using the many-body lattice MC techniques described above (and in the previous chapter), along with the renormalization scheme outlined above, we calculated the first few entanglement entropies of the unitary Fermi gas, setting out to characterize its leading and sub-leading asymptotic behavior as a function of the subregion size $x = k_F L_A$.

The results depicted below were obtained by gathering approximately 250 decorrelated auxiliary field configurations (where a single "auxiliary field" contains all the replicas required to determine the desired Rényi entropy, that is, a single "field" refers to a single value of the collection abbreviated throughout this chapter) for each value of the auxiliary parameter λ. We used various particle numbers in the range $N = 4 - 400$ and cubic lattice sizes ranging throughout $N_x = 6 - 16$, all with periodic boundary conditions in space. The projection to the ground state was carried out by extrapolation to the limit of large imaginary-time direction. The auxiliary parameter λ was discretized using only $N_\lambda = 10$ points, which we found to be enough to capture the very mild dependence on that parameter, as explained in a previous section and as seen previously in the preceding chapter (see also Appendix .2 for further details).

Because the particular methods we implemented require as their base a discretization of spacetime, careful attention was paid to the ordering of the various length scales, to ensure that the thermodynamic and continuum limit were approached successfully and efficiently. Specifically, we required the following ordering:

$$k_F \ell \ll 1 \ll k_F L_A \ll k_F L, \tag{3.97}$$

where $\ell = 1$ is the lattice spacing, L_A is the sub-system size, and $L = N_x \ell = N_x$ is the full system size. The first condition on the left of Eq. (3.97) ensures that the continuum limit is approached; the second condition implies that the region determined by L_A must contain many particles (since the density is the only scale in the system, this condition defines the large-L_A regime); and the last condition means that $L_A \ll L$, to ensure finite-size effects are minimized. This ordering was accomplished by carefully choosing the restrictions on L_A for each given particle number N, while aiming to maintain a large N. The latter, however, requires L to be large in order to avoid high densities where $k_F \simeq 1$, which can be sensitive to lattice-spacing effects. In addition, we set $L_A \leq 0.45L$ as a compromise to satisfy the last inequality, a condition we derived by studying the finite-size effects present in lattice treatments of the free gas.

Shown in Fig. 3.10 are our MC results of the second Rényi entropy S_2 of the resonant Fermi gas in various volumes of N_x^3 lattice points, where $N_x = 6 - 16$, as a function of the dimensionless parameter $x = k_F L_A$, for cubic subsystems of side L_A. The results for different volumes clearly coincide within the statistical uncertainty, shown in colored bands, which indicates that our results are in the appropriate continuum and

thermodynamic regimes.

The inset of Fig. 3.10 depicts S_2 scaled by x^2 in a semi-log plot. The fact that the trend is clearly linear supports the assertion that x is large enough to discern the asymptotic regime, where $S_2/x^2 \propto \ln x$. As in the case of the non-interacting Fermi gas, mentioned in the Introduction, this onset of the asymptotic regime appears to be at $x \simeq 2$.

3.5.1: Rényi entanglement entropies

We calculated $S_{n,A}$ for the resonant Fermi gas for $n = 2, 3, 4, 5$, as a function of $x = k_F L_A$ using the formalism presented above for the determination of Rényi entanglement entropies for $n \geq 2$. In Fig. 3.11 we display our main MC results. To interpret this data, we briefly discuss the noninteracting case. In Refs. [2, 3, 4, 5, 6] it was demonstrated that the leading-order behavior or the entanglement entropy of non-interacting 3D fermions as a function of x is given by

$$S_{n,A}(x) = c(n)x^2 \ln x + o(x^2), \tag{3.98}$$

where the leading coefficient satisfies the formula

$$c(n) = \frac{1 + n^{-1}}{24(2\pi)^{d-1}} \int_{\partial\Omega} \int_{\partial\Sigma} dS_x dS_k \, |\hat{\mathbf{n}}_x \cdot \hat{\mathbf{n}}_k| \tag{3.99}$$

and where Ω is the real-space region A scaled to unit volume with normal $\hat{\mathbf{n}}_x$, Σ is the Fermi volume scaled by the Fermi momentum with unit normal $\hat{\mathbf{n}}_k$. In our present case, A is a cubic subsystem (as in Fig. 3.1) and a spherical Fermi volume.

The free case is given in Fig. 3.11 in two useful ways. The asymptotic result at large x is shown with crosses on the rightmost edge of the plot, carried partway into the plot (in an effort to guide the eye) with dashed black horizontal lines for each order we computed: $n = 2, 3, 4, 5$ (top to bottom). With a thick red dashed line we show the case $n = 2$ at finite x, as obtained from the overlap-matrix method [87].

Our results for $S_{n,A}$ for the resonant Fermi gas (data points with error bands) appear to heal to the noninteracting limit when the slow decay (see below) to a constant at large x is taken into account; this statement holds especially in the $n = 2$ case where the sub-leading oscillations allow for a relatively clean fit. Indeed, our fits for $n = 2$ give

$$S_{2,A}(x) = ax^2 \ln x + bx^2, \tag{3.100}$$

with $a = 0.114(2)$ and $b = 0.04(1)$, while Eq. (3.99) yields $c(2) = 3/(8\pi) \simeq 0.119366\ldots$ While our value and the value for the free $c(2)$ are different to within our uncertainties, they are shockingly similar (between

3 and 6%). The sub-leading behavior is consistent with an area law $\propto x^2$. As n is increased, sub-leading oscillations become increasingly important; however, they are inoffensive enough that it is still possible to discern the asymptotic behavior at large x. For $n = 3, 4, 5$, oscillations notwithstanding, the results in the large-x limit appear again to be close to the noninteracting case.

From our results for the entanglement entropies S_n as a function of n, it is possible to use the power method to extract the lowest eigenvalue λ_1 of the entanglement spectrum as a function of x. We studied the decay of $(1 - n)S_n/n$ to a constant value which, given Eq. (3.96), we identified as $-\lambda_1$. In Fig. 3.12 we show the result of using that sole eigenvalue to approximate S_n. As expected, higher orders n emphasize the contribution from the lowest entanglement eigenvalue (highest eigenvalue of the reduced density matrix), which progressively dominates S_n as n increases. From the n dependence of S_n, it is also possible to study the degeneracy of the lowest entanglement eigenstate; at large n,

$$\frac{(1 - n)}{n} S_n \simeq \frac{\ln d_1}{n} - \lambda_1 + \dots, \tag{3.101}$$

where the ellipsis indicates exponentially suppressed terms, and d_1 is the degeneracy associated with λ_1. We find a vanishing first term, which indicates that d_1 is consistent with unity.

Section 3.6:   Summary and conclusions

In this chapter, we successfully implemented two different lattice methods, one detailed in an earlier chapter, to non-perturbatively characterize the entanglement properties of three-dimensional spin-1/2 fermions in the strongly interacting, unitary regime of short interaction range and large scattering length, i.e. the resonant limit. This region of parameter space is scale invariant (in fact, non-relativistic conformal invariant) in the sense that it presents as many scales as non-interacting gases, and therefore its properties are universal characteristics of fundamental three-dimensional quantum mechanics, i.e. in the same sense as critical exponents that characterize phase transitions.

We computed the two-body spectrum of the entanglement Hamiltonian along the BCS-BEC crossover and well-characterized results for the low-lying part, which displays clear features as the strength of the coupling is varied, such as eigenvalue crossings close to the resonance point, scale invariance, and eigenvalue merging in the BEC limit. The lowest two eigenvalues in the spectrum correspond to the largest two eigenvalues of the reduced density matrix, which are separated by the Schmidt gap which we present. We found that this quantity shows a sharp change at strong coupling, in the vicinity of the conformal point $(k_F a)^{-1} = 0$.

We also carried out a statistical characterization of the high entanglement spectrum, which appears as

a quasi-continuum distribution with well defined mean and standard deviation, which we mapped out along the crossover. We found that the mean of the distribution tends to infinity in the noninteracting limit, which indicates that that sector is due to non-perturbative effects in the entanglement Hamiltonian. In contrast, the low-lying part of the spectrum has a finite noninteracting limit. All of the above two-body results were obtained with non-perturbative non-stochastic methods which are easily generalizable to higher particle numbers (as we show analytically and diagramatically for 3 particles).

In addition, we studied the Rényi entropies of degree $n = 2, 3, 4$, and 5 of many fermions in the unitary limit, which we calculated using a method recently developed by us (based on an enhanced version of the algorithm of Ref. [1]). We found that, remarkably, the large $x = k_F L_A$ (i.e. subsystem size) limit for those entanglement entropies sets in for x as low as 2.0, which allowed us to characterize the leading and sub-leading asymptotic behavior using $2 \leq x \leq 10$. For entropies of order $n > 2$, on the other hand, we found that sub-leading oscillations are enhanced, but not enough to spoil the visualization of the asymptotic behavior at large x.

Our experience with Monte Carlo calculations of $S_{n,A}$ in 1D gave us empirical indication that the entanglement properties of the unitary Fermi gas might not be too different from those of a non-interacting gas. However, since unitarity corresponds to a strongly correlated, three-dimensional point, that intuition could very well have been wrong. Our calculations indicate that the leading-order asymptotic behavior is approximately consistent with that of a non-interacting system, while the sub-leading behavior is clearly different.

The recent measurement of the second Rényi entropy of a bosonic gas in an optical lattice [64, 65] shows that it is possible to experimentally characterize the entanglement properties of the kind of system analyzed here. Our calculations are therefore predictions for such experiments for the case of fermions tuned to the unitary limit.

Section .1: Exact evaluation of the path integral for finite systems

In order to illustrate the details as well as the generality of our few-body technique, we evaluate the path integral for a four-component tensor from which each of the above traces may be obtained by suitable index contraction.

Toward this end, we first define

$$R_{ac,bd} = \int \mathcal{D}\sigma \, \boldsymbol{U}[\sigma]_{ab} \, \boldsymbol{U}[\sigma]_{cd}. \tag{102}$$

We first write out each of the matrices $\boldsymbol{U}[\sigma]$ in its product form. That is, we reintroduce the expression

$$\boldsymbol{U}[\sigma] = \prod_{j=1}^{N_\tau} \boldsymbol{U}_j[\sigma]. \tag{103}$$

For each individual contribution to the N-body transfer matrix, exactly N factors of the matrix $\boldsymbol{U}[\sigma]$ appear, and as a result each temporal lattice point appears in the integrand exactly N times. Writing out the integrand and grouping the components according to their associated timeslice, we obtain

$$
\begin{aligned}
R_{ac,bd} &= \int \mathcal{D}\sigma \, \boldsymbol{U}[\sigma]_{ab} \, \boldsymbol{U}[\sigma]_{cd} = \int \mathcal{D}\sigma \, \Big(\boldsymbol{U}_1[\sigma] \, \boldsymbol{U}_2[\sigma] \, \ldots \, \boldsymbol{U}_{N_\tau}[\sigma]\Big)_{ab} \Big(\boldsymbol{U}_1[\sigma] \, \boldsymbol{U}_2[\sigma] \, \ldots \, \boldsymbol{U}_{N_\tau}[\sigma]\Big)_{cd} \tag{104} \\[2mm]
&= \sum_{\substack{k_1,k_2,\ldots,k_{N_\tau-1} \\ l_1,l_2,\ldots,l_{N_\tau-1}}} \int \mathcal{D}\sigma \, \Big(\boldsymbol{U}_1[\sigma]_{ak_1} \, \boldsymbol{U}_1[\sigma]_{cl_1}\Big) \Big(\boldsymbol{U}_2[\sigma]_{k_1k_2} \, \boldsymbol{U}_2[\sigma]_{l_1l_2}\Big) \, \ldots \, \Big(\boldsymbol{U}_{N_\tau}[\sigma]_{k_{N_\tau-1}b} \, \boldsymbol{U}_{N_\tau}[\sigma]_{l_{N_\tau}d}\Big) \tag{105} \\[2mm]
&= \sum_{\substack{k_1,k_2,\ldots,k_{N_\tau-1} \\ l_1,l_2,\ldots,l_{N_\tau-1}}} \prod_{j=1}^{N_\tau} \left(\int \mathcal{D}\sigma(\tau_j) \, \boldsymbol{U}_j[\sigma]_{k_{j-1}k_j} \, \boldsymbol{U}_j[\sigma]_{l_{j-1}l_j}\right), \tag{106}
\end{aligned}
$$

where we set $k_0 = a$, $l_0 = c$, $k_{N_\tau} = b$, and $l_{N_\tau} = d$ in order to match the diagrams presented above, and used the notation

$$\mathcal{D}\sigma(\tau) \equiv \prod_{\mathbf{r}} \frac{d\sigma(\mathbf{r},\tau)}{2\pi}. \tag{107}$$

Using the specific form of the individual $\mathbf{U}$ factors, we find

$$\int \mathcal{D}\sigma(\tau_j) \boldsymbol{U}_j[\sigma]_{k_{j-1}k_j} \boldsymbol{U}_j[\sigma]_{l_{j-1}l_j} \tag{108}$$

$$= \sum_{\substack{p,q \\ p',q'}} \int \mathcal{D}\sigma(\tau_j) \big(\boldsymbol{T}_{k_{j-1}p}\boldsymbol{V}_j[\sigma]_{pq}\boldsymbol{T}_{qk_j}\big)\big(\boldsymbol{T}_{l_{j-1}p'}\boldsymbol{V}_j[\sigma]_{p'q'}\boldsymbol{T}_{q'l_j}\big),$$

which using our chosen form of $\mathbf{V}$ becomes

$$= \sum_{\substack{p,q \\ p',q'}} \boldsymbol{T}_{k_{j-1}p}\boldsymbol{T}_{qk_j}\boldsymbol{T}_{l_{j-1}p'}\boldsymbol{T}_{q'l_j}\delta_{pq}\delta_{p'q'} \, \times$$

$$\int \mathcal{D}\sigma(\tau_j) \big(1 + A \, \sin\sigma(p,\tau_j)\big)\big(1 + A \, \sin\sigma(p',\tau_j)\big)$$

$$= \sum_{\substack{p,q \\ p',q'}} \boldsymbol{T}_{k_{j-1}p}\boldsymbol{T}_{qk_j}\boldsymbol{T}_{l_{j-1}p'}\boldsymbol{T}_{q'l_j}\delta_{pq}\delta_{p'q'} \big(1 + (e^{\tau g} - 1)\delta_{pp'}\big),$$

where we used

$$\int \mathcal{D}\sigma(\tau_j) \ \left(1 + A \ \sin \sigma(p, \tau_j)\right) \left(1 + A \ \sin \sigma(p', \tau_j)\right)$$
$$= \ \left(1 + (e^{\tau g} - 1)\delta_{pp'}\right). \tag{109}$$

Thus, we naturally arrive at the definition

$$[M_2]_{ac,bd} \ = \ \mathcal{K}_{ab}\mathcal{K}_{cd} + (e^{\tau g} - 1)\mathcal{I}_{abcd}, \tag{110}$$

as the transfer matrix in the two-particle subspace, where

$$\mathcal{K}_{ij} \ = \ \sum_p \boldsymbol{T}_{ip}\boldsymbol{T}_{pj}, \tag{111}$$

$$\mathcal{I}_{ijkl} \ = \ \sum_p \boldsymbol{T}_{ip}\boldsymbol{T}_{pj}\boldsymbol{T}_{kp}\boldsymbol{T}_{pl}. \tag{112}$$

Indeed, this definition of M_2 as a transfer matrix makes sense, because

$$R_{ac,bd} = \sum_{\substack{k_1, k_2, \ldots, k_{N_\tau - 1} \\ l_1, l_2, \ldots, l_{N_\tau - 1}}} \prod_{j=1}^{N_\tau} [M_2]_{k_{j-1}k_j, l_{j-1}l_j}, \tag{113}$$

or more succinctly,

$$R_{ac,bd} = \left[M_2^{N_\tau}\right]_{ac,bd}. \tag{114}$$

In a similar fashion, one may show without much difficulty that the transfer matrix of the three-body problem (for distinguishable particles, i.e. no symmetrization or antisymmetrization is enforced) is

$$[M_3]_{abc,def} = \mathcal{K}_{ad}\mathcal{K}_{be}\mathcal{K}_{cf} + (e^{\tau g} - 1)\mathcal{J}_{abc,def}, \tag{115}$$

where

$$\mathcal{J}_{ijk,lmn} = \mathcal{K}_{il}\mathcal{I}_{jkmn} + \mathcal{K}_{jm}\mathcal{I}_{ikln} + \mathcal{K}_{kn}\mathcal{I}_{ijlm}. \tag{116}$$

The pattern from this point on is clearly visible: there is one term for each 'spectator' particle that does not participate in the interaction, while the other two are accounted for by an interacting term governed by the $\mathcal{I}_{abcd}$ object. One may thus infer the form of the transfer matrix for higher particle numbers and conjecture its form for more complex interactions.

Section .2:   Auxiliary parameter dependence

In this Appendix we give a few additional examples on the surprisingly mild dependence of the entanglement-entropy derivative $\langle \ln Q[\boldsymbol{\sigma}] \rangle_\lambda$ as other parameters are varied. In all cases, the data shown corresponds to full three-dimensional calculations in the conformal regime.

In Fig. 13 (top) we show the variation of that derivative when the Rényi order is changed from $n = 2$ to $n = 5$, at fixed particle number and region size. In Fig. 13 (bottom) we show how $\langle \ln Q[\boldsymbol{\sigma}] \rangle_\lambda$ changes when the particle number is varied, at fixed Rényi order n.
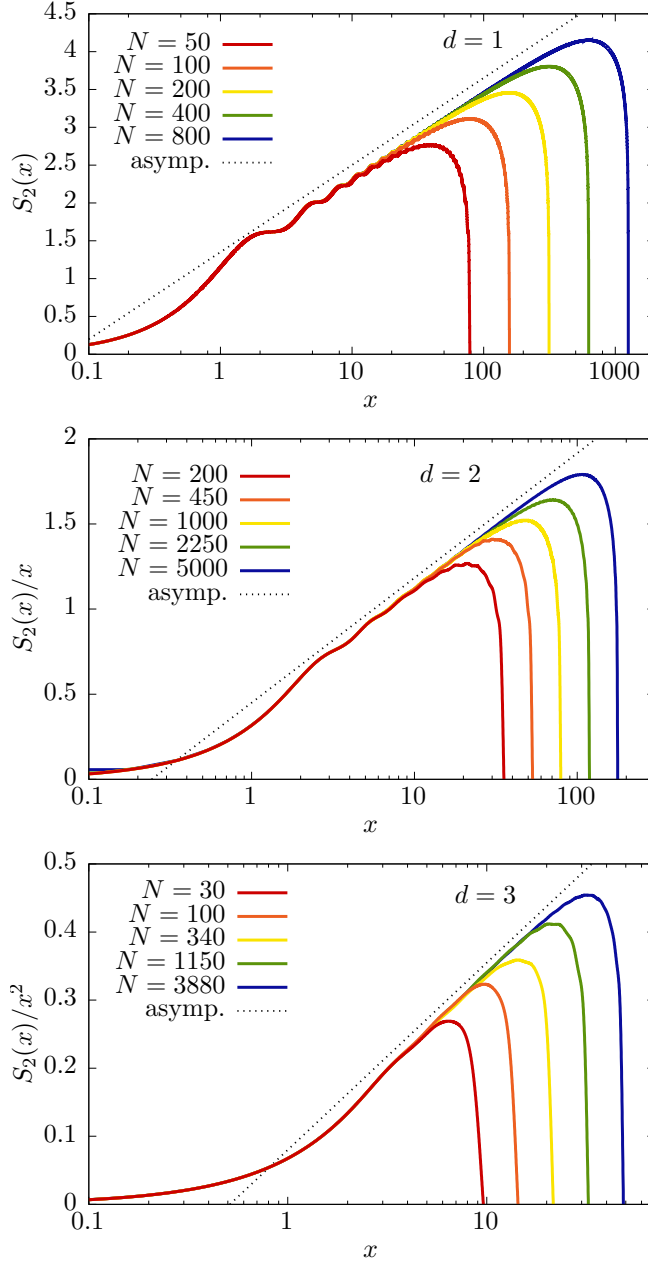
Figure 3.2: Second Rényi entropy S_2 of N non-interacting fermions in $d = 1, 2$, and 3 dimensions (top to bottom) as a function of $x = k_F L_A$, where A is a segment, square, and cubic region, respectively, and L_A is the corresponding linear size; k_F is the Fermi momentum. The entropy S_2 is scaled by the surface area dependence, namely x and x^2 in two and three dimensions, respectively. The x axis is plotted logarithmically to show that, up to finite-size effects, the results heal to the expected asymptotic regime of linear dependence with $\log_{10} x$ (dashed line). This regime sets in at $x \simeq 2-4$ across all d. Finite-size effects appear as a sudden drop at large x.
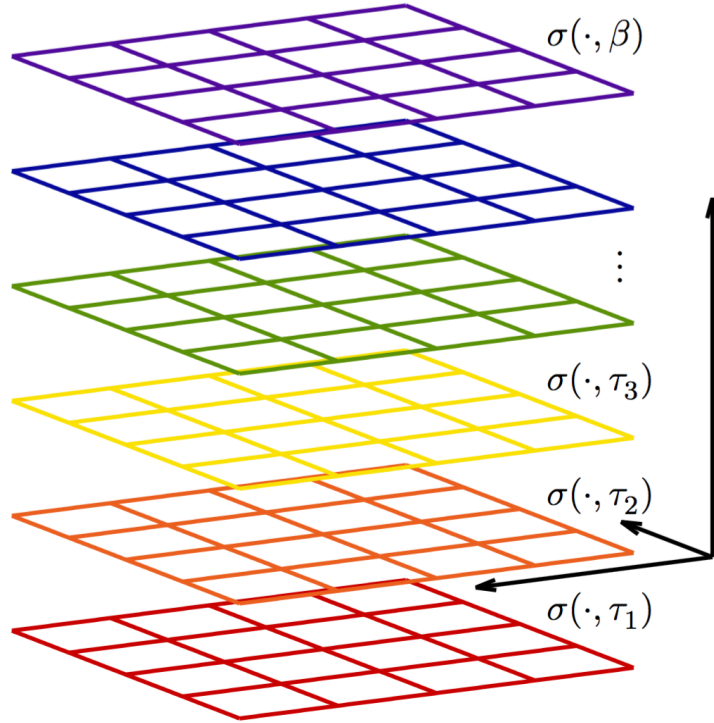
Figure 3.3: Depicted here is a schematic representation of the lattice that we used in our entanglement calculations. Each horizontal lattice slice represents the three-dimensional spatial lattice where the system lives, and the vertical stacking of the planes is meant to represent the imaginary time direction. Although the original Hamiltonian is time-independent, the auxiliary field σ that represents the interaction is supported by a larger spacetime lattice and induces a time dependence that disappears upon averaging over this field.
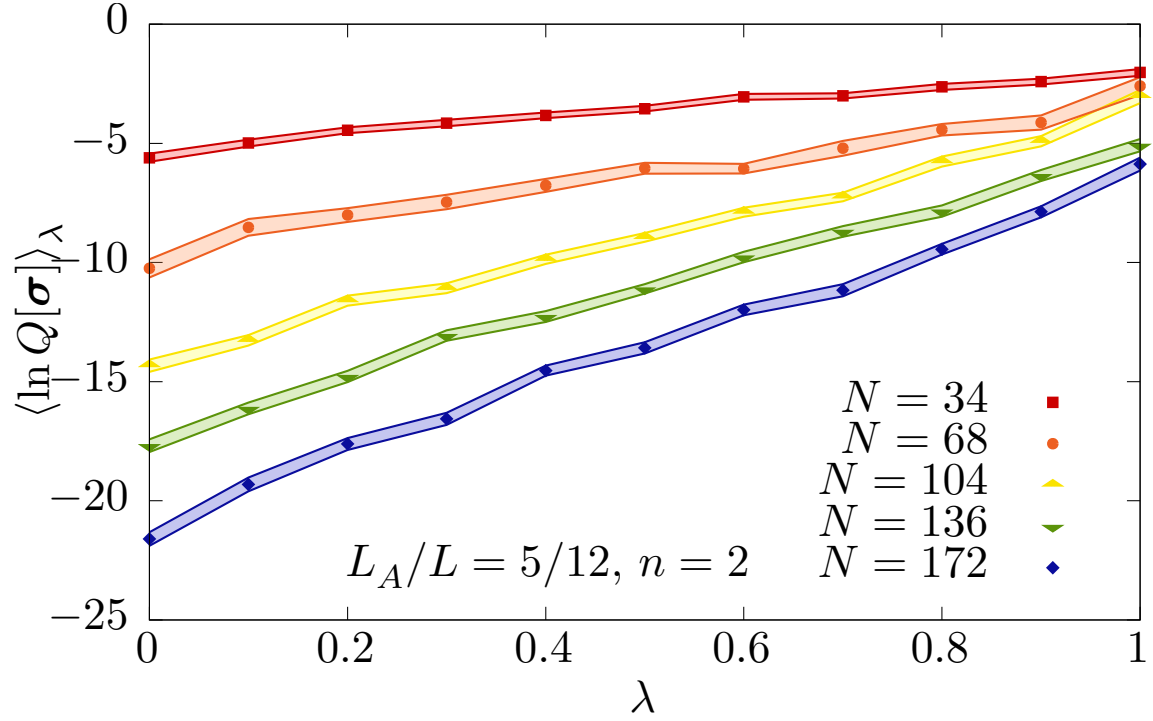
Figure 3.4: The λ dependence of $\langle \ln Q[\boldsymbol{\sigma}] \rangle_\lambda$ for a subsystem of size $L_A = 5/12L$, for systems of $N = 34, 68, 104, 136, 172$ fermions tuned to unitarity in a box of size $L = N_x \ell$ (where $N_x = 12$ points and $\ell = 1$), and for Rényi order $n = 2$. Similar plots are obtained by varying, instead of the particle number, the region size and the Rényi order. These are shown in Appendix .2.
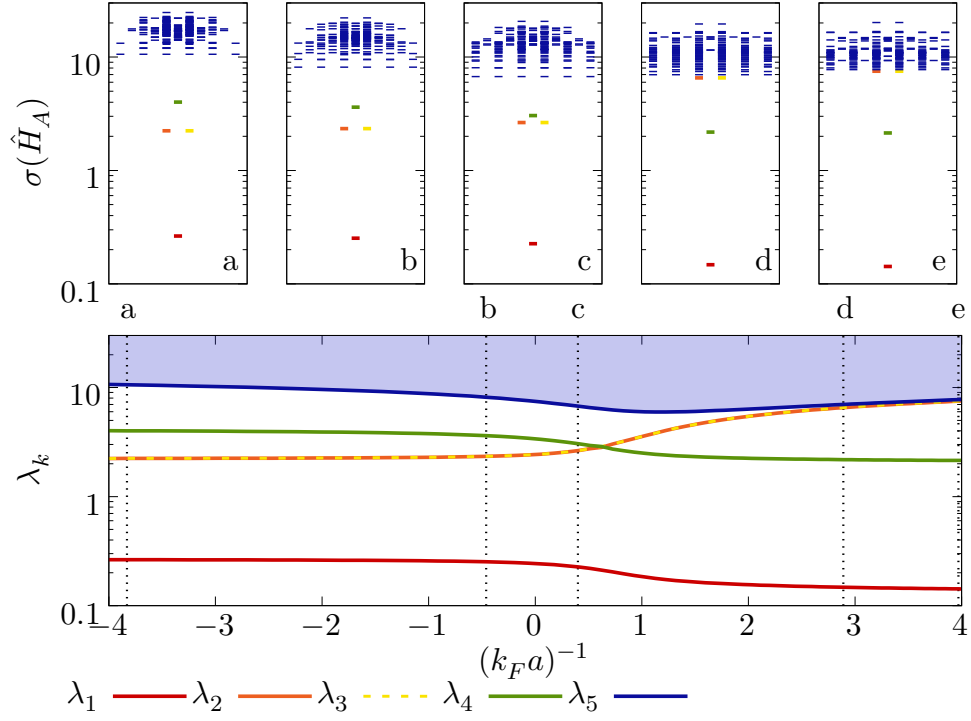
Figure 3.5: Bottom panel: Low-lying entanglement spectrum of the two-body problem as a function of the dimensionless coupling $(k_F a)^{-1}$ in the BCS-BEC crossover regime, for a cubic subregion A of linear size $L_A/L = 0.5$. Top panels (a - e): Low-lying (and part of the excited) entanglement spectrum for selected couplings (a - e) at the top of the bottom panel.
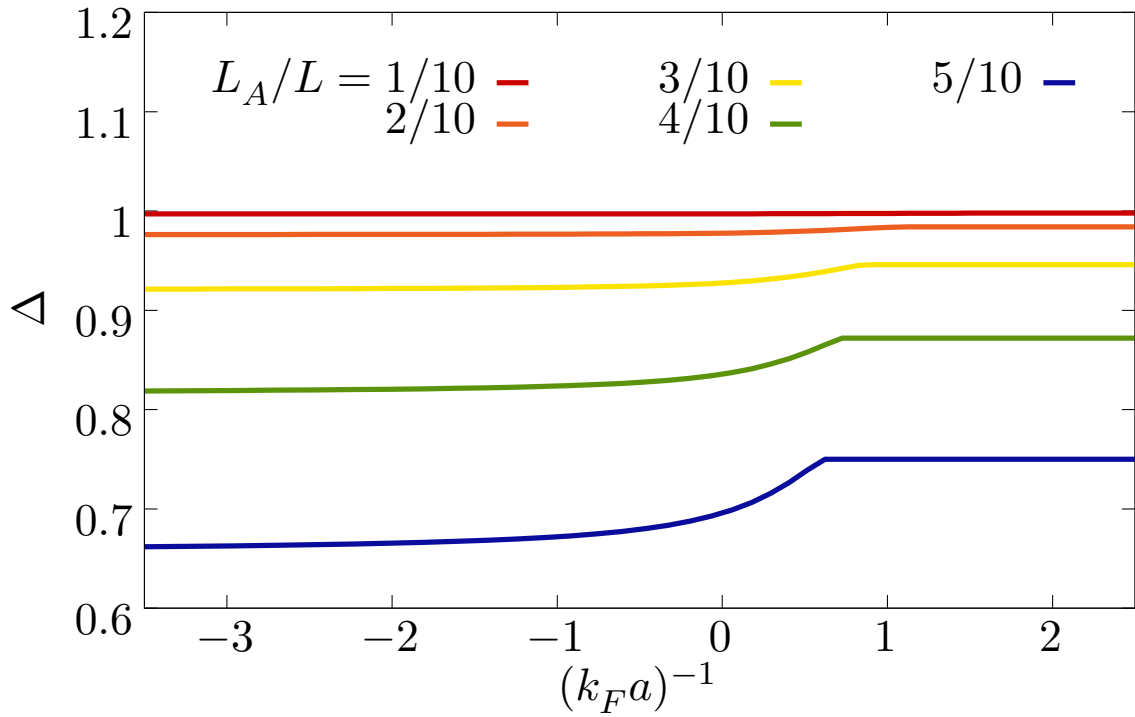
Figure 3.6: The Schmidt gap Δ between the two largest eigenvalues of the reduced density matrix, i.e. the two smallest entanglement eigenvalues, at $L_A/L = 0.1, 0.2, ..., 0.5$ (top to bottom), for the two-body system as a function of the coupling $(k_F a)^{-1}$
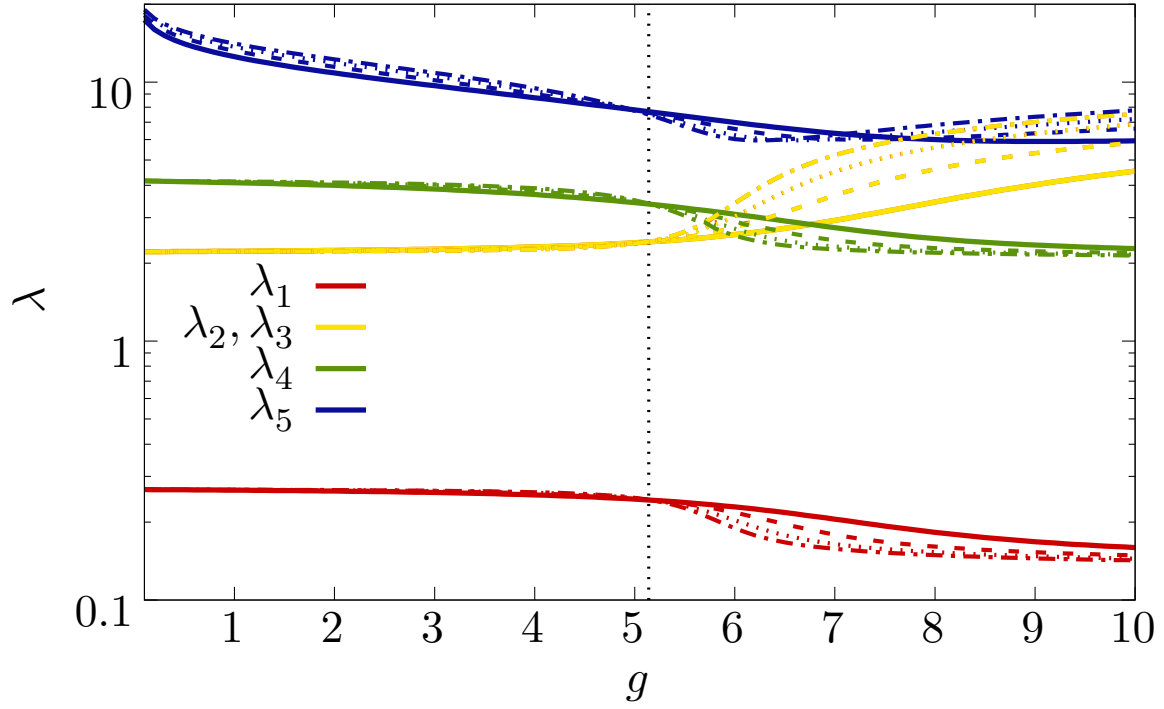
Figure 3.7: The entanglement spectrum of the two-body problem in the BCS-BEC crossover regime as a function of the bare lattice coupling at a few lattice sizes: solid, dashed, dotted, dash-dotted, for $N_x = 4, 6, 8, 10$, respectively. The subsystem size was fixed to $L_A/L = 0.5$. The coupling corresponding to the unitary point is marked with a vertical dashed line. Note how different volumes cross precisely at unitarity, which reflects the property of scale invariance characteristic of this particular system.
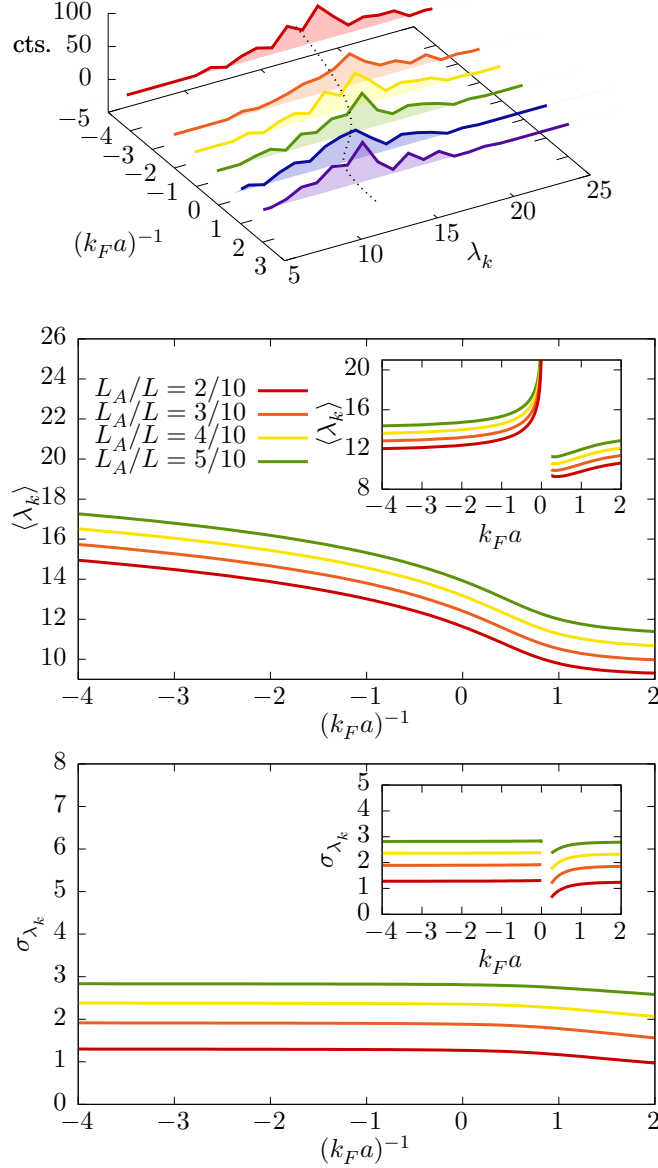
Figure 3.8: Top: A histogram of the higher entanglement spectrum of the two-body problem showing the number of counts (cts.) as a function of the physical coupling $(k_F a)^{-1}$ and the entanglement eigenvalue λ_k, for region size $L_A/L = 1/2$. The dashed line highlights the dependence of the mean (see also the middle plot). Middle and bottom: The mean and standard deviation, respectively, of the high entanglement spectrum distribution, as functions of the dimensionless interaction strength $(k_F a)^{-1}$ (main) and $k_F a$ (inset). In each plot the different curves show results for various region sizes L_A/L. Note that the weak coupling limit corresponds to $k_F a \to 0^-$.
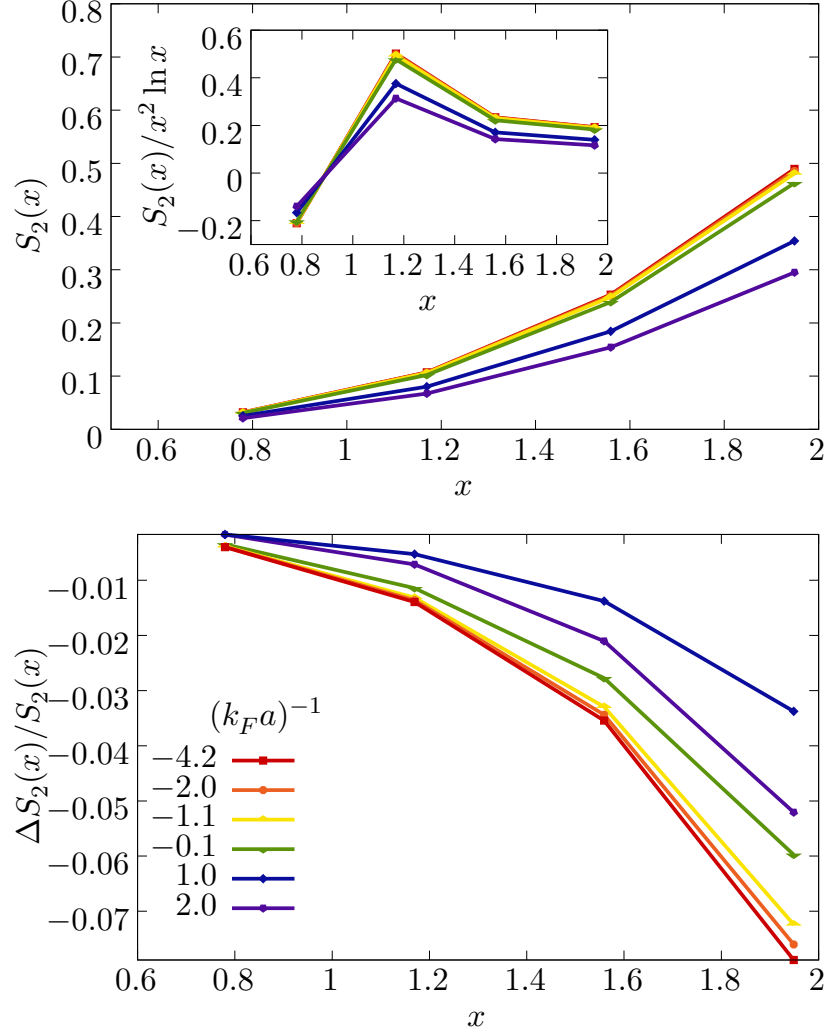
Figure 3.9: Top: The second Rényi entanglement entropy S_2 of the two-body problem as a function of $x = k_F L_A$ and for several values of the coupling $(k_F a)^{-1}$. Inset: The entropy S_2 scaled by $x^2 \ln x$. Bottom: The relative contribution of the high entanglement spectrum to the second Rényi entanglement entropy S_2, as a function of $x = k_F L_A$.
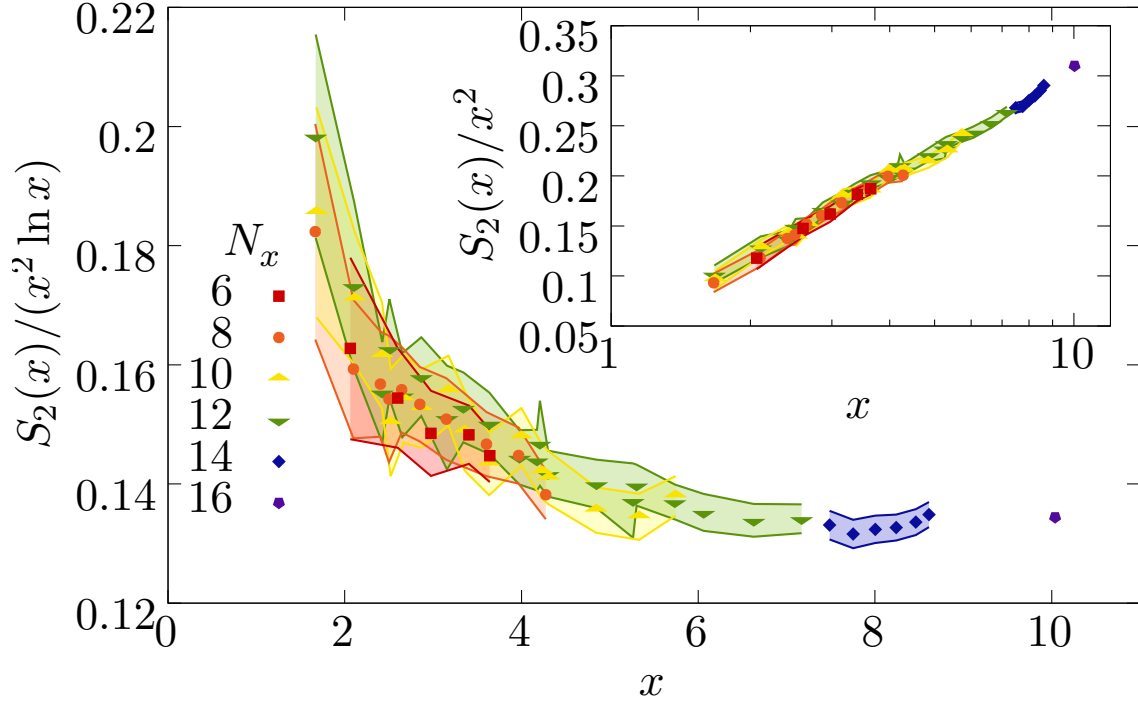
Figure 3.10: The second Rényi entropy of the resonant Fermi gas given in units of $x^2 \ln x$ (main) and x^2 (inset), where we define the parameter $x = k_F L_A$. We note the use of a linear scale in the main plot and logarithmic scale in the inset. Although the range of values of x is fundamentally limited by our computational power (as set by method and hardware), the fact that the main plot is consistent with a straight line is strongly supportive of the conclusion that the leading behavior of the entanglement entropy as a function of x is logarithmic. Additionally, we see that that behavior sets in as early as $x \simeq 2$, which thankfully is roughly consistent with the non-interacting case shown in Fig. 3.2.
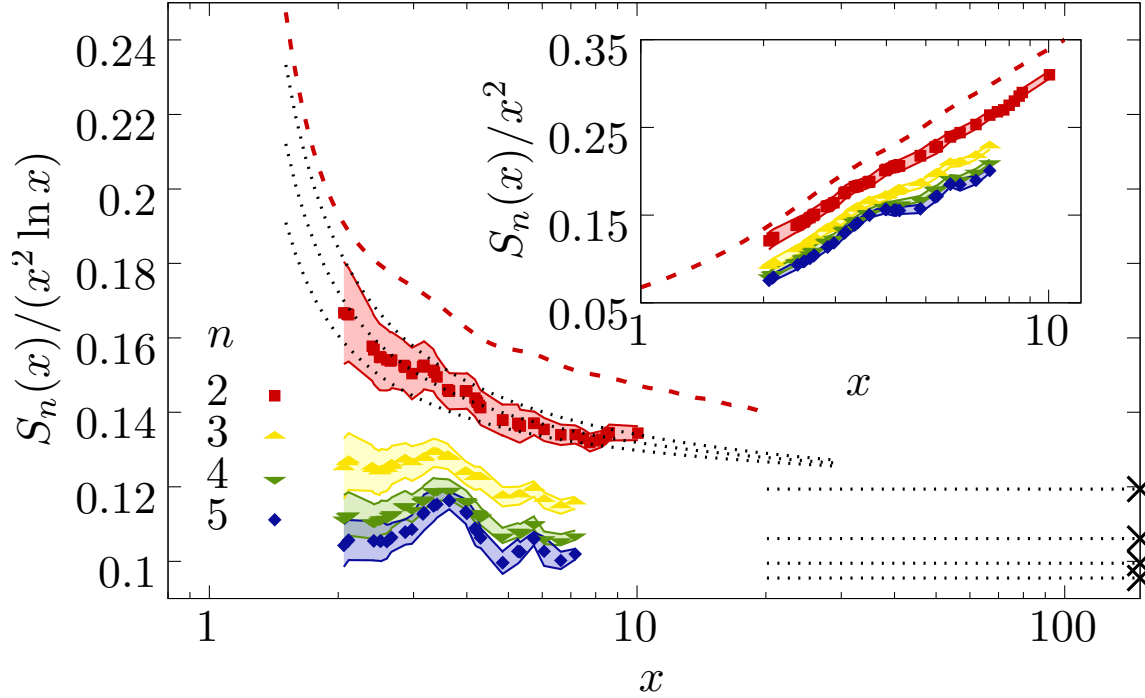
Figure 3.11: Rényi entropies of order $n = 2, 3, 4, 5$ (data points with error bands in red, yellow, green, and blue, respectively) of the unitary Fermi gas in units of $x^2 \ln x$ (main plot) and x^2 (inset), where $x = k_F L_A$. Note the logarithmic scale in the x axis. The red dashed line shows the non-interacting result for $n = 2$, obtained using the overlap matrix method. The black dotted lines plotted over the $n = 2$ data correspond to a fit the functional form $f(x) = a + b/\ln(x)$ (central line, with uncertainties marked by upper and lower dotted lines). The crosses on the right, and the corresponding horizontal dotted lines, indicate the expected asymptotic value $c(n)$ (from top to bottom, for $n = 2, 3, 4, 5$) for a non-interacting gas (see Refs. [2, 3, 4, 5, 6]), which we reproduce in Eq. (3.99); numerically, they are $c(2) = 0.11937...$, $c(3) = 0.10610...$, $c(4) = 0.09947...$, and $c(5) = 0.09549...$.
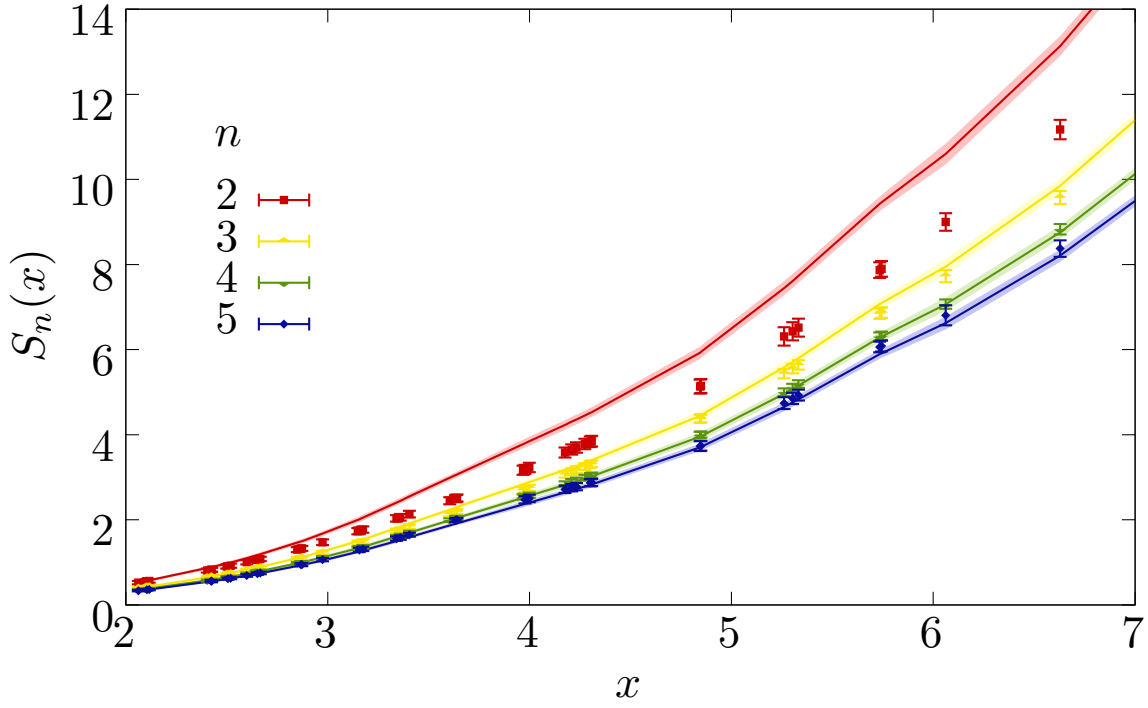
Figure 3.12: Rényi entanglement entropy S_n as a function of $x = k_F L_A$ for $n = 2, 3, 4, 5$ (top to bottom). Monte Carlo results are shown as data points with error bars. The solid lines show the result of computing S_n using only the lowest entanglement eigenvalue λ_1, i.e. the approximation $S_n = \frac{n}{n-1}\lambda_1$. Uncertainties appear as shaded regions around the central value.
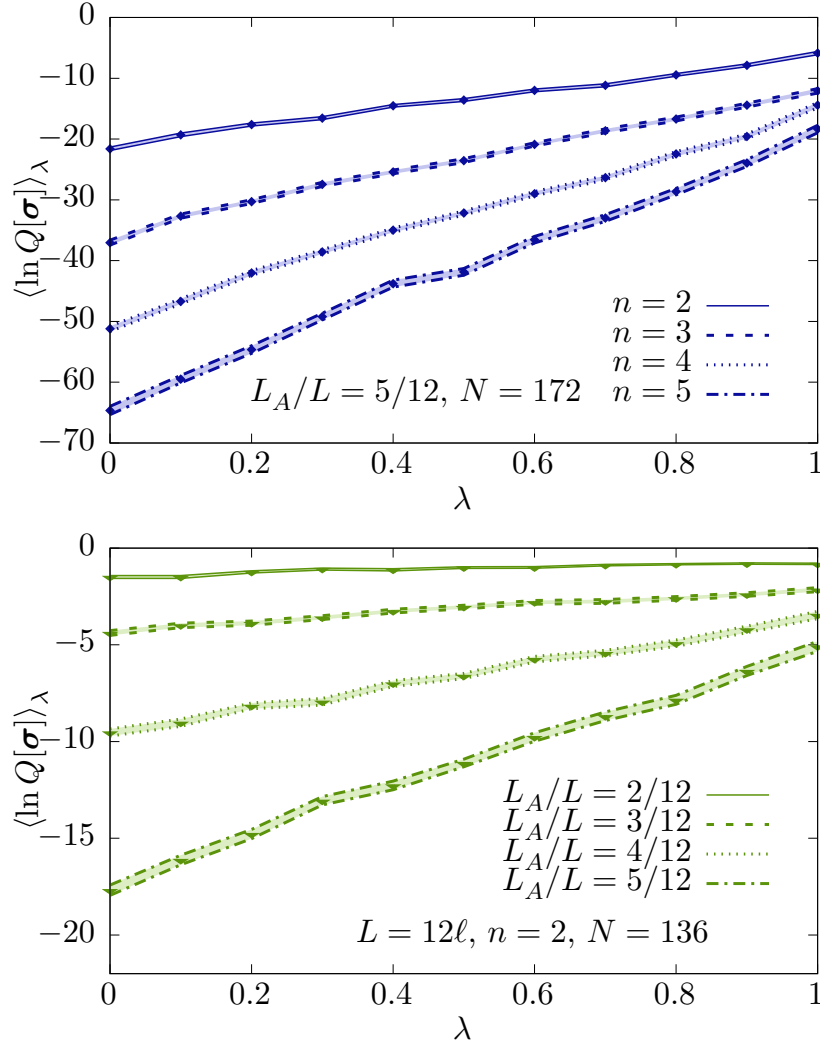
Figure 13: Top: λ dependence of $\langle \ln Q[\boldsymbol{\sigma}] \rangle_\lambda$ for several Rényi orders $n = 2, 3, 4, 5$, for subsystem size $L_A = 5/12L$, for $N = 172$ fermions at unitarity in a box of size $L = N_x \ell$ (where $N_x = 12$ points and $\ell = 1$). Bottom: λ dependence of $\langle \ln Q[\boldsymbol{\sigma}] \rangle_\lambda$ for several subsystem sizes L_A, for $N = 136$ fermions at unitarity in a box of size $L = N_x \ell$ (where $N_x = 12$ points and $\ell = 1$), and for Rényi order $n = 2$.

REFERENCES

[1] Tarun Grover. Entanglement of interacting fermions in quantum monte carlo calculations. *Phys. Rev. Lett.*, 111:130402, Sep 2013.

[2] Michael M. Wolf. Violation of the entropic area law for fermions. *Phys. Rev. Lett.*, 96:010404, Jan 2006.

[3] Dimitri Gioev and Israel Klich. Entanglement entropy of fermions in any dimension and the widom conjecture. *Phys. Rev. Lett.*, 96:100503, Mar 2006.

[4] P. Calabrese, M. Mintchev, and E. Vicari. Entanglement entropies in free-fermion gases for arbitrary dimension. *EPL (Europhysics Letters)*, 97(2):20009, 2012.

[5] Wenxin Ding, Alexander Seidel, and Kun Yang. Entanglement entropy of fermi liquids via multidimensional bosonization. *Phys. Rev. X*, 2:011012, Mar 2012.

[6] Hajo Leschke, Alexander V. Sobolev, and Wolfgang Spitzer. Scaling of rényi entanglement entropies of the free fermi-gas ground state: A rigorous proof. *Phys. Rev. Lett.*, 112:160403, Apr 2014.

[7] Luigi Amico, Rosario Fazio, Andreas Osterloh, and Vlatko Vedral. Entanglement in many-body systems. *Rev. Mod. Phys.*, 80:517–576, May 2008.

[8] J. Eisert, M. Cramer, and M. B. Plenio. *Colloquium* : Area laws for the entanglement entropy. *Rev. Mod. Phys.*, 82:277–306, Feb 2010.

[9] Ryszard Horodecki, Paweł Horodecki, Michał Horodecki, and Karol Horodecki. Quantum entanglement. *Rev. Mod. Phys.*, 81:865–942, Jun 2009.

[10] G. Vidal, J. I. Latorre, E. Rico, and A. Kitaev. Entanglement in quantum critical phenomena. *Phys. Rev. Lett.*, 90:227902, Jun 2003.

[11] Alexei Kitaev and John Preskill. Topological entanglement entropy. *Phys. Rev. Lett.*, 96:110404, Mar 2006.

[12] Michael Levin and Xiao-Gang Wen. Detecting topological order in a ground state wave function. *Phys. Rev. Lett.*, 96:110405, Mar 2006.

[13] Mark Srednicki. Entropy and area. *Phys. Rev. Lett.*, 71:666–669, Aug 1993.

[14] Pasquale Calabrese and John Cardy. Entanglement entropy and quantum field theory. *Journal of Statistical Mechanics: Theory and Experiment*, 2004(06):P06002, 2004.

[15] Curtis Callan and Frank Wilczek. On geometric entropy. *Physics Letters B*, 333(1):55 – 61, 1994.

[16] P.V. Buividovich and M.I. Polikarpov. Numerical study of entanglement entropy in lattice gauge theory. *Nuclear Physics B*, 802(3):458 – 474, 2008.

[17] Pasquale Calabrese and John Cardy. Entanglement entropy and conformal field theory. *Journal of Physics A: Mathematical and Theoretical*, 42(50):504005, 2009.

[18] Tatsuma Nishioka, Shinsei Ryu, and Tadashi Takayanagi. Holographic entanglement entropy: an overview. *Journal of Physics A: Mathematical and Theoretical*, 42(50):504008, 2009.

[19] Mark P. Hertzberg and Frank Wilczek. Some calculable contributions to entanglement entropy. *Phys. Rev. Lett.*, 106:050404, Feb 2011.

[20] Mark P Hertzberg. Entanglement entropy in scalar field theory. *Journal of Physics A: Mathematical*

and Theoretical, 46(1):015402, 2013.

[21] Roger G. Melko, Ann B. Kallin, and Matthew B. Hastings. Finite-size scaling of mutual information in monte carlo simulations: Application to the spin-$\frac{1}{2}$ XXZ model. *Phys. Rev. B*, 82:100409, Sep 2010.

[22] Matthew B. Hastings, Iván González, Ann B. Kallin, and Roger G. Melko. Measuring renyi entanglement entropy in quantum monte carlo simulations. *Phys. Rev. Lett.*, 104:157201, Apr 2010.

[23] L. B. Weinstein, E. Piasetzky, D. W. Higinbotham, J. Gomez, O. Hen, and R. Shneor. Short range correlations and the emc effect. *Phys. Rev. Lett.*, 106:052301, Feb 2011.

[24] Stephen Inglis and Roger G. Melko. Wang-landau method for calculating rényi entropies in finite-temperature quantum monte carlo simulations. *Phys. Rev. E*, 87:013306, Jan 2013.

[25] Stephan Humeniuk and Tommaso Roscilde. Quantum monte carlo calculation of entanglement rényi entropies for generic quantum systems. *Phys. Rev. B*, 86:235116, Dec 2012.

[26] Jeremy McMinis and Norm M. Tubman. Renyi entropy of the interacting fermi liquid. *Phys. Rev. B*, 87:081108, Feb 2013.

[27] David J. Luitz, Xavier Plat, Nicolas Laflorencie, and Fabien Alet. Improving entanglement and thermodynamic rényi entropy measurements in quantum monte carlo. *Phys. Rev. B*, 90:125105, Sep 2014.

[28] Peter Broecker and Simon Trebst. Rnyi entropies of interacting fermions from determinantal quantum monte carlo simulations. *Journal of Statistical Mechanics: Theory and Experiment*, 2014(8):P08015, 2014.

[29] Lei Wang and Matthias Troyer. Renyi entanglement entropy of interacting fermions calculated using the continuous-time quantum monte carlo method. *Phys. Rev. Lett.*, 113:110401, Sep 2014.

[30] Fakher F. Assaad, Thomas C. Lang, and Francesco Parisen Toldin. Entanglement spectra of interacting fermions in quantum monte carlo simulations. *Phys. Rev. B*, 89:125121, Mar 2014.

[31] Fakher F. Assaad. Stable quantum monte carlo simulations for entanglement spectra of interacting fermions. *Phys. Rev. B*, 91:125146, Mar 2015.

[32] Dean Lee. Ground state energy at unitarity. *Phys. Rev. C*, 78:024001, Aug 2008.

[33] Dean Lee. Lattice simulations for few- and many-body systems. *Progress in Particle and Nuclear Physics*, 63(1):117 – 154, 2009.

[34] F. F. Assaad and H. G. Evertz. Worldline and determinantal quantum monte carlo methods for spins, phonons and electrons. In H. Fehske, R. Shnieider, and A. Weise, editors, *Computational Many-Particle Physics*. Springer, 2008.

[35] Simon Duane, A.D. Kennedy, Brian J. Pendleton, and Duncan Roweth. Hybrid monte carlo. *Physics Letters B*, 195(2):216 – 222, 1987.

[36] Steven Gottlieb, W. Liu, D. Toussaint, R. L. Renken, and R. L. Sugar. Hybrid-molecular-dynamics algorithms for the numerical simulation of quantum chromodynamics. *Phys. Rev. D*, 35:2531–2542, Apr 1987.

[37] R. M. Neal. MCMC using hamiltonian dynamics. In S. Brooks, A. Gelman, G. Jones, and X.-L. Meng, editors, *Handbook of Markov Chain Monte Carlo*. Chapman & Hall / CRC Press, 2011.

[38] Joaquín E Drut and Amy N Nicholson. Lattice methods for strongly interacting many-body systems. *Journal of Physics G: Nuclear and Particle Physics*, 40(4):043101, 2013.

[39] Joaquín E. Drut and Timo A. Lähde. Is graphene in vacuum an insulator? *Phys. Rev. Lett.*, 102:026802, Jan 2009.

[40] Joaquín E. Drut and Timo A. Lähde. Lattice field theory simulations of graphene. *Phys. Rev. B*, 79:165425, Apr 2009.

[41] Simon Hands and Costas Strouthos. Quantum critical behavior in a graphenelike model. *Phys. Rev. B*, 78:165423, Oct 2008.

[42] P. V. Buividovich and M. I. Polikarpov. Monte carlo study of the electron transport properties of monolayer graphene within the tight-binding model. *Phys. Rev. B*, 86:245117, Dec 2012.

[43] Ming-Chiang Chung and Ingo Peschel. Density-matrix spectra of solvable fermionic systems. *Phys. Rev. B*, 64:064412, Jul 2001.

[44] Siew-Ann Cheong and Christopher L. Henley. Many-body density matrices for free fermions. *Phys. Rev. B*, 69:075111, Feb 2004.

[45] Ingo Peschel. Calculation of reduced density matrices from correlation functions. *Journal of Physics A: Mathematical and General*, 36(14):L205, 2003.

[46] Brian Swingle. Entanglement entropy and the fermi surface. *Phys. Rev. Lett.*, 105:050502, Jul 2010.

[47] William H. Press, Saul A. Teukolsky, William T. Vetterling, and Brian P. Flannery. *Numerical Recipes in FORTRAN; The Art of Scientific Computing*. Cambridge University Press, New York, NY, USA, 2nd edition, 1993.

[48] Michael G. Endres, David B. Kaplan, Jong-Wan Lee, and Amy N. Nicholson. Noise, sign problems, and statistics. *Phys. Rev. Lett.*, 107:201601, Nov 2011.

[49] Thomas DeGrand. Log-normal distribution for correlators in lattice qcd? *Phys. Rev. D*, 86:014512, Jul 2012.

[50] W. Ketterle and M. W. Zwierlein. Making, probing and understanding ultracold Fermi gases. *Nuovo Cimento Rivista Serie*, 31:247–422, May 2008.

[51] Immanuel Bloch, Jean Dalibard, and Wilhelm Zwerger. Many-body physics with ultracold gases. *Rev. Mod. Phys.*, 80:885–964, Jul 2008.

[52] Stefano Giorgini, Lev P. Pitaevskii, and Sandro Stringari. Theory of ultracold atomic fermi gases. *Rev. Mod. Phys.*, 80:1215–1274, Oct 2008.

[53] M. H. Anderson, J. R. Ensher, M. R. Matthews, C. E. Wieman, and E. A. Cornell. Observation of bose-einstein condensation in a dilute atomic vapor. *Science*, 269(5221):198–201, 1995.

[54] C. C. Bradley, C. A. Sackett, J. J. Tollett, and R. G. Hulet. Evidence of bose-einstein condensation in an atomic gas with attractive interactions. *Phys. Rev. Lett.*, 75:1687–1690, Aug 1995.

[55] K. B. Davis, M. O. Mewes, M. R. Andrews, N. J. van Druten, D. S. Durfee, D. M. Kurn, and W. Ketterle. Bose-einstein condensation in a gas of sodium atoms. *Phys. Rev. Lett.*, 75:3969–3973, Nov 1995.

[56] C. A. Regal, M. Greiner, and D. S. Jin. Observation of resonance condensation of fermionic atom pairs. *Phys. Rev. Lett.*, 92:040403, Jan 2004.

[57] Cheng Chin, Rudolf Grimm, Paul Julienne, and Eite Tiesinga. Feshbach resonances in ultracold gases. *Rev. Mod. Phys.*, 82:1225–1286, Apr 2010.

[58] G. Pagano, M. Mancini, G. Cappellini, L. Livi, C. Sias, J. Catani, M. Inguscio, and L. Fallani. Strongly interacting gas of two-electron fermions at an orbital feshbach resonance. *Phys. Rev. Lett.*, 115:265301, Dec 2015.

[59] M. Höfer, L. Riegger, F. Scazza, C. Hofrichter, D. R. Fernandes, M. M. Parish, J. Levinsen, I. Bloch, and S. Fölling. Observation of an orbital interaction-induced feshbach resonance in ^{173}Yb. *Phys. Rev. Lett.*, 115:265302, Dec 2015.

[60] Mark J. H. Ku, Ariel T. Sommer, Lawrence W. Cheuk, and Martin W. Zwierlein. Revealing the superfluid lambda transition in the universal thermodynamics of a unitary fermi gas. *Science*, 335(6068):563–567, 2012.

[61] Eugenio Cocchi, Luke A. Miller, Jan H. Drewes, Marco Koschorreck, Daniel Pertot, Ferdinand Brennecke, and Michael Köhl. Equation of state of the two-dimensional hubbard model. *Phys. Rev. Lett.*, 116:175301, Apr 2016.

[62] C. Cao, E. Elliott, J. Joseph, H. Wu, J. Petricka, T. Schäfer, and J. E. Thomas. Universal quantum viscosity in a unitary fermi gas. *Science*, 331(6013):58–61, 2011.

[63] J. A. Joseph, E. Elliott, and J. E. Thomas. Shear viscosity of a unitary fermi gas near the superfluid phase transition. *Phys. Rev. Lett.*, 115:020401, Jul 2015.

[64] Rajibul Islam, Ruichao Ma, Philipp M. Preiss, M. Eric Tai, Alexander Lukin, Matthew Rispoli, and Markus Greiner. Measuring entanglement entropy in a quantum many-body system. *Nature*, 528(7580):77–83, 12 2015.

[65] Adam M. Kaufman, M. Eric Tai, Alexander Lukin, Matthew Rispoli, Robert Schittko, Philipp M. Preiss, and Markus Greiner. Quantum thermalization through entanglement in an isolated many-body system. *Science*, 353(6301):794–800, 2016.

[66] Bei Zeng, Xie Chen, Duan-Lu Zhou, and Xiao-Gang Wen. Quantum information meets quantum matter – from quantum entanglement to topological phase in many-body systems, 2015.

[67] Erez Zohar, J. Ignacio Cirac, and Benni Reznik. Quantum simulations of gauge theories with ultracold atoms: Local gauge invariance from angular-momentum conservation. *Phys. Rev. A*, 88:023617, Aug 2013.

[68] Erez Zohar and Michele Burrello. Formulation of lattice gauge theories for quantum simulations. *Phys. Rev. D*, 91:054506, Mar 2015.

[69] T. Pichler, M. Dalmonte, E. Rico, P. Zoller, and S. Montangero. Real-time dynamics in u(1) lattice gauge theories with tensor networks. *Phys. Rev. X*, 6:011023, Mar 2016.

[70] Immanuel Bloch, Jean Dalibard, and Sylvain Nascimbene. Quantum simulations with ultracold quantum gases. *Nat Phys*, 8(4):267–276, 04 2012.

[71] I. M. Georgescu, S. Ashhab, and Franco Nori. Quantum simulation. *Rev. Mod. Phys.*, 86:153–185, Mar 2014.

[72] Andreas Reiserer and Gerhard Rempe. Cavity-based quantum networks with single atoms and optical photons. *Rev. Mod. Phys.*, 87:1379–1418, Dec 2015.

[73] George A. Baker. Neutron matter model. *Phys. Rev. C*, 60:054311, Oct 1999.

[74] David B. Kaplan, Martin J. Savage, and Mark B. Wise. A new expansion for nucleon-nucleon interactions. *Physics Letters B*, 424(34):390 – 396, 1998.

[75] David B. Kaplan, Martin J. Savage, and Mark B. Wise. Two-nucleon systems from effective field theory. *Nuclear Physics B*, 534(1):329 – 355, 1998.

[76] K. M. O'Hara, S. L. Hemmer, M. E. Gehm, S. R. Granade, and J. E. Thomas. Observation of a strongly interacting degenerate fermi gas of atoms. *Science*, 298(5601):2179–2182, 2002.

[77] D. M. Eagles. Possible pairing without superconductivity at low carrier concentrations in bulk and thin-film superconducting semiconductors. *Phys. Rev.*, 186:456–463, Oct 1969.

[78] Leggett, A. J. Cooper pairing in spin-polarized fermi systems. *J. Phys. Colloques*, 41(C7):C7–19–C7–26, 1980.

[79] P. Nozières and S. Schmitt-Rink. Bose condensation in an attractive fermion gas: From weak to strong coupling superconductivity. *Journal of Low Temperature Physics*, 59(3):195–211, 1985.

[80] Koushik Balasubramanian and John McGreevy. Gravity duals for nonrelativistic conformal field theories. *Phys. Rev. Lett.*, 101:061601, Aug 2008.

[81] D. T. Son. Toward an ads/cold atoms correspondence: A geometric realization of the schrödinger symmetry. *Phys. Rev. D*, 78:046003, Aug 2008.

[82] Yusuke Nishida and Dam T. Son. Nonrelativistic conformal field theories. *Phys. Rev. D*, 76:086004, Oct 2007.

[83] Sergei V. Isakov, Matthew B. Hastings, and Roger G. Melko. Topological entanglement entropy of a bose-hubbard spin liquid. *Nat Phys*, 7(10):772–775, 10 2011.

[84] M. Lüscher. Volume dependence of the energy spectrum in massive quantum field theories. *Communications in Mathematical Physics*, 105(2):153–188, 1986.

[85] Martin Lüscher. Two-particle states on a torus and their relation to the scattering matrix. *Nuclear Physics B*, 354(2):531 – 578, 1991.

[86] A. Osterloh, Luigi Amico, G. Falci, and Rosario Fazio. Scaling of entanglement close to a quantum phase transition. *Nature*, 416(6881):608–610, 04 2002.

[87] Pasquale Calabrese, Mihail Mintchev, and Ettore Vicari. Entanglement entropy of one-dimensional gases. *Phys. Rev. Lett.*, 107:020601, Jul 2011.

[88] Brian Swingle, Jeremy McMinis, and Norm M. Tubman. Oscillating terms in the renyi entropy of fermi gases and liquids. *Phys. Rev. B*, 87:235112, Jun 2013.

[89] G. De Chiara, L. Lepori, M. Lewenstein, and A. Sanpera. Entanglement spectrum, critical exponents, and order parameters in quantum spin chains. *Phys. Rev. Lett.*, 109:237208, Dec 2012.